Doklady Physics, Vol. 47, No. 11, 2002, pp. 775–777. Translated from Doklady Akademii Nauk, Vol. 387, No. 1, 2002, pp. 37–39.

PHYSICS

Formula for the Current Flow Coefficient

Kh. Kh. Imomnazarov and B. Kh. Imomnazarov

Presented by Academician A.S. Alekseev March 20, 2002

Received April 5, 2002

To date, electrokinetic phenomena have been studied in various fields of science and technology. These phenomena must be taken into account in both geophysics [1] and biomechanics [2]. Electrokinetic phenomena are successfully applied while developing chemotron elements in computer engineering, seismic sensors and hydrophones, as well as devices for monitoring the composition of fluids and fluid-flow rates.

In [3], a formula for the current flow coefficient

$$C_c = \frac{\varepsilon\zeta}{\tilde{\mu}F_2} \tag{1}$$

was obtained on the basis of the model of [4]. Here, ε and $\tilde{\mu}$ are the permittivity and viscosity of a fluid, ζ is the ζ potential, $F_2 = \dfrac{T^2}{d_0}$, T is the tortuosity, and d_0 is the porosity of the medium.

In accordance with the results of laboratory experiments, the current flow coefficient depends on the permeability of the fluid (see Figs. 8 and 16 in [3]):

$$C_c = a\sqrt{k}, \tag{2}$$

where k is the permeability and a is a positive constant.

In [5], a nonlinear mathematical model that combines equations of filtration and Maxwell equations was constructed. This model describes the movement of an electrically conducting fluid in a porous conducting elastically deformable medium. The model is based on three basic principles: the validity of conservation laws, the Galilean relativity principle, and the consistency of equations of motion for a conducting fluid with thermodynamic-equilibrium conditions. The hyperbolic behavior of a system linearized with respect to an arbitrary hydrodynamic background in the reversible magnetohydrodynamic approximation (in the absence of energy dissipation) is shown. In this model, there exist four types of sound vibrations, namely, Alfven vibrations, transverse vibrations, and two longitudinal vibrations.

In this paper, the dependence between the coefficients of the current flow and the potential flow of an electrically conducting fluid in an electrically conducting porous medium on the porosity of a medium, the conductivity of a fluid, its permittivity, the ζ potential, and the ratio between physical densities of the conducting fluid and a conducting elastic porous body are established. It is theoretically shown that the product of the coefficients of the current flow and of the potential flow is strictly positive.

ELECTROKINETIC MODEL

In [8–10], modified Darcy and Ohm laws

$$\mathbf{v} = -\frac{\nabla p}{\chi\rho\rho_l} + \frac{\gamma}{\chi\rho_l}\nabla\phi, \tag{3}$$

$$\mathbf{J} = -\frac{\gamma}{\chi\rho}\nabla p - \frac{\sigma\chi - \gamma^2}{\chi}\nabla\phi, \tag{4}$$

which are suitable for describing electrokinetic phenomena in porous media were obtained. Here, $\mathbf{v}$ is the flow velocity of a conducting fluid; $\mathbf{J}$ is the electric-current density; $\rho = \rho_l + \rho_s$, $\rho_l(\sigma_l)$, and $\rho_s(\sigma_s)$ are the partial densities (conductivities) of a conducting fluid and of a conducting elastic porous body, respectively; χ is the friction coefficient; and γ is the electrokinetic coefficient. In this case, the coefficients χ and γ and conductivity $\sigma = \sigma_l + \sigma_s$ satisfy the inequality [7, 8]

$$\sigma\chi - \gamma^2 > 0.$$

It is worth noting that the crossed phenomenological coefficients in the generalized Darcy law and Ohm law, in contrast to those which were proposed previously (see [2, 4, 9–11] and references therein), are not equal to each other. Moreover, the coefficients determining the current density, as distinct to the mentioned papers,

Institute of Computational Mathematics and Mathematical Geophysics, Siberian Division, Russian Academy of Sciences, pr. Lavrent'eva 6, Novosibirsk, 630090 Russia

1028-3358/02/4711-0775$22.00

do depend on the friction coefficient (permeability, viscosity of a fluid), as well as on the partial densities of a conducting elastic porous body and of a conducting fluid. It is well known [8] that the Darcy law and Ohm law, like other laws, have no physical sense without the entropy-balance equation.

As was shown in [7], the electrokinetic coefficient γ is inversely proportional to the product of the density ρ and the coefficient C_p of the potential flow:

$$\gamma = \frac{1}{\rho C_p}, \quad C_p = \frac{\varepsilon\zeta}{\tilde{\mu}\sigma_l}. \tag{5}$$

FORMULA FOR THE CURRENT FLOW COEFFICIENT

Using the definition for the current flow coefficient from [11],

$$C_c = -\frac{\mathbf{J}}{\nabla p}\Big| \nabla\phi = 0,$$

we can obtain from Ohm law (4) the relation

$$C_c = \frac{\gamma}{\chi\rho}.$$

From here, with allowance for expression (5) and from the definition of the friction coefficient $\chi = \frac{\tilde{\mu}}{\rho\rho_l k}$ [12], we can write out

$$C_c = \frac{\rho_l^f}{\rho_s^f}\frac{d_0}{1-\left(1-\frac{\rho_l^f}{\rho_s^f}\right)d_0}\frac{k}{\tilde{\mu}C_p}, \tag{6}$$

where ρ_l^f and ρ_s^f are the physical densities of a conducting fluid and a conducting elastic porous body, respectively. On one hand, it follows from relationship (6) that the product of the coefficients of potential and current flows is strictly positive:

$$C_c C_p = \frac{\rho_l^f}{\rho_s^f}\frac{d_0}{1-\left(1-\frac{\rho_l^f}{\rho_s^f}\right)d_0}\frac{k}{\tilde{\mu}} > 0.$$

On the other hand, we find from relationship (6) with the definition of the potential-flow coefficient taken into account that

$$C_c = \frac{\frac{\rho_l^f}{\rho_s^f}\varepsilon\zeta d_0}{1-\left(1-\frac{\rho_l^f}{\rho_s^f}\right)d_0}\frac{k}{\sigma_l}. \tag{7}$$

Hence, it follows that the current-flow coefficient depends on the porosity, permeability, conductivity, permittivity, and ζ potential of a fluid and on the ratio of physical densities of a fluid and an elastic porous body. However, it does not depend on the viscosity of the fluid. At the same time, the electrokinetic coefficient and the coefficient of the potential flow depend on the partial densities of the elastic porous body and the fluid, as well as on the conductivity, permittivity, and ζ potential of the fluid and is independent of its permeability.

Using the formula

$$k = \frac{d_0\tilde{\mu}}{\omega_c T\rho_l^f}\frac{2}{M},$$

derived in [13], we find from expression (7)

$$|C_c| = \sqrt{\frac{2\tilde{\mu}}{\omega_c T\rho_l^f M}}\frac{\frac{\rho_l^f}{\rho_s^f}\varepsilon|\zeta|d_0^{\frac{3}{2}}}{1-\left(1-\frac{\rho_l^f}{\rho_s^f}\right)d_0}\frac{\sqrt{k}}{\sigma_l}.$$

Here, ω_c is the critical frequency of the Biot theory and M is a dimensionless parameter that depends on the geometry of pores.

It follows from here that the modulus of the current-flow coefficient is proportional to the square root of the permeability, which coincides qualitatively with results of the laboratory experiments described in [3].

ACKNOWLEDGMENTS

The authors are grateful to V.N. Dorovskiĭ for fruitful discussions and to the reviewer of this paper for critical comments.

This work was supported by the Russian Foundation for Basic Research, project no. 00-15-98544.

REFERENCES

1. N. I. Migunov, Izv. Akad. Nauk SSSR, Fiz. Zemli, No. 5, 52 (1978).
2. M. E. Levenston, E. H. Frank, and A. J. Grodzinsky, J. Appl. Mech. **66**, 323 (1999).
3. S. Yoshida, J. Geophys. Res. **106**, 2103 (2001).

4. S. R. Pride, Phys. Rev. B **50** (21), 15678 (1994).
5. V. N. Dorovskiĭ and Kh. Kh. Imomnazarov, Math. Comput. Modeling **20** (7), 91 (1994).
6. Kh. Kh. Imomnazarov, in *Proc. Int. Conf. "Mathematical Models and Methods of Their Research," Krasnoyarsk, 2001*, Vol. 1, p. 277.
7. Kh. Kh. Imomnazarov, Candidate's Dissertation in Physics and Mathematics (Vychisl. Tsentr Sib. Otd. Ross. Akad. Nauk, Novosibirsk, 1995).
8. S. R. de Groot and P. Mazur, *Nonequilibrium Thermodynamics* (North-Holland, Amsterdam, 1962; Mir, Moscow, 1964).
9. D. V. Fitterman, J. Geophys. Res. **83**, 5923 (1978).
10. T. Ishido, J. Geotherm. Res. Soc. Jap. **3**, 87 (1981).
11. W. R. Sill, Geophysics **48** (1), 76 (1983).
12. A. M. Blokhin and V. N. Dorovskiĭ, *Mathematical Modeling in Theory of Multivelocity Continuum* (Nova Science, New York, 1995).
13. D. L. Johnson, J. Koplik, and R. Dashen, J. Fluid Mech. **176**, 379 (1987).

Translated by G. Merzon

Doklady Physics, Vol. 47, No. 11, 2002, pp. 778–782. Translated from Doklady Akademii Nauk, Vol. 387, No. 1, 2002, pp. 40–45.

PHYSICS

A Standard Isotherm of Copper

Corresponding Member of the RAS N. N. Kalitkin and L. V. Kuz'mina

Received March 14, 2002

1. FORMULATION OF PROBLEMS

Constructing wide-ranging equations of state for various materials is a challenging problem. Its essential part is finding zero isotherms, i.e., global curves of cold compression $P(\rho)$ applicable at pressures $0 \le P < \infty$ (ρ is the density of a material). Models of a planet's structure, regimes of shock-free compression of thermonuclear targets, etc., are very sensitive to these isotherms. The initial segments of these curves are obtained from experiments on static and shock-wave compressions, while the upper segments are derived from theoretical calculations. However, a wide interval for which there are no reliable data remains between these segments. This interval is filled with approximated data based on model considerations.

A number of reasonable approximations were constructed in studies performed in our country in 1960–1990. There were no other similar publications abroad, although such approximations were presumably constructed. This conclusion follows from the existence of the Los Alamos SESAME library for materials properties. We compared these studies and found that the differences between $P(\rho)$ curves in them reach 25%, and none of the curves has a convincing justification. Therefore, the problem of constructing precision curves remained unsolved.

Here, we propose a method of constructing $P(\rho)$ curves for materials that undergo no phase transitions. As an example, we chose copper. Its fcc crystal lattice is close packed, and the metal has no phase transitions under static compression. Copper possesses plasticity, which provides for isotropy of static compressions and their good conformity with dynamic ones. Copper melts under dynamic compressions, but this transition is almost imperceptible. For copper, the number of experimental measurements is rather large, and their accuracy is higher than for other materials. Therefore, copper is the most suitable material for a standard.

Below, we construct the precision room-temperature isotherm of copper (it is more convenient than the zero isotherm). Under compressions smaller than 2.4-fold and higher than 60-fold, the error of the isotherm does not exceed 0.2–0.3%, whereas it is 1–2% for intermediate compressions. This is more exact than in the case of all previously proposed curves by a factor of 7–10. This isotherm is recommended as a standard for interpreting experiments in which the comparative compressibility of various materials was measured.

For measuring pressures in static experiments with diamond anvils, a ruby sensor is used. We found its systematic deviations from our standard by 1–2% within the range of $0 \le P \le 1$ Mbar, which evidenced the sensor error. We corrected the sensor, which reduced the error in pressure measurements down to 0.2–0.3%, i.e., elevated the experimental accuracy by a factor of 5–7.

2. THEORETICAL BACKGROUND

The compression of a material is characterized by the quantity $\sigma = \dfrac{\rho}{\rho_0}$, where ρ_0 is the normal (usual) density of a medium. For hypercompressions with $\sigma \ge 10^6$, the material behaves as a homogeneous electron gas (HEG) and its pressure is

$$P = 1003.60\left(\frac{\rho Z}{A}\right)^{5/3}. \qquad (1)$$

Here, Z and A are the atomic number and atomic weight of an element. We take

$$[P]\text{—GPa}, \quad [\rho]\text{—g/cm}^3, \quad [v]\text{—km/s}, \quad [\lambda]\text{—nm}. \qquad (2)$$

Dependence (1) is valid up to compressions at which the transition of an atom into the neutron state begins. When the compressions decrease, the accuracy of formula (1) becomes insufficient and, for $\sigma \ge 10^4$, it is necessary to use the Thomas–Fermi (TF) statistical atomic model [1]. For lower densities with $\sigma \ge 60$, it is necessary to complement this model with quantum and exchange corrections as was proposed in [2] [TF corrected (TFC) model]. These are *ab initio* models, but they ignore the atomic-shell structure (the band structure of a solid). For this reason, their ranges of applicability are far from normal conditions.

In the case of hypercompressions, HEG (1) sets a limit for both models. In this case, their thermodynamic functions are expanded into series in terms of powers of

Institute of Mathematical Modeling,
Russian Academy of Sciences,
Miusskaya pl. 4a, Moscow, 125047 Russia

1028-3358/02/4711-0778$22.00

$\rho^{-1/3}$, and the minor coefficients of the expansion are known. However, the series converge only for $\sigma \geq 10^4$, so that their immediate use is limited.

The TF model is a semiclassical approximation to the Hartree–Fock model, while the quantum and exchange corrections are combined in the first even term of the expansion into series in terms of the powers of the operator $i\hbar\nabla$. Therefore, the relative error of the TF model can be estimated by the difference between this and the TFC models, i.e., by the quantity

$$\varepsilon(\rho) = 1 - \frac{P_{\mathrm{TFC}}(\rho)}{P_{\mathrm{TF}}(\rho)}. \quad (3)$$

In the TFC model, a reasonable estimate of the relative error is the quantity $\varepsilon^2(\rho)$. The above lower limits of applicability correspond to $\varepsilon \approx 0.01$ for the TF model and to $\varepsilon^2 \approx 0.01$ for the TFC model.

In the 1970s, complicated quantum-mechanical models taking into account the atomic-shell structure were proposed. However, rigorous *ab initio* models of this type described the experiments no better than the TFC model. The best agreement was obtained with models involving fitting parameters that, in fact, were interpolations (although rather complicated). Constructing the simple approximation described below has no less physical sense.

3. DYNAMIC EXPERIMENTS

Virtually all experiments with shock-wave compressions are accumulated in [3–5]. For copper, they involve more than 250 points in the form $D(u)$, where D is the shock-wave velocity and u is the velocity of material beyond the shock front. From them, $P_{\mathrm{H}}(\rho)$ and other caloric quantities are reconstructed according to the Hugoniot relationships for a shock wave. The most accurate treatment of experimental data was made in [6]. In this study, an approximation that provides excellent agreement with the TFC model within the 100 Mbar–30 Gbar range is constructed, and at pressures $P \leq 4$ Mbar, this approximation transforms into the classical form

$$D \approx c_0 + bu \quad (4)$$

with the coefficients

$$c_0 = 3.923 \pm 0.002 \text{ km/s}, \; b = 1.511 \pm 0.003. \quad (5)$$

The spread of the experimental points is estimated as 1.05%, while the accuracy of approximation (4) is 0.16%.

The principal Hugoniot adiabat begins from a normal state of a material: $P(\rho_0) = 0$ and $t_0 \approx 20$–26°C. In the experiments, the initial density varied from 8.90 to 8.93, but its influence was negligible. Therefore, we took as the normal copper density the crystallographic value

$$\rho_0 = 8.934 \text{ g/cm}^3, \quad (6)$$

variations of the room temperature being negligible. The coefficients c_0 and b determine the initial slope and initial curvature of the Hugoniot adiabat:

$$\left(\frac{dP_{\mathrm{H}}}{d\rho}\right)_0 = c_0^2, \quad \left(\frac{d^2P_{\mathrm{H}}}{d\rho^2}\right) = \frac{(4b-2)c_0^2}{\rho_0}. \quad (7)$$

As is known, an isentropy passing through the normal state has the same initial slope and curvature. For a solid material, the room-temperature isotherm is so close to this isentropy that the same parameters can be assigned to it, but its asymptotic formula is HEG (1).

If the compression increases, the principal Hugoniot adiabat rapidly deviates upward from the room-temperature isotherm by 1% for $\sigma \approx 1.09$ and by 10% for $\sigma \approx 1.37$. Therefore, it is admissible to use only initial values (6) and (7) for constructing the isotherm instead of the total information about the shock adiabat.

4. APPROXIMATION

The concept of expansion in terms of $\rho^{-1/3}$ was proposed by Cormer in 1960. The most successful approximation described cold pressure as the sum [7–9]

$$P(\rho) \approx \sum_{n=0}^{5} \beta_n \rho^{n/3}. \quad (8)$$

Approximation [10], which used a different dependence, turned out to be poorer. The coefficient b_5 in [7, 9] was taken from asymptotic formula (1), while it did not satisfy this asymptotic formula in [8] (this is not good). Additionally, conditions for the preservation of normal density $P(\rho_0) = 0$ and the best description of other reliable experimental and theoretical data were posed. The latter conditions were formulated in these studies in a different way, and the resulting curves differed drastically. In addition, the coefficients β_n are alternating; therefore, they must necessarily be written out with a large number of digits.

It is worth noting that approximation (8) and the condition $P(\rho_0) = 0$ can be immediately combined by converting to the form

$$P(\rho) = \rho^{5/3} \sum_{n=1}^{5} b_n (1-x)^n, \quad x = \sigma^{-1/3} \equiv \left(\frac{\rho_0}{\rho}\right)^{1/3}, \quad (9)$$

the relation between the coefficients b_n and β_n being evident. This form can be generalized by summation in (9) up to an arbitrary number N, asymptotic formula (1) being conserved. The coefficients b_n can be taken with a smaller number of significant digits. However, the sensitivity of the curves to the additional conditions is not reduced.

This fact is seen from Table 1, where we display the coefficients for copper b_n corresponding to [7–9]. They are obtained from the coefficients β_n presented in the

Table 1. Coefficients b_n in approximation (9) for copper

Reference	b_n				
	$n = 1$	$n = 2$	$n = 3$	$n = 4$	$n = 5$
[7]	10.726	37.119	45.232	142.786	34.095
[8]	10.967	32.967	23.241	351.199	–194.775
[9]	11.855	–20.771	558.967	–911.557	645.150
This study	10.727	32.887	53.763	81.101	93.011

Table 2. Coefficients a_n in approximation (10) for copper

Reference	a_n				Range x
	$n = 0$	$n = 1$	$n = 2$	$n = 3$	
This standard	2.3724	3.0660	0.8355	–0.6700	0.00–1.00
[11]	2.3727	2.9822	0	0	0.99–1.00
[12]	2.3621	2.7450	4.2183	0	0.90–0.99
[13]	2.2284	4.8669	–4.8025	0	0.84–1.00
[14]	2.3309	3.2243	0.8013	0	0.81–1.00
[15]	2.3628	3.4842	0	0	0.76–0.90

same table. It can be seen that in various studies, the coefficients differ strongly. This fact is indicative of an unsuccessful situation.

The other approximation with a smaller number of digits used turned out to be the most successful:

$$P(\rho) \approx \rho^{5/3}(1-x)\exp[y(x)],$$
$$y(x) = \sum_{n=0}^{3} a_n(1-x)^n. \qquad (10)$$

This approximation is nonequivalent to (9) but imparts the normal density. For describing asymptotic formula (1), it is necessary to assume

$$a_0 + a_1 + a_2 + a_3 = 6.91134 + \frac{5}{3}\ln\frac{Z}{A}. \qquad (11)$$

We also require reproduction of both the experimental initial slope and the curvature for the curve $P(\rho)$ according to (7). Thus, we arrive at the expression

$$a_0 = \ln(3c_0^2\rho_0^{-2/3}), \quad a_1 = 6(b-1). \qquad (12)$$

As the fourth condition, we take the least-mean-square deviation of approximation (10) from the TFC model with allowance for the estimate of the accuracy of this model:

$$\int_0^1 \left[1 - \frac{P_{\mathrm{TFC}}(\rho)}{P(\rho)}\right]^2 \varepsilon^{-4}(\rho)dx = \min. \qquad (13)$$

From formulas (5), (6), and (12), we directly obtain for copper

$$a_0 = 2.3724, \quad a_1 = 3.0660. \qquad (14)$$

Then, the coefficients a_2 and a_3 are found by numerically solving the set of Eqs. (11) and (13). The last equation is not reduced to the linear one; however, the problem is reduced to minimizing the single-argument function, which is sufficiently simple. The calculation results together with (14) are displayed in Table 2 and in Fig. 1. This room-temperature copper isotherm is proposed as a standard.

For comparison, in Fig. 1 we plot curves corresponding to the TF model and TFC model, as well as to the principal Hugoniot adiabat. It can be seen that approximation (10) is very close to the TFC model for $0 \le x \le 0.25$ (i.e., for $\sigma \ge 60$) when $\varepsilon^2 \le 0.01$. Therefore, within this range, the global approximation is reliably corroborated by the theory. With increasing x, the accuracy of the TFC model rapidly decreases and the approximation deviates from it.

5. STATIC COMPRESSIONS

The shock adiabat deviates too rapidly from the isotherm. For this reason, static experiments are necessary to substantiate the approximation. Measurements using piston equipment for copper [11] are very accurate and agree excellently with the shock-wave data, but they encompass a narrow range of $P \le 3$ GPa ($0.99 \le x \le 1$). The diamond anvils used in [12] cover the range $P \le 100$ GPa ($0.9 \le x \le 1$); the compression is measured

with an accuracy of 0.15%, while the accuracy of pressure measurement is much poorer.

The isotherms obtained in [13–15] by treating shock-wave experiments are less reliable, because a model accounting for thermal terms is used. However, these isotherms cover a much wider range of $P \leq 400$ GPa ($0.75 \leq x \leq 1$).

The experimental data of [11–15] were approximated by dependence (10) using the method of least squares. In this case, no consistency with the HEG asymptotic formula (11) was required. The derived coefficients a_n are displayed in Table 2, and the corresponding curves are shown in Fig. 2. In the same figure, we show the global approximation corresponding to Section 4 and the shock adiabat. The difference $\Delta y = 0.01$ corresponds to a 1% deviation in pressure. For $x \longrightarrow 1$, all the isotherms must touch the shock adiabat; therefore, their difference from the shock adiabat serves as a measure of their errors. As is seen, the accuracy of the majority of experiments attains 1–2%, and their deviations from the global approximation are approximately the same.

Consequently, the experiments corroborate the global approximation within the range $0.75 \leq x \leq 1.0$ ($1 \leq \sigma \leq 2.4$) well.

6. DISCUSSION

This global approximation is well corroborated by the theory for $0 \leq x \leq 0.25$ and by the experiments for $0.75 \leq x \leq 1.0$. Within the range $0.25 \leq x \leq 0.75$, there are no data verifying this approximation. However, this range is not too wide, and the curve itself expressed in variables $y(x)$ is reasonably close to a straight line. Therefore, the choice of the variables x and y is successful, whereas approximation (10) in itself seems to be quite reliable.

An additional test was construction of the approximation in less successful form (9) when the curve considerably differs from a straight line. Here, the choice of coefficients b_n also obeyed the conservation requirements of asymptotic formula (1), tangency conditions (7), and mean-square approximation to the theory (13). The corresponding coefficients are more sensitive to the choice of these assumptions than are the coefficients a_n. The calculated values of b_n are presented in Table 1.

In Fig. 3, we show the deviation (in %) from global approximation (10) for all the pressure curves. The deviation of our approximation (9) is lower than 0.7% in the most unfavorable portion of the range and is small at its edges. This fact enables us to estimate the error of formula (10) as 0.2–0.3% for $0 \leq x \leq 0.25$ or $0.75 \leq x \leq 1$ (i.e., $\sigma \geq 60$ or $\sigma \leq 2.4$) and up to 1–2% within the range $0.25 \leq x \leq 0.75$.

In the same figure, we show the deviations of other global approximations of [7–10] and (for verification) the deviations of the experimental results of [11–15] from the TFC model [2]. The approximations of [8–10]

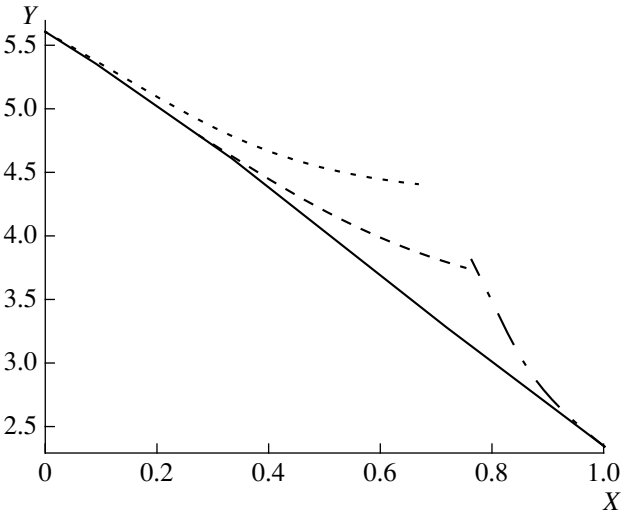

Fig. 1. Room-temperature isotherm of copper in special coordinates. Solid, dashed, dotted, and dashed–dotted lines correspond to standard approximation (10), the TFC model, the TF model, and the Hugoniot shock adiabat, respectively.

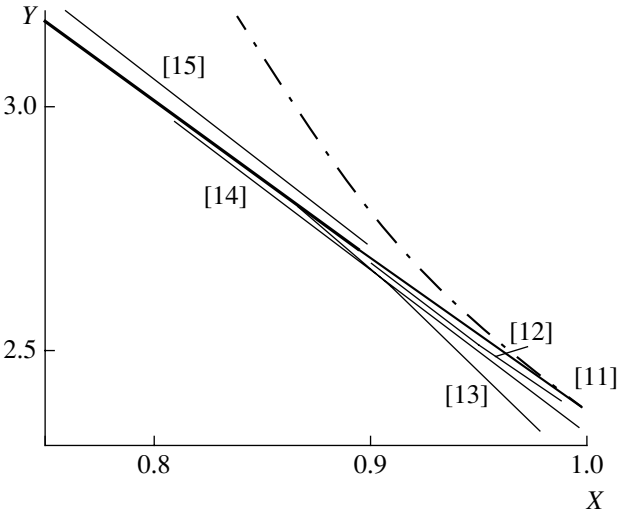

Fig. 2. Room-temperature isotherm of copper. Thick, thin, and dashed–dotted lines correspond to the standard approximation, experimental data (numbers near the lines correspond to the reference numbers), and Hugoniot shock adiabat, respectively.

differ very significantly from one another, which was not previously noted. They agree poorly with the experiments. Their considerable deviation from the results of this study (up to 15–25%) can be explained by the unsuccessful procedure of concordance with the TFC model: in these approximations, the coincidence of $P(\rho)$ with the TFC model was required instead of the use of criterion (13) for $\sigma \approx 10$–15 when the error of the TFC model in itself attained ~10%. The situation is somewhat better in [7], where criterion (13) was adopted, but the coefficient β_4 was unsuccessfully determined. The poor qualitative and quantitative

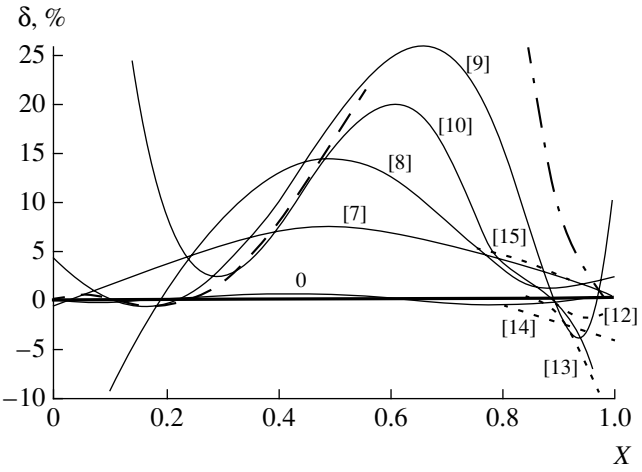

Fig. 3. Deviation from the standard isotherm: thick line is zero (standard) isotherm, thin lines are other global approximations, dotted lines are experimental data, dashed–dotted lines correspond to the Hugoniot shock adiabat, and dashed line corresponds to the TFC model. The numbers near the curves correspond to the reference numbers, and 0 corresponds to the present approximation in form of (9).

behavior of these approximations within the experimental region of $0.75 \le x \le 1$ also entirely rules them out.

Thus, global approximation (10) constructed by us is the most reliable; it is more precise than all the previous approximations by a factor of ~10.

7. RUBY SENSOR

The experiments using diamond anvils [12] diverge by 1–2% in pressure, not only with our global approximation, but also with the precision shock adiabat obtained in [6] for $\sigma \longrightarrow 1$. The accuracy of the adiabat of [6] attains 0.16%; therefore, the deviation is caused by errors of the experiments described in [12].

The compressions in [7] were determined by means of the X-ray diffractometry of the copper-crystal lattice with an accuracy of 0.15%. However, pressures were measured by the shift of the ruby R_1 ($\lambda_0 = 693$ nm) fluorescence line. This shift was calibrated according to shock-wave compressions for several metals; this compressions had a considerable spread. It is evident that such an inexact calibration is the major reason for the deviation; i.e., the pressure sensor is incorrect.

Within the range of $P \le 100$ GPa, the accuracy of our approximation (10) attains ~0.2%. We calculated this dependence of pressure on the fluorescence-line shift, which matches compressions (10) and those described in [12] within this range with an accuracy of 0.1%:

$$P \approx 2.784 \cdot \Delta\lambda\left(1 + \frac{\Delta\lambda}{73.8}\right)^{1/4}, \quad 5 \le P \le 100 \text{ GPa}. \quad (15)$$

The use of calibration formula (15) decreases the error for the ruby pressure sensor down to 0.2–0.3%. This implies an improvement in the measurement accuracy with diamond anvils by a factor of 5–7.

Thus, we proposed a method of constructing wide-ranging room-temperature isotherms $P(\rho)$ for materials that undergo no phase transitions in the compression process. We constructed the standard isotherm for copper, whose accuracy is higher than that of the previously proposed curves by a factor of 7–10. We corrected a ruby pressure sensor, which improved the accuracy of measurements made with diamond anvils by a factor of 5–7.

ACKNOWLEDGMENTS

This work was supported by the Russian Foundation for Basic Research, project no. 02-01-00066.

REFERENCES

1. R. Latter, J. Chem. Phys. **24** (2), 280 (1956).
2. N. N. Kalitkin, Zh. Éksp. Teor. Fiz. **38**, 1534 (1960) [Sov. Phys. JETP **11**, 1106 (1960)].
3. *Compendium of Shock-Wave Data*, Ed. by M. van Thiel (Univ. of California Press, Livermore, 1977).
4. *LASL Shock Hugoniot Data*, Ed. by S. P. Marsh (Univ. of California Press, Berkley, 1980).
5. *Properties of Condensed Matter under High Pressures and Temperatures*, Ed. by R. F. Trunin (Arzamas-16, 1992).
6. N. N. Kalitkin and L. V. Kuz'mina, Dokl. Akad. Nauk **368**, 178 (1999) [Dokl. Phys. **44**, 589 (1999)].
7. N. N. Kalitkin and I. A. Govorukhina, Fiz. Tverd. Tela (Leningrad) **7**, 355 (1965) [Sov. Phys. Solid State **7**, 287 (1965)].
8. L. V. Al'tshuler and S. E. Brusnikin, Teplofiz. Vys. Temp. **27** (1), 42 (1989).
9. E. A. Kuz'menkov, Izv. Sib. Otd. Akad. Nauk SSSR, Ser. Tekh. Nauki, No. 6, 106 (1989).
10. L. V. Al'tshuler, A. A. Bakanova, and R. F. Trunin, Zh. Éksp. Teor. Fiz. **42**, 91 (1962) [Sov. Phys. JETP **15**, 65 (1962)].
11. P. W. Bridgman, Proc. Am. Acad. Arts Sci. **76** (6), 189 (1949).
12. H. K. Mao, P. M. Bell, J. W. Shaner, and D. J. Steinberg, J. Appl. Phys. **49** (6), 3276 (1978).
13. L. V. Al'tshuler, S. B. Kormer, A. A. Bakanova, and R. F. Trunin, Zh. Éksp. Teor. Fiz. **38**, 790 (1960) [Sov. Phys. JETP **11**, 573 (1960)].
14. L. V. Al'tshuler, S. E. Brusnikin, and E. A. Kuz'menkov, Prikl. Mekh. Tekh. Fiz., No. 1, 134 (1987).
15. W. J. Nellis, J. A. Moriarty, A. C. Mitchell, *et al.*, Phys. Rev. Lett. **60**, 1414 (1988).

Translated by V. Bukhanov

Doklady Physics, Vol. 47, No. 11, 2002, pp. 783–787. Translated from Doklady Akademii Nauk, Vol. 387, No. 1, 2002, pp. 46–50.

PHYSICS

Superfluidity as an Inviscid Fluid in a Viscous Medium

Yu. L. Klimontovich

Presented by Academician F.V. Bunkin April 7, 2002

Received April 11, 2002

In 1932, Keesom and Clausius observed an anomalous temperature dependence of the specific heat near $T_C = 2.19$ K, which attests a phase transition of the second kind (see [5, 13]).

In 1938, Kapitza [4] discovered that helium was superfluid, i.e., could flow through thin slits and capillaries without friction.

In order to explain this phenomenon, Feynman [15] proposed a two-liquid model of superfluidity, which was improved later by Landau [11]. Analyzing experimental data, Landau determined the form of the collective-excitation spectrum in liquid helium at zero temperature. Along with phenomenological theory, the microscopic theory of superfluidity was developed [1]. Feynman [15] found the relation between the elementary excitation spectrum in liquid helium at $T = 0$ and the statistical form factor of liquid $S(p)$. The nature of the phase transition and existence of an inviscid flow in a viscid medium remain undetermined.

In this paper, I demonstrate that the phase transition in helium is accompanied by not only fast processes but also slow ones ensuring, in particular, spatial coherence on the scale of a slit or capillary. In addition, the structure of viscid friction for low frequencies is rearranged due to the appearance of flicker noise, i.e., the $\frac{1}{f}$ spectrum [7–10]. In this case, the width of the line νk^2 of velocity fluctuations that is typical for high frequencies changes to the frequency ω for low frequencies. As a result, the corresponding distribution over wave numbers is similar to the Bose condensation case; i.e., dispersion is proportional to frequency. The low-frequency (large-time) limit is determined only by the lifetime τ_{life} of a setup.

According to the Ginzburg–Landau model [2, 3, 12], the superfluid state is specified by the effective complex wave function

$$\psi(\mathbf{R}, t) = |\psi| e^{i\varphi}, \quad |\psi|^2 = \frac{N_S}{V} = n_S, \tag{1}$$

where n_S is the atomic density in the superfluid component. The effective wave function of a stationary state satisfies the Ginzburg–Landau equation.

In order to reveal the physical meaning of the coefficients α_L and b of the Ginzburg–Landau equation, we compare susceptibilities calculated for an imperfect Bose gas from the time-dependent Ginzburg–Landau equation and from the quantum kinetic equation in the self-consistent approximation with the effective potential $\nu_{eff}(0)$ [6]. Near the critical point T_C, we have

$$bn = \alpha_L = n|\nu_{eff}(0)| = k_B T_C. \tag{2}$$

Time evolution is described by the kinetic equation for the local distribution function $f(n_S, R, t)$ of the atomic density of the superfluid component [9]. This equation involves, not only the coefficient of the spatial diffusion D and the friction coefficient $\gamma = \frac{\alpha_L}{\hbar}$, but also the second coefficient of diffusion $D_{n_S} = \frac{n}{N_{ph}}$, where N_{ph} is the number of particles in a physically infinitesimal volume, in the n_S space. For convenience, the friction coefficient γ is extracted from this coefficient. In the equilibrium spatially uniform state, the distribution function has the form

$$f_0(n_S) = C\exp\left(-\frac{h_{eff}}{D_{n_S}}\right),$$
$$h_{eff} = \frac{T - T_C}{T_C} n_S + \frac{n_S^2}{2n}, \quad \gamma = \frac{k_B T_C}{\hbar}, \tag{3}$$

where h_{eff} is the effective Hamiltonian per particle. The most probable n_S values are

$$n_{m.p} = 0 \quad \text{for} \quad T - T_C > 0$$
$$\text{and} \tag{4}$$
$$n_{m.p} = n\frac{T_C - T}{T_C} \quad \text{for} \quad T < T_C.$$

Thus, the quantity $n_S^{m.p}$ serves as the order parameter of the Landau theory. For $T < T_C$, we arrive at the

Moscow State University,
Vorob'evy gory, Moscow, 119899 Russia

1028-3358/02/4711-0783$22.00

Gaussian distribution

$$f_0(n_S) = \frac{1}{2\pi\langle(\delta n)^2\rangle}\exp\left(-N_{ph}\frac{(n_S - n_{m.p})^2}{2n^2}\right),$$
$$\langle n_S\rangle = n_{m.p} = n\frac{T_C - T}{T_C}. \quad (5)$$

Therefore, the variance is small and is proportional to the number of particles at a point of a continuous medium, whereas the mean value is determined by the order parameter of the Landau theory.

The kinetic equation in the self-consistent approximation for describing fast processes provides the following equation for the first moment $\langle n_S\rangle$:

$$\frac{d\langle n_S\rangle}{dt} = 2\left[\gamma D_{n_S} - \gamma\left(\frac{T - T_C}{T_C} + \frac{\langle n_S\rangle}{n}\right)\langle n_S\rangle\right] + D\frac{\partial^2\langle n_S\rangle_{R,t}}{\partial\mathbf{R}^2}. \quad (6)$$

For a stationary uniform state, this equation reduces to the equation

$$D_{n_S} - \left(\frac{T - T_C}{T_C} + \frac{\langle n_S\rangle}{n}\right)\langle n_S\rangle = 0,$$
$$D_{N_S} = \frac{n}{N_{ph}}, \quad \gamma = \frac{k_B T_C}{\hbar}, \quad (7)$$

which determines $\langle n_S\rangle$ for any temperature.

Below the critical point of the phase transition, relaxation processes can be divided into fast processes for the particle number density and slow processes for the phase. To describe these processes, we replace the complex wave function $\psi(R, t)$ by the two real field functions

$$\psi(\mathbf{R}, t) = X(\mathbf{R}, t) + iY(\mathbf{R}, t),$$
$$n_S(\mathbf{R}, t) = X^2(\mathbf{R}, t) + Y^2(\mathbf{R}, t).$$

Let us use the corresponding kinetic equation for the distribution function $f(X, Y, \mathbf{R}, t)$ with allowance for spatial diffusion. In application to slow relaxation, the kinetic equation allows the change

$$\frac{T - T_C}{T_C} + \frac{X^2 + Y^2}{n} \longrightarrow \frac{T - T_C}{T_C} + \frac{\langle n_S\rangle}{n}. \quad (8)$$

The equilibrium solution of the kinetic equation has the form of a Gaussian distribution in two variables X and Y.

All the information about the phase transition is contained in the mean number density of superfluid atoms, which is determined for any temperature by solving Eq. (7).

The relaxation and correlation characteristics change substantially when passing through the critical point. States for $T > T_C$ are characterized by fast processes. In addition to fast fluctuations, slow fluctuations arise at the phase transition to the superfluid state. These fluctuations ensure the coherence of the motion of liquid-helium atoms in Kapitza experiments for flows through thin slits and capillaries.

For fast processes, the relaxation time and spectral-line width are

$$\frac{1}{\tau_{n_S}}(k) = \Delta_{n_S} = 2\gamma\left(\frac{T - T_C}{T_C} + 2\frac{\langle n_S\rangle_{st}}{n}\right) + Dk^2,$$
$$\gamma = \frac{k_B T_C}{\hbar}. \quad (9)$$

For $k = 0$, the relaxation time increases according to the Curie law as temperature approaches the critical point from above ($T > T_C$), has the finite value τ_{n_S} ($T = T_C$) $\sim \frac{\sqrt{N_{ph}}}{\gamma}$ at the critical point, and decreases according to the Curie law below the critical point.

Static susceptibility is related to the correlation radius of fast processes as

$$r_C^2 = \frac{D}{\gamma}\left(\frac{T - T_C}{T_C} + 2\frac{\langle n_S\rangle_{st}}{n}\right)^{-1}. \quad (10)$$

The quantity r_C^2 increases according to the Curie law as temperature approaches the critical point from above, has the finite value

$$r_C^2\big|_{T = T_C} \sim \frac{D}{\gamma}\sqrt{N_{ph}} \quad (11)$$

at the critical point, and decreases according to the Curie law below the critical point.

Thus, the time and radius of correlation are anomalous only in the critical region. This means that fast processes cannot ensure the coherence of the state for low temperatures.

Slow processes are characterized by the different correlation radius

$$r_C^2 = D\frac{\langle n_S\rangle_{st}}{\gamma D_{n_S}}, \quad (12)$$

which rises according to the Curie law

$$r_C^2 = \frac{D}{\gamma}\frac{T_C}{T - T_C}, \quad T > T_C \quad (13)$$

as temperature approaches the critical point from above in the region where the Landau theory is applicable. At the critical point,

$$r_C^2 = \frac{D}{\gamma}\sqrt{N_{ph}}, \quad T = T_C. \quad (14)$$

For temperatures below the critical point,

$$r_C^2 = \frac{D}{\gamma}\frac{T_C - T}{T_C}N_{ph}, \quad T < T_C. \tag{15}$$

Thus, in contrast to fast processes, r_C^2 does not decrease according to the Curie law but continues to increase with decreasing temperature. In this case, the quantity r_C^2 is proportional to N_{ph} and, therefore, is much larger than its microscopic value $\sqrt{\frac{D}{\gamma}}$.

The above formulas indicate that the fast-to-slow relaxation-time ratio above the critical point is about $\frac{1}{N_{ph}}$. Thus, long-lived correlations arise at the critical points. Superfluidity in the Kapitza experiments is possible only due to slow fluctuations.

The term "superfluidity," introduced by Kapitza, points to the hydrodynamic nature of this phenomenon. In view of this circumstance, two questions arise.

(i) Why is an inviscid flow possible in a dissipative medium?

(ii) What is the physical difference between superfluid and normal components in helium hydrodynamics?

The de Broglie wavelength $\lambda_B^{(T)}$ in liquid helium is about the mean atomic spacing r_{av}. However, both these values in a continuous medium are much smaller than the physically infinitesimal scale l_{ph}, because each point of this medium involves many atoms. For this reason, contributions determined by Planck's constant are not necessarily substantial either in the kinetic equation or in the corresponding hydrodynamic equations.

In order to take both dynamic and dissipative components into account, one has to use the corresponding generalized kinetic equation, which includes both dynamics and reaction–diffusion dissipation [9].

Based on this kinetic equation for the local distribution function $f(X, Y, R, v, t)$, we construct the hydrodynamic equations. In the self-consistent approximation, the continuity equation has the form

$$\frac{\partial}{\partial t}\langle n_S\rangle_{R,t} + \frac{\partial}{\partial \mathbf{R}}\mathbf{j}_S(R,t) = 2\left[D_{n_S} - \gamma\left(\frac{T - T_C}{T_C} + \frac{\langle n_S\rangle_{R,t}}{n}\right)\langle n_S\rangle_{R,t}\right], \tag{16}$$

where the matter flux

$$j_S(\mathbf{R},t) = \langle n_S\rangle_{R,t}\mathbf{u}_S(\mathbf{R},t) - D\frac{\partial\langle n_S\rangle_{\mathbf{R},t}}{\partial \mathbf{R}} \tag{17}$$

represents both convective transfer and spatial diffusion. The right-hand side of the continuity equation describes the "chemical reaction" of the creation and annihilation of the superfluid component. For a uniform flow, this equation reduces to the two equations

$$\frac{\partial u_S(\mathbf{R},t)}{\partial \mathbf{R}} = 0, \quad D_{n_S} - \left(\frac{T - T_C}{T_C} + \frac{\langle n_S\rangle}{n}\right)\langle n_S\rangle = 0, \quad D_{n_S} = \frac{n}{N_{ph}}, \tag{18}$$

the second of which coincides with Eq. (9). In view of this circumstance, we arrive at the following Navier–Stokes equation for the velocity of the superfluid component:

$$\frac{\partial \mathbf{u}_S}{\partial t} + \left(\mathbf{u}_S\frac{\partial}{\partial \mathbf{R}}\right)\mathbf{u}_S = \frac{F}{m} + \nu\frac{\partial^2 \mathbf{u}_S}{\partial \mathbf{R}^2}, \quad \mathbf{j}_S(\mathbf{R},t) = \langle n_S\rangle_{R,t}\mathbf{u}_S(\mathbf{R},t). \tag{19}$$

The flux of superfluid helium depends on temperature through the density $\langle n_S\rangle_{R,t}$ according to Eq. (7). In this case, the kinetic coefficients of diffusion, kinematic viscosity, and thermal conductivity are identical; i.e., $D = \nu = \chi$. The nonlinear term can be ignored for velocities u_S much lower than the critical velocity u_C. As a result,

$$\frac{\partial \mathbf{u}_S}{\partial t} = \nu\frac{\partial^2 \mathbf{u}_S}{\partial \mathbf{R}^2}, \quad \mathbf{j}_S(\mathbf{R},t) = \langle n_S\rangle_{\mathbf{R},t}\mathbf{u}_S(\mathbf{R},t) \tag{20}$$

for $F = 0$.

For low frequencies, when the time $\frac{1}{\omega}$ is much larger than the viscous diffusion time $\frac{L^2}{\nu}$, the dissipative term in the equation for the velocity of the superfluid component changes fundamentally due to the appearance of flicker noise, which exists for the frequencies [7, 9]

$$\frac{1}{\tau_{life}} \ll \omega \ll \frac{1}{\tau_\nu} = \frac{\nu}{L^2}; \tag{21}$$

where τ_{life} is the lifetime of the setup. The upper limit of this frequency range is determined by the velocity diffusion time $\tau_\nu = \frac{L^2}{\nu}$, where L is the minimum characteristic scale of the sample. There are the new scale and corresponding volume

$$L_\omega = \sqrt{\frac{\nu}{\omega}} \gg L, \quad V_\omega = L_\omega^3 \gg V. \tag{22}$$

The following two regions are distinguished in the fluctuation spectrum of the velocity u_S:

(i) High frequencies, where time $\frac{1}{\omega}$ is much smaller than the diffusion time. In this case, the typical spectrum is the Rayleigh line.

(ii) Low frequencies, where time $\frac{1}{\omega}$ is much larger than the diffusion time. In this case, multiple diffusion takes place, and the effective diffusion volume $V_\omega = \left(\frac{\nu}{\omega}\right)^{3/2}$ is much larger than the system volume V. The structure of a Langevin source is determined as [7–9]

$$(\delta\mathbf{u}_S\delta\mathbf{u}_S)_{\omega,\mathbf{k}} = \frac{(yy)_{\omega,k}}{\omega^2 + (\nu k^2)^2},$$
$$(yy)_{\omega,\mathbf{k}} = 2\nu k^2 A V_\omega \langle \delta\mathbf{u}_S\delta\mathbf{u}_S\rangle_V \exp\left(-\frac{\nu k^2}{2\omega}\right), \quad (23)$$

where $\langle \delta\mathbf{u}_S\delta\mathbf{u}_S\rangle_V$ is the correlation function of the velocity fluctuations averaged over sample volume and A is the normalization constant. The dispersion of the wave-number distribution is proportional to frequency:

$$\langle(\delta k)^2\rangle \sim \frac{1}{L_\omega^2} = \frac{\omega}{\nu}. \quad (24)$$

Therefore, specific Bose condensation occurs in the flicker-noise region for $\omega \longrightarrow 0$, which indicates that this region is characterized by spatial coherence. The space–time spectral density is expressed as

$$(\delta\mathbf{u}_S\delta\mathbf{u}_S)_{\omega,\mathbf{k}} = \frac{2\nu k^2}{\omega^2 + (\nu k^2)^2} A V_\omega \langle \delta u_S \delta u_S\rangle_V \exp\left(-\frac{\nu k^2}{2\omega}\right). \quad (25)$$

Integrating this expression with respect to k by using the narrowness of the distribution in wavenumbers, we obtain the corresponding time spectral density

$$(\delta\mathbf{u}_S\delta\mathbf{u}_S)_\omega = \frac{\pi\langle \delta\mathbf{u}_S\delta\mathbf{u}_S\rangle_V}{\ln\frac{\tau_{life}}{\tau_\nu}}\frac{1}{\omega},$$
$$\frac{1}{\tau_{life}} \le \frac{1}{\tau_{obs}} \ll \omega \ll \frac{1}{\tau_\nu}. \quad (26)$$

The correlation time for the flicker-noise region is determined as

$$\tau_{cor} = \frac{\int_{\tau_D}^{\tau_{life}} \langle \delta\mathbf{u}_S\delta\mathbf{u}_S\rangle_\tau d\tau}{\langle \delta\mathbf{u}_S\delta\mathbf{u}_S\rangle_{\tau_D}} \sim \frac{\tau_{life}}{\ln\frac{\tau_{life}}{\tau_\nu}} \quad (27)$$

and increases infinitely with the lifetime τ_{life}.

In the flicker-noise region, the dissipation factor νk^2 in the Fourier transform of Eq. (20) for the velocity of superfluid helium is replaced by ω. Since the minimum frequency is determined by the lifetime τ_{rel}, the slowest relaxation is described by the equation

$$\frac{\partial\mathbf{u}_S}{\partial t} = -\frac{1}{\tau_{rel}}\mathbf{u}_S. \quad (28)$$

In the zeroth approximation in the dimensionless parameter $\frac{\tau_{obs}}{\tau_{life}}$, dissipation can be ignored in this equation. In this case, we arrive at the equation

$$\frac{\partial\mathbf{u}_S}{\partial t} = 0, \quad \mathbf{u}_S = \text{const}. \quad (29)$$

This constant velocity is determined by the boundary condition at the ends of the capillary, e.g., by the density difference. The lower limit of the time of observing the flicker noise is $(\tau_{obs})_{min} \ge \tau_\nu = \frac{d^2}{\nu} \sim 10^{-5}$–$10^{-6}$ s.

We arrive at the following two basic conclusions.

1. For $T < T_C$, there are two types of relaxation and fluctuation processes: fast and slow. The radius and time of correlation for fast processes increase according to the Curie law when approaching the critical point but have finite values at the critical point. As temperature decreases below the critical point, this correlation radius again becomes about the mean interatomic spacing. For this reason, fast fluctuations cannot ensure the coherence of the asymmetric phase at macroscopic scales.

In contrast, slow fluctuations for $T < T_C$ become macroscopic and, therefore, ensure the spatial coherence of the superfluid component in Kapitza experiments.

2. Inviscid, i.e., superfluid, motion in a viscous medium is possible due to the appearance of the coherent distribution in wave numbers for low frequencies. For this reason, the hydrodynamic dissipation in the equations for Fourier components is rearranged: the hydrodynamic friction νk^2 is replaced by ω.

The normal motion is described by the Navier–Stokes equation. The characteristic frequencies of the fluctuation spectrum and relaxation are determined by viscosity as $\omega \sim \nu k^2$. The characteristic frequencies of the superfluid motion lie in the flicker-noise region. The lower limit of the frequency range is determined by the inverse lifetime of a setup, which attests an inviscid flow.

Separation into two independent flows is possible only in the linear approximation. The superfluid flow is broken when it begins to generate vortex motion of the normal component. The corresponding maximum velocity of inviscid flow is $u_C \sim \frac{\hbar}{md}$, which corresponds to the familiar estimate of the critical velocity.

REFERENCES

1. N. N. Bogolyubov, Izv. Akad. Nauk SSSR, Ser. Fiz. **11**, 7 (1947).
2. V. L. Ginzburg and L. D. Landau, Zh. Éksp. Teor. Fiz. **20**, 106 (1950).
3. V. L. Ginzburg and A. A. Sobyanin, Usp. Fiz. Nauk **120**, 153 (1976) [Sov. Phys. Usp. **19**, 773 (1976)].
4. P. L. Kapitsa, Dokl. Akad. Nauk SSSR **18** (1), 21 (1938); Nature **141**, 74 (1938).
5. W. Keesom, *Helium* (Elsevier, Amsterdam, 1942; Inostrannaya Literatura, Moscow, 1949).
6. Yu. L. Klimontovich and V. P. Silin, Zh. Éksp. Teor. Fiz. **23**, 151 (1952); Usp. Fiz. Nauk **70**, 247 (1960).
7. Yu. L. Klimontovich, Pis'ma Zh. Éksp. Teor. Fiz. **51**, 43 (1990) [JETP Lett. **51**, 51 (1990)]; Physica A (Amsterdam) **167**, 782 (1990).
8. Yu. L. Klimontovich, *Statistical Physics* (Nauka, Moscow, 1982; Harwood Academic, New York, 1986).
9. Yu. L. Klimontovich, *Statistical Theory of Open Systems* (Yanus, Moscow, 1995–2001; Kluwer, Dordrecht, 1995–2001), Vols. 1–3.
10. Sh. M. Kogan, Usp. Fiz. Nauk **145**, 285 (1985) [Sov. Phys. Usp. **28**, 171 (1985)].
11. L. D. Landau, Zh. Éksp. Teor. Fiz. **11**, 592 (1941); **14**, 112 (1944).
12. E. M. Lifshitz and L. P. Pitaevskiĭ, *Course of Theoretical Physics*, Vol. 5: *Statistical Physics* (Nauka, Moscow, 1978; Pergamon, Oxford, 1980), Part 2.
13. F. London, *Superfluidity* (Wiley, New York, 1950).
14. Ph. Nozieres and D. Pines, *Theory of Quantum Liquids*, Vol. II: *Superfluid Bose Liquids* (Addison-Wesley, Reading, 1980).
15. R. P. Feynman, *Statistical Mechanics: a Set of Lectures* (Benjamin, Reading, 1972; Mir, Moscow, 1974).

Translated by R. Tyapaev

Doklady Physics, Vol. 47, No. 11, 2002, pp. 788–790. Translated from Doklady Akademii Nauk, Vol. 387, No. 1, 2002, pp. 51–53.

PHYSICS

High-Amplitude Precession and Dynamic Insensitivity of the Spin System of Bilayer Films with Antiferromagnetic Coupling

D. I. Sementsov* and A. M. Shutyĭ**

Presented by Academician V.V. Osiko July 2, 2002

Received June 17, 2002

Recently, the static and dynamic properties of multilayer magnetically coupled systems have attracted increased attention [1–3]. When these structures are exposed to an rf field, dynamic modes, where the amplitude of the magnetization precession angle increases sharply, are of particular interest [4–6]. For the resonance excitation of spin-subsystem precession in both single-layer and multilayer thin films, an rf field perpendicular to the static bias field is usually used [7–9]. However, in bilayer structures with antiferromagnetic coupling, the magnetic subsystem can be excited more efficiently in a wide frequency band by a longitudinal alternating field. In this study, new dynamic precession modes of layer magnetizations in a magnetically coupled system of this type in a longitudinal rf field are revealed. These modes are characterized by high precession amplitudes and are efficiently controlled by an external bias field. We observed a new effect of dynamic insensitivity of the magnetic subsystem to the perturbing action of the alternating field.

We consider a structure consisting of two ferromagnetic-metal layers separated by a nonmagnetic layer. Each layer has thickness d_i, magnetization $\mathbf{M}_i$, and plane uniaxial anisotropy with constant K_i. The external bias $\mathbf{H}$ and rf $\mathbf{h}(t)$ fields are directed along the coinciding axes of the easy magnetization of layers. The magnetic-subsystem energy per unit film area is

$$E = \sum_{i=1,2} d_i\{K_i\sin^2\varphi_i - (H+h)M_i\cos\varphi_i\cos\psi_i - 2\pi M_i^2\cos^2\psi_i\} + AM_1M_2d_{12}[\cos\psi_1\cos\psi_2 \times\cos(\varphi_1-\varphi_2) + \sin\psi_1\sin\psi_2], \quad (1)$$

where $d_{12} = d_1d_2(d_1+d_2)^{-1}$ is the reduced thickness of two magnetic layers; $A > 0$ is the coupling constant of the magnetic layers, which generally depends on the thickness, material, and structural characteristics of the separating layer; and the azimuth angle φ_i, measured from the *y* axis, and exit angle ψ_i, from the film plane, specify the directions of $\mathbf{M}_i$ in the horizontal and vertical planes.

Equations of motion for magnetizations $\mathbf{M}_i$ are taken in the following Landau–Lifshitz form in spherical coordinates:

$$\dot\varphi_iM_id_i\sin\psi_i = \gamma\frac{\partial E}{\partial\psi_i} + \frac{\lambda_i}{M_i}\frac{1}{\sin\psi_i}\frac{\partial E}{\partial\varphi_i},$$
$$\dot\psi_iM_id_i = \frac{\lambda_i}{M_i}\frac{\partial E}{\partial\psi_i} - \gamma\frac{1}{\sin\psi_i}\frac{\partial E}{\partial\varphi_i}, \quad (2)$$

where γ is the gyromagnetic ratio and λ_i is the damping factor in the *i*th layer [7]. We use parameters close to the parameters of actual permalloy-class films: $\lambda_1 = \lambda_2 = 5\times10^7$ Hz, $H_{k1} = 10$ Oe, $4\pi M_1 = 1.1\times10^4$ G, $H_{k2} = 5$ Oe, $4\pi M_2 = 8\times10^3$ G, $\lambda = 1.76\times10^7$ (Oe s)$^{-1}$, and $d_1 = d_2 = 0.1$ μm. Since demagnetizing fields are strong for the films under investigation ($4\pi M_i \gg H_{ki}, AM_i$), the amplitude of polar-angle oscillations is always much lower than the amplitude for the azimuth angle.

In view of Eq. (1), the equilibrium conditions for layer magnetizations, $\frac{\partial E}{\partial\varphi_i} = 0$ and $\frac{\partial^2 E}{\partial\varphi_i^2} > 0$, reduce to the set of equations

$$K_i\sin2\varphi_{0i} + HM_i\sin\varphi_{0i} - Ad_{3-i}(d_1+d_2)^{-1} \times M_1M_2\sin(\varphi_{0i}-\varphi_{03-i}) = 0,$$
$$H_{ki}\cos2\varphi_{0i} + H\cos\varphi_{0i} - Ad_{3-i}(d_1+d_2)^{-1} \times M_{3-i}\cos(\varphi_{0i}-\varphi_{03-i}) > 0, \quad i = 1,2. \quad (3)$$

The analysis of these conditions indicates [10] that orientational phase transitions, where layer magnetizations change their orientations stepwise, occur in the systems under consideration for certain values of the

Ul'yanovsk State University, ul. L'va Tolstogo 42, Ul'yanovsk, 432700 Russia

** e-mail: sdi@sdi.ulsu.ru*

*** e-mail: shuty@mail.ru*

1028-3358/02/4711-0788$22.00

longitudinal bias field **H**. Near these values of the field **H**, there are the most favorable conditions under which a weak rf field **h** excites various dynamic modes sensitive to small variations in the parameters of the system and field magnitudes. Variations in the bias-field magnitude were found to give rise to orientational hysteresis loops that are different in shape and whose width depends in particular on the coupling constant A. As A increases, the width of a hysteresis loop decreases down to fractions of an oersted. For the efficient excitation of magnetic oscillations in the longitudinal alternating field, one must use systems where narrow ($\Delta H \leq$ 1 Oe) hysteresis loops occur. In this case, the bias-field magnitude must be either inside the loop or close to its critical values.

Figure 1 shows the time dependences of the azimuth angles of the magnetic moments of the layers for A = 0.05, frequencies ω = (a) 0.1×10^8 and (b) 1.7×10^8 Hz, rf-field amplitude h = 1 Oe, and bias-field magnitude H = 19 Oe. As is seen, a pulse mode of oscillations with short transient sections and period T_h of the alternating field arises for low frequencies (Fig. 1a). The amplitude of this mode is determined by the difference between the angles of the equilibrium stationary positions for given H and A ($\varphi_{01} \approx 0, \mp 30°$; $\varphi_{02} \approx 180°, \pm 89°$) and depends only slightly on the alternating-field amplitude h. Oscillations of the magnetic moment of each layer occur between two potential wells, and the rf field disturbs the system from the equilibrium state and compensates losses in the energy of precession. For A = 0.05, this oscillation mode occurs at the minimum amplitude of the alternating field $h_{\min} \approx 0.7$ Oe. The increase in h up to 1 Oe or higher does not noticeably change the parameters of the mode. As the coupling constant A increases, the threshold alternating field decreases due to narrowing of the orientational hysteresis loop, and $h_{\min} \approx 0.4$ Oe for A = 0.06. The relative pulse duration of oscillations in this mode can be controlled by varying the bias field. In particular, when H is shifted to the left edge of the hysteresis loop (H = 18.3 Oe), the duration of the pulse decreases as is shown by the dashed line in Fig. 1a. Since two noncollinear equilibrium orientations exist in addition to the equilibrium orientation with opposite magnetic moments [10], two remagnetization modes—in the directions $0 < \varphi_2 < \pi$ and $-\pi < \varphi_2 < 0$ with the corresponding remagnetization of the first film—are equiprobable. However, only one of these transitions is realized for the pulse mode.

As the alternating-field frequency increases, arbitrary time intervals involving a number of periods of either oscillations symmetric about the $\varphi = 0$ direction begin to alternate. As a result, chaotic oscillation modes develop.

In the frequency band $\omega \sim (7–17) \times 10^8$ Hz, a steady-state high-amplitude oscillation mode occurs with the double period $2T_h$ [function $h(t)$ is shown by the dashed line in Fig. 1b] and with an amplitude that is almost

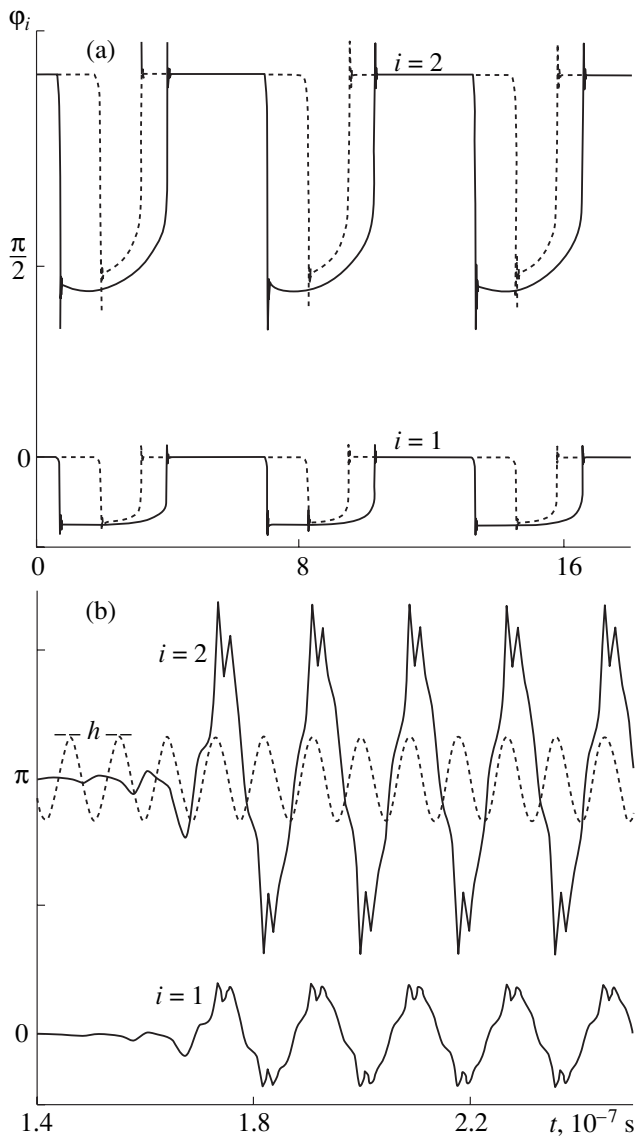

Fig. 1. Time dependence of the azimuth angles of the magnetic moments of the layer for the longitudinal perturbing fields whose frequencies correspond to high-amplitude precession modes.

double the amplitude of the pulse mode (Fig. 1a). In this case, chaotic oscillations of magnetic moments occur in certain regions of this frequency band, whereas the system is insensitive to the alternating field in the band $\omega_n \sim (7.5–8) \times 10^{-8}$ Hz. The period of the steady-state high-amplitude oscillations has several minima and maxima (Fig. 1b) in the frequency band below the dynamic insensitivity range and has only one minimum and one maximum above the dynamic insensitivity range, where it is also double the period of the rf field.

Figure 2 shows the functions $\varphi_i(t)$ for the above fields, coupling constant, and ω = (*1*) 7.15×10^8, (*2*) 7.4×10^8, and (*3*) 7.5×10^8 Hz. As is seen, the dynamic insensitivity range follows the region with

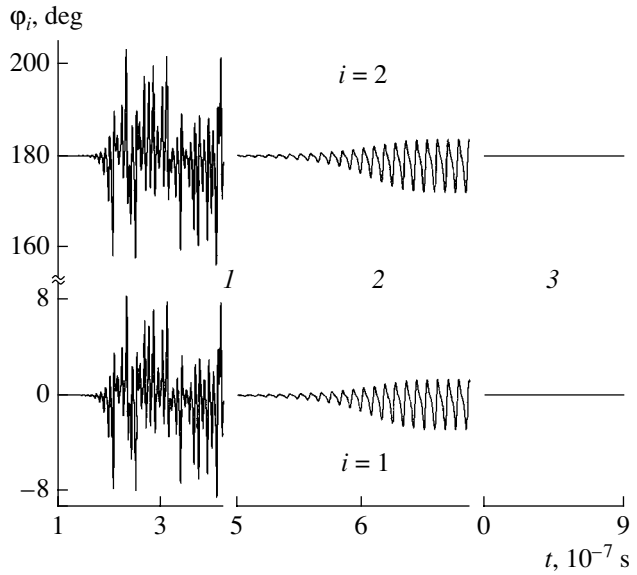

Fig. 2. Dynamic modes of the magnetic moments of the layers for frequencies near the dynamic insensitivity range and the time dependence of the azimuth angles in the dynamic insensitivity range.

chaotic oscillations (lines *1*), which transform with increasing frequency to low-amplitude regular oscillations with the period of the rf field (lines *2*). When approaching the dynamic insensitivity range, the amplitude of regular oscillations decreases down to zero (lines *3*). Variation in the amplitude of the rf field results in a shift of the dynamic insensitivity range. In particular, the dynamic insensitivity range for $h = 0.8$ Oe corresponds to the frequency band $\omega_n \sim (6.8\text{–}7.5) \times 10^8$ Hz. We note that the maximum angles of magnetic-moment precession for a transverse field of the same amplitude and frequency are no more than 10°.

In summary, the above analysis indicated that the use of a longitudinal rf field to excite stratified antiferromagnetically coupled structures considerably extends the frequency band where high-amplitude precession modes occur to the low-frequency region. A frequency region where the magnetically coupled system is dynamically insensitive to the alternating field was found.

REFERENCES

1. A. K. Kazansky and V. M. Uzdin, Phys. Rev. B **52**, 9477 (1995).
2. V. V. Ustinov, M. M. Kirilova, I. V. Lobov, *et al.*, Zh. Éksp. Teor. Fiz. **96** (2), 477 (1996) [JETP **82**, 253 (1996)].
3. V. V. Kostyuchenko and A. K. Zvezdin, Phys. Rev. B **57**, 5951 (1998).
4. B. Neite and H. Doetsch, J. Appl. Phys. **62** (2), 648 (1987).
5. A. G. Temiryazev, M. P. Tikhomirova, and A. V. Maryakhin, in *Proceedings of the International School-Workshop on Novel Magnetic Materials for Microelectronics, NMMM-XVI, Moscow, 1998*, Part 1, p. 270.
6. A. M. Shutyĭ and D. I. Sementsov, Zh. Éksp. Teor. Fiz. **118** (3), 610 (2000) [JETP **91**, 531 (2000)].
7. A. G. Gurevich and G. A. Melkov, *Magnetic Oscillations and Waves* (Nauka, Moscow, 1994).
8. Yu. V. Kornev, D. I. Sementsov, and V. V. Sidorenkov, Dokl. Akad. Nauk SSSR **295** (5), 1114 (1987) [Sov. Phys. Dokl. **32**, 682 (1987)].
9. S. M. Resende and F. M. de Aguiar, Proc. IEEE **78** (6), 5 (1990).
10. D. I. Sementsov and A. M. Shutyĭ, Pis'ma Zh. Éksp. Teor. Fiz. **74** (6), 339 (2001) [JETP Lett. **74**, 306 (2001)].

Translated by R. Tyapaev

Doklady Physics, Vol. 47, No. 11, 2002, pp. 791–797. Translated from Doklady Akademii Nauk, Vol. 387, No. 1, 2002, pp. 54–60.

PHYSICS

A New Type of Boron–Oxygen Framework in the $Na_3(NO_3)[B_6O_{10}]$ Crystal Structure

O. V. Yakubovich, I. V. Perevoznikova, O. V. Dimitrova, and Corresponding Member of the RAS V. S. Urusov

Received February 18, 2002

The history of boron atoms in the Earth's crust, in which they occupy the 22nd place on the atomic clarke scale (5×10^{-3}%) [1], is mainly associated with their oxygen compounds. The overwhelming majority of boron minerals are borates, i.e., salts of boric acid and its derivatives. To date, the crystal structures of more than 100 borate minerals and more than 1000 synthetic inorganic borates have been interpreted [2]. The intrinsic features of crystal chemistry for compounds of such a class are associated with the possibility of double boron coordination by oxygen atoms over both a triangle and a tetrahedron. The capability for polymerization of coordination B polyhedra (triangles and tetrahedra) is well known and manifests itself in a great variety of boron–oxygen anion radicals.

Sodium, together with magnesium, calcium, manganese, and iron, belongs to the basic cations of borate minerals. Crystal structures with complicated boron–oxygen constructions involving triangles and tetrahedra (varied from island to layered structures) are typical of natural sodium borates. According to our data, no sodium minerals whose structures were formed by isolated boron–oxygen triangles or tetrahedra are found. The only exception is the $Na_2[B(OH)_4]Cl$ teepleite mineral [3] with isolated $B(OH)_4$ tetrahedron complexes [3]. On the other hand, sodium borates possessing the maximal degree of anion polymerization (i.e., framework structures) are not found in nature. However, these are framework that are rather interesting, since the anion structures, being the basis of so-called technological crystals, often manifest promising physical properties. For example, nonlinear optical properties are found for LiB_3O_5 and $CsLiB_6O_{10}$ synthetic framework borates [4, 5].

In this paper, we present the results of our studies of colorless transparent prismatic crystals with longitudinal length up to 3 mm (Fig. 1). The crystals were obtained by soft hydrothermal synthesis (T = 280°C, P = 70 atm) in standard (fettled by teflon) autoclaves with volumes of ~5–6 cm^3. The duration of the experiment was 18–20 days. The crystals were formed for the mass-component ratio NaCl : B_2O_3 = 1 : 2. Nitrogen acid (0.1 M) was used as a mineralizer. Individual features of the diffraction pattern recorded by a DRON UM diffractometer for a powder sample attested the original nature of the synthesized compound. X-ray spectral analysis with a CamScan 4DV analyzer showed the presence of sodium atoms in the composition of the given phase. (The possibility to determine the presence of chemical elements with atomic numbers less than 11 is limited by the technical properties of the device used.)

Parameters of a unit cell [a = 12.589(3) Å; b = 10.015(2) Å; c = 7.679(2) Å] and crystal orthorhombic symmetry were determined by the photographic method with a rotating-crystal X-ray camera. The results obtained were then refined with the help of a four-circle automated SYNTEX P1 diffractometer. Experimental data required for determining the struc-

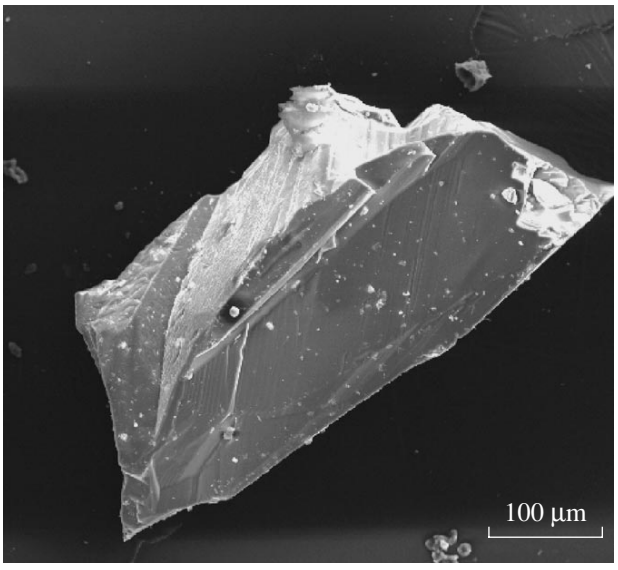

Fig. 1. Exterior view of $Na_3(NO_3)[B_6O_{10}]$ single crystal. The photograph was obtained using a scanning electron microscope.

Moscow State University, Vorob'evy gory, Moscow, 119899 Russia

1028-3358/02/4711-0791$22.00

Table 1. Crystallographic characteristics, experimental data, and structure refinements

Crystallographic characteristics	
Chemical formula	$Na_3(NO_3)[B_6O_{10}]$
Absorption μ, mm^{-1}	0.34
Crystallographic space group	*Pnma*
Number of formula units *Z*	4
Parameters of a unit cell, Å	
a	12.589(3)
b	10.015(2)
c	7.679(2)
Unit-cell volume *V*, $Å^3$	968.2(4)
Density ρ, g cm^{-3}	2.441
Experimental data	
Diffractometer	SYNTEX $P\bar{1}$
Radiation	MoK_α (graphite monochromator)
Temperature, K	293
Region of recording, angular θ_{max} degrees	30.00
Data for the structure refinement	
Number of reflections: independent/observed with $I > 1.96\sigma(I)$	1181/1090
Refinement method	over F^2
Number of parameters to be refined	119
Correction for absorption	DIFABS
T_{max}, T_{min}	1.000, 0.380
Residuals	
R (for reflections observed)	0.045
wR_2 (for all independent reflections)	0.118
s	1.070
Extinction coefficient	0.003(2)
Residual electron density, e/$Å^3$	$\rho_{max} = 0.402$, $\rho_{min} = -0.417$

ture were obtained by $2\theta : \theta$ scanning with the same diffractometer using the MoK_α line. The reflection intensities recorded were corrected for the Lorentz factor and the polarization effect.

All calculations were performed using the SHELX software package [6, 7]. In this case, the atomic-scattering curves and corrections for the anomalous dispersion taken from [8] were used. The crystal structure was determined by direct methods and, furthermore, was refined in the full-matrix anisotropic approximation, with absorption and secondary isotropic extinction taken into account. Identifying atoms in the absence of chemical-analysis data, we allowed for the composition of the system under investigation (which had been used when synthesizing crystals), the values of interatomic distances, temperature factors, and the shape of thermal-oscillation ellipsoids. The structure determined is described by the chemical formula $Na_3(NO_3)[B_6O_{10}]$. The crystallographic characteristics of the new phase, data from X-ray measurements, and structure refinement parameters are presented in Table 1. Data for basis-atom coordinates with equivalent temperature coefficients and atomic distances are given in Tables 2 and 3, respectively. The results of the bond-valence analysis [9] are seen from Table 4.

Two types of boron polyhedra participate in the formation of the crystal structure, namely, triangles and tetrahedra. In the B1 tetrahedron, interatomic cation–oxygen distances vary from 1.445 to 1.511 Å (the average value is 1.469 Å). In B2 tetrahedra, they vary from

Table 2. Coordinates of basis atoms and equivalent thermal parameters

Atom	*x*/*a*	*y*/*b*	*z*/*c*	U_{equiv}, Å^2
B1	0.1673(2)	0.1203(2)	0.2728(3)	0.0118(5)
B2	0.3139(3)	0.25	0.4415(5)	0.0111(6)
B3	0.0003(3)	0.25	0.2194(5)	0.0138(7)
B4	0.2594(2)	0.0202(2)	0.5261(3)	0.0136(5)
N	0.0521(3)	0.25	0.7135(4)	0.0215(6)
Na1	0.5	0.0	0.0	0.0233(4)
Na2	0.0	0.0	0.0	0.0255(4)
Na3	0.2856(1)	0.25	0.8805(2)	0.0266(4)
O1	0.2064(2)	0.25	0.3502(3)	0.0094(4)
O2	0.1812(1)	0.0154(2)	0.4017(2)	0.0142(3)
O3	0.0532(1)	0.1309(2)	0.2372(2)	0.0148(3)
O4	0.2263(1)	0.0953(2)	0.1149(2)	0.0161(4)
O5	0.3211(1)	0.1308(2)	0.5514(2)	0.0225(4)
O6	−0.0180(2)	0.25	0.5976(4)	0.0331(7)
O7	−0.1047(2)	0.25	0.1883(4)	0.0305(7)
O8	0.0872(2)	0.1416(2)	0.7670(3)	0.0450(7)

Table 3. Interatomic distances, Å

B1-tetrahedron		B2-tetrahedron		B3-triangle		B4-triangle	
B1–O4	1.445(3)	B2–O7	1.430(4)	B3–O7	1.342(4)	B4–O4	1.354(3)
O2	1.454(3)	O5	1.465(3) × 2	O3	1.373(2) × 2	O5	1.367(3)
O3	1.466(3)	O1	1.524(4)			O2	1.372(3)
O1	1.511(3)						
Average value:	1.469	Average value:	1.471	Average value:	1.363	Average value:	1.364
N-triangle		Na1-eight-vertex polyhedron		Na2-octahedron		Na3-nine-vertex polyhedron	
N–O8	1.242(3) × 2	Na1–O2	2.408(2) × 2	Na2–O3	2.342(2) × 2	Na3–O6	2.479(3)
O6	1.253(4)	O3	2.498(2) × 2	O8	2.533(2) × 2	O4	2.489(2) × 2
Average value:	1.246	O6	2.623(1) × 2	O5	2.636(2) × 2	O2	2.695(2) × 2
		O8	2.724(3) × 2			O5	2.830(2) × 2
						O8	2.860(3) × 2
		Average value:	2.563	Average value:	2.504	Average value:	2.692

1.430 to 1.524 Å (the average value is 1.471 Å). Although the average values for boron–oxygen bond lengths in tetrahedron groupings coincide to within an accuracy of 0.001 Å, we can see that the spread of interatomic distances in B2 tetrahedra is larger. A similar conclusion follows from the analysis of cation–oxygen bond lengths in boron triangles. For example, for virtually equal average values of interatomic B–O distances (equal to 1.363 and 1.364 Å) in crystallographically independent B3 and B4 triangles, the B3 polyhedra are more strongly distorted. The interatomic B3–O distances lie within the interval 1.342–1.373 Å, whereas in B4 triangles the minimum and maximum B4–O distances are 1.354 and 1.372 Å. If any intrinsic symmetry

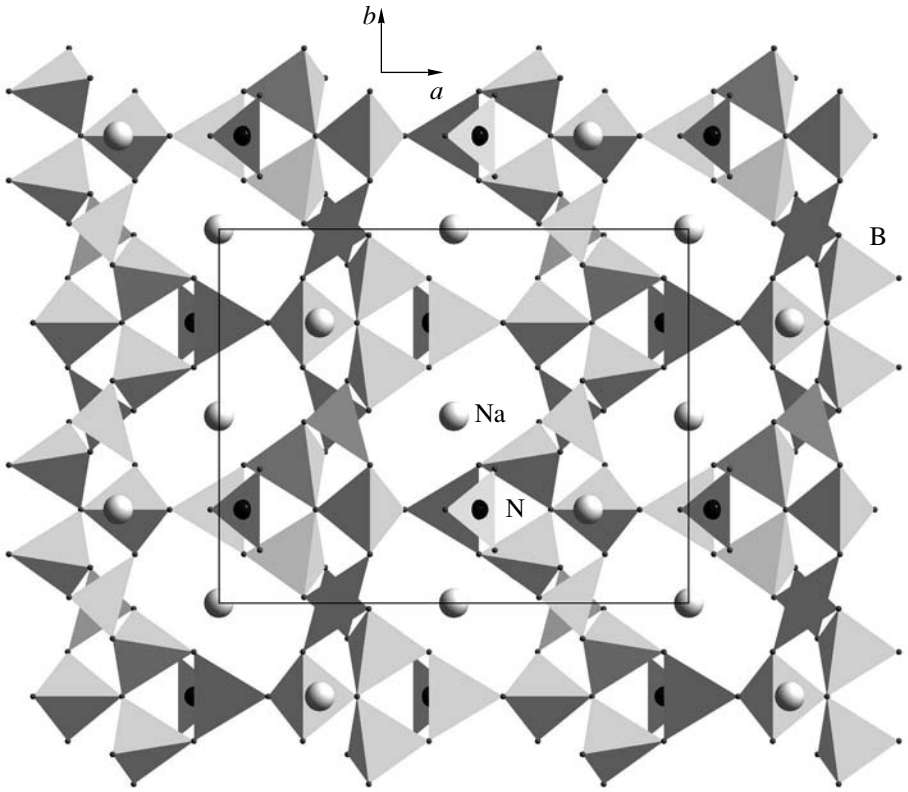

Fig. 2. $Na_3(NO_3)[B_6O_{10}]$ crystal structure in the *xy* projection. The composition of a hexaborate complex consisting of three tetrahedra and three triangles and the character of its polymerization accompanied by the formation of the three-dimensional microporous framework are clearly seen.

is absent for the B4 triangle or B1 tetrahedron, then the B2 and B3 polyhedra are described by their own C_s symmetry.

Smaller NO_3 triangles that have also been found in this structure are close to regular ones. The spread for the N–O bond lengths attains 1.242 and 1.253 Å, the average length being 1.246 Å.

Three independent sodium atoms are characterized by coordination numbers 6, 8, and 9. Cation–oxygen interatomic distances in Na2 octahedra (with the C_i

Table 4. Bond-valence analysis*

Atom	N	B1	B2	B3	B4	Na1	Na2	Na3	Σ	|δ|
O1		0.68 × 2	0.66						2.02	0.02
O2		0.80			1.00	0.19 (0.19)		0.09 (0.09)	2.08	0.08
O3		0.77		0.99 (0.99)		0.15 (0.15)	0.23 (0.23)		2.14	0.14
O4		0.82			1.05			0.16 (0.16)	2.03	0.03
O5			0.78 (0.78)		1.01		0.11 (0.11)	0.06 (0.06)	1.96	0.04
O6	1.62					0.11 × 2		0.16	2.00	0.00
O7			0.85	1.08					1.93	0.07
O8	1.67 (1.67)					0.08 (0.08)	0.14 (0.14)	0.06 (0.06)	1.95	0.05
Σ	4.96	3.07	3.07	3.06	3.06	1.06	0.96	0.90		

* The balance is calculated on the basis of the relationship $s_{ij} = \exp\frac{R_1 - R_{ij}}{b}$, where s_{ij} is the valence force transferred from the *i*th cation to the *j*th anion, R_1 is the bond length of a unit valence for a particular cation–anion pair (tabulated value or empirical constant), R_{ij} is the measured cation–anion interatomic distance in a particular crystal structure, and $b = 0.37$.

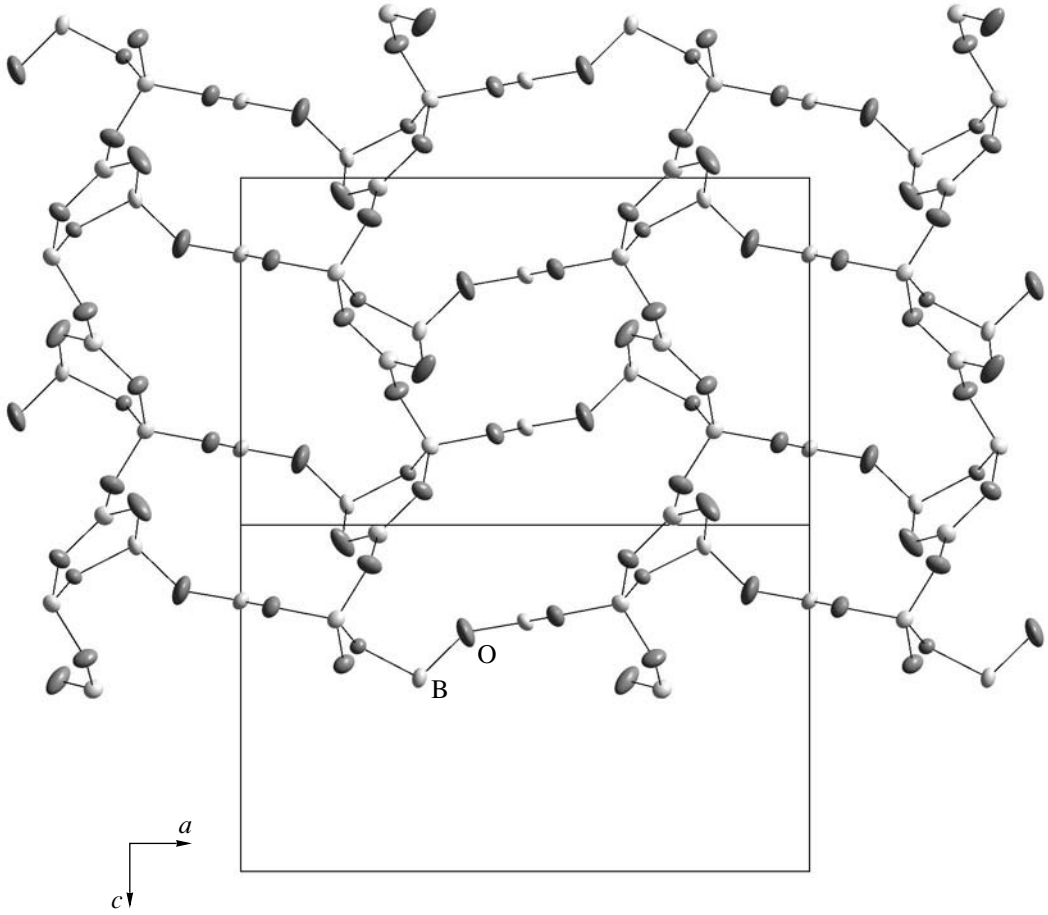

Fig. 3. Ellipsoids of atomic thermal oscillations in the zeolite-like boron–oxygen framework in the *xz* projection (70% probability).

intrinsic symmetry) vary from 2.342 to 2.636 Å (the average value is 2.504 Å), while in the central-symmetric Na1 eight-vertex polyhedra, from 2.408 to 2.724 Å (the average value is 2.553 Å). At the same time, in Na3 nine-vertex polyhedra with their intrinsic C_s symmetry, they vary from 2.479 to 2.860 Å (the average value is 2.692 Å).

One of the features of the new nitrate–borate crystal structure is the grouping of three boron tetrahedra around a common oxygen atom. BO_3 triangles are connected to two free vertices of each of the tetrahedra in this group. As a result, anion fragments of a mixed type, which consist of tetrahedra and triangles, are formed. These fragments can be described as quasi-clusters consisting of three inderite rings.[1] Each of these rings is formed by two tetrahedra and a triangle coupled into a unified complex via a common vertex of the three tetrahedra (Fig. 2). One oxygen vertex of each tetrahedron which is not shared among other polyhedra of the given complex is shared with a free oxygen vertex of the triangle in a neighboring complex. This process is accompanied by the formation of a three-dimensional zeolite-like framework structure that is described by the formula $[B_6O_{10}]^{2-}_{\infty\infty\infty}$ (Fig. 3). Isolated triangular groupings $(NO_3)^-$ and Na^+ turn out to be captured by a microporous framework. In this case, Na^+ cations screen oxygen atoms of the nitrate triangles from the cations of the boron–oxygen framework. As a result, complicated $[Na_3(NO_3)]^{2+}$ cation complexes are formed in voids of the open anion framework formed by boron tetrahedra and triangles (Fig. 4).

The six-link group consisting of three B tetrahedra with a common vertex and three B triangles that connect the tetrahedra pairwise from outside is the simplest framework-structural element. This group was first discovered in the tunellite mineral structure [10] and is now well known in borate crystal chemistry [11]. In the crystal structures of the minerals

aksaite $Mg[B_6O_7(OH)_6] \cdot 2H_2O$,

admontite $Mg[B_6O_7(OH)_6] \cdot 4H_2O$ [12],

mcallisterite $Mg_2[B_6O_7(OH)_6]_2 \cdot 9H_2O$,

rivadavite $Na_6Mg[B_6O_7(OH)_6]_4 \cdot 10H_2O$ [2],

[1] Borate complex anions consist of two vertex-coupled tetrahedra and one triangle. These anions were first determined in the inderite mineral.

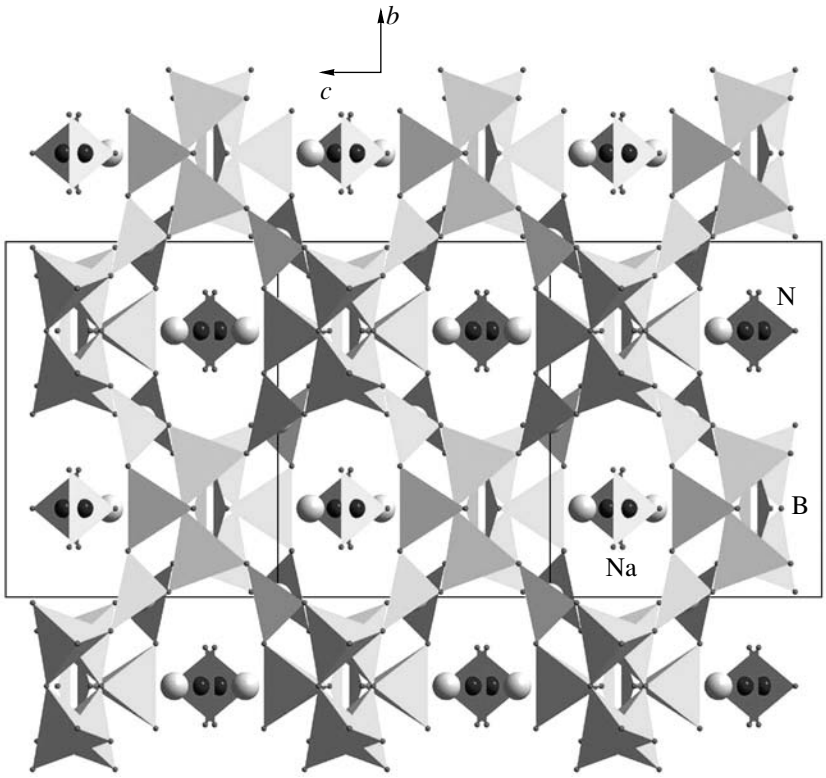

Fig. 4. Distribution of sodium cations and nitrate triangular groups in voids of the $Na_3(NO_3)[B_6O_{10}]$ open microporous framework (*yz* projection).

and in the $Mg[B_6O_7(OH)_6] \cdot 3H_2O$

synthetic compound, the above-described six-nuclear complexes consisting of three triangles and three tetrahedra are isolated. In other words, they form $[B_6O_7(OH)_6]$ island groupings in which vertices of the triangles and tetrahedra which are not shared between boron atoms are occupied with (OH) groups.

The $[B_6O_7(OH)_6]^{2-}$ island anion is the first term of the row [13]

$$[B_6O_7(OH)_6]^{2-} - (H_2O) \Rightarrow [B_6O_8(OH)_4]^{2-}_{\infty}$$

$$- (H_2O) \Rightarrow [B_6O_9(OH)_2]^{2-}_{\infty\infty} - (H_2O) \Rightarrow [B_6O_{10}]^{2-}_{\infty\infty\infty},$$

in which the group consisting of three tetrahedra and three triangles serves as a structural element of boron–oxygen radicals. The degree of condensation of single structural elements in this row as crystallized water is lost regularly increases from isolated complexes to frameworks. For example, the one-dimensional band-shaped structure characterizes the boron–oxygen radical in the aristarainite radical

$$Na_2Mg[B_6O_8(OH)_4]_2 \cdot 4H_2O,$$

and layered anion boron–oxygen structures are the basis for the

$$Sr[B_6O_9(OH)_2] \cdot 3H_2O$$

tunellite crystal structures and for those of

$$Ca[B_6O_9(OH)_2] \cdot 3H_2O \text{ nobleite [2].}$$

According to available information, the $[B_6O_{10}]^{2-}_{\infty\infty\infty}$ boron–oxygen framework in mineral structures and in synthetic phases was not found before and is described by us for the first time in the structure of the $Na_3(No_3)[B_6O_{10}]$ microporous low-temperature compound.

Broad eight-, nine-, and ten-term windows formed by boron triangles and tetrahedra open the input to channels of the $[B_6O_{10}]^{2-}_{\infty\infty\infty}$ microporous zeolite-like framework (Figs. 2–4). The boron–oxygen framework is maximally open in the direction of the unit-cell *b* axis. Two types of channels are aligned along this direction and are restricted by eight- and ten-term rings. (Fig. 3). The maximum size of the most broad ten-term windows equals 9.2 Å. In natural conditions, zeolite-like borates are found in marine evaporite deposits [2]. These are dimorphic pringleite and ruitenbergite minerals being described by the rather complicated formula

$$Ca_9[B_{20}O_{28}(OH)_{18}][B_6O_6(OH)_6]Cl_4(H_2O)_{13},$$

and the penobsquisite

$$Ca_2Fe[B_9O_{13}(OH)_6]Cl(H_2O)_4$$

Ca, Fe borate.

Among natural borates, minerals containing additional complex anions, namely, carbonate, aluminosilicate, arsenate, sulfate, and phosphate anions are known. These are

$Ca_4Mn_3O_3(CO_3)[BO_3]_3$ gaudefroyite,

$Ca_2Mg(CO_3)_2[B(OH)_4]_2 \cdot 4H_2O$ carboborite,

$Ca_4Mg(CO_3)_2[B_4O_6(OH)_6]$ borcarite,

$Ca_3Mg(CO_3)[BO_3]_2 \cdot 0.36H_2O$ sakhaite,

$Ca_{12}Mg_4(CO_3)_4[AlSi_4(O,OH)_{16}][BO_3]_4 \cdot 0.5(H_2O,Cl)$, harkerite,

$Ca_4Mg[AsB_6O_{11}(OH)_6]_2 \cdot 14H_2O$ teruggite [14],

$Mn_3(PO_4)[B(OH)_4](OH)_2$ simonite,

and $Mg_3(SO)_4[B(OH)_4]_2(OH)_2$ sulfoborite [15].

A large number of borates with additional complex acid anion groupings were obtained recently under laboratory conditions. However, no borate–nitrates have yet been synthesized among them. The crystals described in the present study are the first borates known to us whose structure is also formed by triangular nitrate groups.

ACKNOWLEDGMENTS

The authors are grateful to E.V. Guseva for performing X-ray spectral analysis of samples.

This work was supported by the Russian Foundation for Basic Research, project numbers 00-05-64312 and 00-15-98582.

REFERENCES

1. A. E. Fersman, *Geochemistry* (Goskhimtekhizdat, Leningrad, 1939), Vol. 4.
2. J. D. Grice, P. C. Burns, and F. C. Hawthorne, Can. Mineral. **37**, 731 (1999).
3. H. Effenberger, Acta Crystallogr. B **38**, 82 (1982).
4. H. König and R. Hopper, Z. Anorg. Allg. Chem. **439**, 71 (1978).
5. T. Sasaki, I. Mori, I. Kuroda, *et al.*, Acta Crystallogr. C **51**, 2222 (1995).
6. G. M. Sheldrick, *SHELXS-97: Program for the Solution of Crystal Structures* (Univ. of Göttingen, Göttingen, 1997).
7. G. M. Sheldrick, *SHELXS-97: Program for the Refinement of Crystal Structures from Diffraction Data* (Univ. of Göttingen, Göttingen, 1997).
8. *International Tables of Crystallography*, Ed. by T. Hahn (Kluwer, Dordrecht, 1995), Vol. A.
9. V. S. Urusov and I. P. Orlov, Kristallografiya **44**, 736 (1999) [Crystallogr. Rep. **44**, 686 (1999)].
10. J. R. Clark, Science **141**, 1178 (1963).
11. N. V. Belov, O. V. Yakubovich, Yu. K. Egorov-Tismenko, and M. A. Simonov, Mineral. Zh., No. 6, 38 (1981).
12. H. Strunz, Eur. J. Mineral. **9**, 225 (1977).
13. F. Hanic, O. Lindqwist, I. Nyborg, and A. Zedler, Collect. Czech. Chem. Commun. **36**, 3678 (1971).
14. O. V. Yakubovich, N. A. Yamnova, M. A. Simonov, and N. V. Belov, Mineral. Zh., No. 3, 32 (1983).
15. O. V. Yakubovich, M. A. Simonov, and N. V. Belov, in *Problems of Crystal Chemistry and Genesis of Minerals* (Nauka, Leningrad, 1983), pp. 51–56.

Translated by G. Merzon

Doklady Physics, Vol. 47, No. 11, 2002, pp. 798–800. Translated from Doklady Akademii Nauk, Vol. 387, No. 2, 2002, pp. 178–180.

PHYSICS

Nonlinear Electrodynamic Effect of Frequency Doubling in the Field of a Magnetic Dipole

P. A. Vshivtseva, V. I. Denisov, and I. P. Denisova

Presented by Academician V.A. Magnitskiĭ May 17, 2002

Received May 17, 2002

In modern theoretical models, electrodynamics in vacuum is known to be treated as a nonlinear theory. The corresponding Lagrangian in the approximation of a weak electromagnetic field can be written out in the following parametric form:

$$L = \frac{1}{8\pi}\{[\mathbf{E}^2 - \mathbf{B}^2] + \xi[\eta_1(\mathbf{E}^2 - \mathbf{B}^2)^2 + 4\eta_2(\mathbf{BE})^2]\}, \quad (1)$$

where $\xi = \frac{1}{B_q^2} = 0.5 \times 10^{-27}$ G^{-2} and the parameters η_1 and η_2 depend on a particular theoretical model.

For example, according to predictions of quantum electrodynamics, $\eta_1 = \frac{\alpha}{45\pi} = 5.1 \times 10^{-5}$ and $\eta_2 = \frac{7\alpha}{180\pi} = 9.0 \times 10^{-5}$, where α is the fine-structure constant [2]. The effective Lagrangian of an electromagnetic field in supersymmetric models coincides with that of the Born–Infeld electrodynamics [3]. As a result, these parameters turn out to be identical, $\eta_1 = \eta_2 = \frac{a^2 B_q^2}{4}$, and depend on a constant a^2 for which only the lower bound is known: $a^2 > 1.2 \times 10^{-32}$ G^{-2}.

The electromagnetic equations following from Lagrangian (1) are similar to the equations of macroscopic electrodynamics

$$\mathrm{rot}\mathbf{H} = \frac{1}{c}\frac{\partial \mathbf{D}}{\partial t}, \quad \mathrm{div}\mathbf{D} = 0,$$
$$\mathrm{rot}\mathbf{E} = -\frac{1}{c}\frac{\partial \mathbf{B}}{\partial t}, \quad \mathrm{div}\mathbf{B} = 0 \quad (2)$$

with the specific constitutive equations

$$\mathbf{D} = 4\pi\frac{\partial L}{\partial \mathbf{E}} = \mathbf{E} + 2\xi\{\eta_1(\mathbf{E}^2 - \mathbf{B}^2)\mathbf{E} + 2\eta_2(\mathbf{BE})\mathbf{B}\},$$
$$\mathbf{H} = -4\pi\frac{\partial L}{\partial \mathbf{B}} = \mathbf{B} + 2\xi\{\eta_1(\mathbf{E}^2 - \mathbf{B}^2)\mathbf{B} - 2\eta_2(\mathbf{BE})\mathbf{E}\}. \quad (3)$$

Nonlinear electrodynamic effects in vacuum for electromagnetic fields attainable in laboratory conditions are extremely small. Therefore, their observation was impossible for a long time. The first experiment, performed only recently [4], has shown that electrodynamics in vacuum is actually a nonlinear theory. At present, on account of the further development of experimental technique, the possibility arises to observe other nonlinear electrodynamic effects in laboratory conditions or as a result of astrophysical investigations [5–9].

The frequency-doubling effect for an electromagnetic signal propagating in the strong magnetic-dipole field of a neutron star is one of such effects. In terms of quantum theory, this process corresponds to the fusion of photons in the magnetic-dipole field [10]. Below, we estimate the efficiency of such a process.

We consider a neutron star with the radius R, which has the magnetic-dipole field

$$\mathbf{B}_0 = \frac{3(\mathbf{mn})\mathbf{n} - \mathbf{m}}{r^3}, \quad (4)$$

where $\mathbf{m}$ is the magnetic dipole moment and $\mathbf{n} = \frac{\mathbf{r}}{r}$.

We assume that a spherical electromagnetic wave with the frequency ω is radiated from the surface of the star. In the simplest case, the vectors $\mathbf{B}_1$ and $\mathbf{E}_1$ for this wave take the form

$$\mathbf{B}_1 = -[\mathbf{na}_1]\sqrt{\frac{\pi k}{2r}}H^{(1)}_{3/2}(kr)e^{-i\omega t},$$
$$\mathbf{E}_1 = \frac{i}{3}\sqrt{\frac{\pi k}{2r}}\{[2H^{(1)}_{1/2}(kr) - H^{(1)}_{5/2}(kr)]\mathbf{a}_1 + 3(\mathbf{na}_1)\mathbf{n}H^{(1)}_{5/2}(kr)\}e^{-i\omega t}, \quad (5)$$

Moscow State University,
Vorob'evy gory, Moscow, 119899 Russia

1028-3358/02/4711-0798$22.00

where $k = \frac{\omega}{c}$ and the vector $\mathbf{a}_1$ specifies the polarization and orientation of the directivity pattern for radiation in space.

In the wave zone ($kr \gg 1$), the time-averaged angular distribution of the radiation at the frequency ω takes the form

$$\frac{\overline{dI}}{d\Omega}(\omega) = \frac{c[\mathbf{n}\mathbf{a}_1]^2}{8\pi}.$$

Integrating this expression over angles, we find the total radiation intensity of the neutron star at the frequency ω:

$$\bar{I}(\omega) = \frac{c\mathbf{a}_1^2}{3}.$$

In such a formulation of the problem, the vectors $\mathbf{D}$ and $\mathbf{H}$ entering into Eqs. (2) and (3) have terms depending on frequencies multiple to the frequency ω. Therefore, after passing electromagnetic wave (5) through magnetic field (4), a series of secondary waves originates as a result of the wave–field interaction. We now find the vectors $\mathbf{B}_2$ and $\mathbf{E}_2$ for an electromagnetic wave with the frequency 2ω.

Because the magnetospheres of neutron stars are basically transparent only for X-rays and gamma radiation, we assume that $kR \gg 1$. Substituting expressions $\mathbf{B} = \mathbf{B}_0 + \mathrm{Re}\mathbf{B}_1 + \mathbf{B}_2$ and $\mathbf{E} = \mathrm{Re}\mathbf{E}_1 + \mathbf{E}_2$ into Eqs. (2) and (3) and taking into account that $|\mathbf{B}_2| \ll |\mathbf{B}_1|$ and $|\mathbf{E}_2| \ll |\mathbf{E}_1|$, we arrive at the following system of equations for the vectors $\mathbf{B}_2$ and $\mathbf{E}_2$:

$$\begin{aligned} \mathrm{rot}\mathbf{H}_2 &= \frac{1}{c}\frac{\partial \mathbf{D}_2}{\partial t}, \quad \mathrm{div}\mathbf{D}_2 = 0, \\ \mathrm{rot}\mathbf{E}_2 &= -\frac{1}{c}\frac{\partial \mathbf{B}_2}{\partial t}, \quad \mathrm{div}\mathbf{B}_2 = 0. \end{aligned} \tag{6}$$

It is convenient to present the asymptotically dominant terms of the vectors $\mathbf{D}_2$ and $\mathbf{H}_2$ in the form

$$\begin{aligned} \mathbf{D}_2 &= \mathbf{E}_2 - \xi\{\eta_1[(\mathbf{B}_0\mathbf{B}_1)\mathbf{E}_1 + (\mathbf{B}_0\mathbf{B}_1^*)\mathbf{E}_1^*] \\ &\quad - \eta_2[(\mathbf{B}_0\mathbf{E}_1)\mathbf{B}_1 + (\mathbf{B}_0\mathbf{E}_1^*)\mathbf{B}_1^*]\}, \\ \mathbf{H}_2 &= \mathbf{B}_2 - \xi\{\eta_1[(\mathbf{B}_0\mathbf{B}_1)\mathbf{B}_1 + (\mathbf{B}_0\mathbf{B}_1^*)\mathbf{B}_1^*] \\ &\quad + \eta_2[(\mathbf{B}_0\mathbf{E}_1)\mathbf{E}_1 + (\mathbf{B}_0\mathbf{E}_1^*)\mathbf{E}_1^*]\}. \end{aligned}$$

We write out the retarded solution to Eqs. (6) for $r \gg R$ as

$$\mathbf{E}_2 = -[\mathbf{n}\mathbf{B}_2], \tag{7}$$

$$\begin{aligned} \mathbf{B}_2 &= \frac{\xi\cos 2(\omega t - kr - 2kR)}{rR^4}\{\eta_1(\mathbf{n}[\mathbf{m}\mathbf{a}_1])[\mathbf{n}\mathbf{a}_1] \\ &\quad + \eta_2\{(\mathbf{m}\mathbf{a}_1) - (\mathbf{n}\mathbf{a}_1)(\mathbf{n}\mathbf{m})\}[\mathbf{n}[\mathbf{n}\mathbf{a}_1]]\}. \end{aligned}$$

Using Eqs. (7), we easily find the time-averaged angular distribution of the radiation at the frequency 2ω, which results from the nonlinear interaction of electromagnetic wave (5) with magnetic-dipole field (4):

$$\begin{aligned} \frac{\overline{dI}}{d\Omega}(2\omega) &= \frac{c\xi^2[\mathbf{n}\mathbf{a}_1]^2}{8\pi R^8} \\ &\quad + \{\eta_1^2(\mathbf{n}[\mathbf{m}\mathbf{a}_1])^2 + \eta_2^2\{(\mathbf{m}\mathbf{a}_1) - (\mathbf{n}\mathbf{a}_1)(\mathbf{n}\mathbf{m})\}^2\}. \end{aligned} \tag{8}$$

Let the neutron star rotate with the frequency Ω about an axis not directed along the magnetic dipole moment $\mathbf{m}$. If we denote this axis the z-axis, then

$$\mathbf{m} = |\mathbf{m}|\{\sin\beta\cos\Omega t, \sin\beta\sin\Omega t, \cos\beta\},$$

where β is the angle between the rotation axis and the vector $\mathbf{m}$.

Substituting this expression into Eq. (8), we easily conclude that a certain effect of the amplitude modulation of the radiation recorded by an observer arises in this case. The modulation frequency corresponds to the star's rotation frequency, while the modulation depth depends on the angle between the rotation axis and the magnetic-dipole moment.

Integrating expression (8) over angles, we find the total intensity of the electromagnetic radiation at the frequency 2ω:

$$\begin{aligned} \bar{I}(2\omega) &= \frac{2c\xi^2\mathbf{a}_1^2}{105R^8} \\ &\quad \times \{7\eta_1^2[\mathbf{m}\mathbf{a}_1]^2 + \eta_2^2[\mathbf{m}^2\mathbf{a}_1^2 + 11(\mathbf{m}\mathbf{a}_1)^2]\}. \end{aligned}$$

We now determine a factor for the electromagnetic-wave energy conversion from the frequency ω to the doubled frequency 2ω:

$$\begin{aligned} k &= \frac{\overline{dI}}{d\Omega}(2\omega)\Big/\frac{\overline{dI}}{d\Omega}(\omega) \\ &= \frac{\xi^2}{R^8}\{\eta_1^2(\mathbf{n}[\mathbf{m}\mathbf{a}_1])^2 + \eta_2^2\{(\mathbf{m}\mathbf{a}_1) - (\mathbf{n}\mathbf{a}_1)(\mathbf{n}\mathbf{m})\}^2\}. \end{aligned} \tag{9}$$

This factor is determined by properties of both the initial wave and the magnetic-dipole field (4), which serves as an energy converter.

Before, we assumed that a source radiates electromagnetic waves with directivity pattern (8). However, X-rays and gamma radiation from magnetic neutron stars are caused by the accretion of matter and the acceleration of charged particles. Therefore, the directivity pattern for the radiation by a neutron star having a strong magnetic field is very narrow.

As is shown by detailed analysis, by virtue of this fact, the factor of the nonlinear electrodynamic energy conversion in a magnetic-dipole field could be greater than that given by expression (9) by four to five orders

of magnitude. In the problem under consideration, the following estimates are valid:

$$\mathbf{a}_1^2 \sim \frac{\bar{I}(\omega)}{c}, \quad \frac{\mathbf{m}^2}{R^6} \sim \mathbf{B}_0^2(R).$$

Hence,

$$k \sim 10^5 \eta_{1,2}^2 \xi^2 \mathbf{B}_0^2(R) \frac{\bar{I}(\omega)}{cR^2}.$$

Using this expression, we now estimate the efficiency of the nonlinear electrodynamic doubling of frequency in various theoretical models. We assume that the radius of a magnetic neutron star is 3 km and the intensities of its X rays and gamma radiation coincide with the intensity of giant flares: $\bar{I}(\omega) \sim 10^{40}$ erg s^{-1}.

According to quantum electrodynamics, expansion (1) is valid only if $\xi \mathbf{B}_1^2(R) < 1$ and $\xi \mathbf{B}_0^2(R) < 1$. Therefore, the results obtained above are applicable to a neutron star provided that the value of $|\mathbf{B}_0(R)|$ at its surface does not exceed $B_q = 4.41 \times 10^{13}$ G. In this case, $\eta_{1,2} \sim 10^{-4}$; therefore, we have $k \sim 10^{-11}$.

The expansion of Lagrangian (1) can be used in the Born–Infeld nonlinear electrodynamics in the case of $|\mathbf{B}_0(R)|$ being less than 10^{16} G. Therefore, the results obtained above can be applied to recently discovered magnetars, for which $|\mathbf{B}_0(R)| \sim 10^{16}$ G. In the case of a sufficiently powerful flare of X-rays or gamma radiation, the conversion factor could be as large as $k \sim 10^{-7}$.

Thus, under favorable conditions, electromagnetic radiation at the frequency 2ω originating in the magnetic field of a neutron star could attain an intensity quite measurable in the circumterrestrial space.

ACKNOWLEDGMENTS

This work was supported by the Russian Foundation for Basic Research, project no. 02-02-16598.

REFERENCES

1. V. I. Denisov and I. P. Denisova, Opt. Spektrosk. **90**, 329 (2001).
2. W. Heisenberg and H. Euler, Z. Phys. **26**, 714 (1936).
3. M. Born and L. Infeld, Proc. R. Soc. London, Ser. A **144**, 425 (1934).
4. D. L. Burke, R. C. Feld, G. Horton-Smith, *et al.*, Phys. Rev. Lett. **79**, 1626 (1997).
5. E. B. Aleksandrov, A. A. Ansel'm, and A. N. Moskalev, Zh. Éksp. Teor. Fiz. **89**, 1181 (1985) [Sov. Phys. JETP **62**, 680 (1985)].
6. N. N. Rozanov, Zh. Éksp. Teor. Fiz. **103**, 1996 (1993) [JETP **76**, 991 (1993)].
7. D. Bakalov, F. Brandi, G. Cantatore, *et al.*, Quant. Semiclass. Opt. **10** (1), 239 (1998).
8. V. I. Denisov, Phys. Rev. D **61**, 036004 (2000).
9. V. I. Denisov and I. P. Denisova, Teor. Mat. Fiz. **129**, 131 (2001).
10. I. M. Ternov, V. R. Khalilov, and V. N. Rodionov, *Interaction of Charged Particles with a Strong Electromagnetic Field* (Mosk. Gos. Univ., Moscow, 1982).

Translated by V. Chechin

Doklady Physics, Vol. 47, No. 11, 2002, pp. 801–803. Translated from Doklady Akademii Nauk, Vol. 387, No. 2, 2002, pp. 181–183.

PHYSICS

Dynamics of the Interface Displacement in the Case of Oriented Crystallization

A. P. Gus'kov

Presented by Academician Yu.A. Osip'yan July 15, 2002

Received July 16, 2002

Stability of a phase interface under oriented crystallization was considered in the oriented-crystallization model proposed in [1, 2]. In contrast to other models, temperature perturbations and concentration perturbations are treated in this model as an initial perturbation. These perturbations lead to displacement-velocity disturbances at the interface, an effect which is associated with kinetic overcooling. In [3, 4], dependences of the eutectic-structure period on the displacement velocity of the phase interface were found from solutions inherent in the model. These dependences closely coincide with available experimental results. In the present paper, we argue that the model of [1, 2] has solutions in the form of plane interfaces for which both temperature perturbations and concentration perturbations take place. Such crystallization regimes are consistent with experimental results for the component-concentration distribution in the liquid phase under crystallization of eutectics. We also argue that the model has solutions describing cellular interfaces. This result is a consequence of the fact that, in the mathematical model of oriented crystallization [1, 2], interfaces are considered as curved surfaces (in contrast to other models in which boundary conditions are imposed on the plane boundary), and, moreover, the kinetic overcooling is taken into account in the general form. It should be pointed out that for describing cellular interfaces, models were developed in which the surface-tension anisotropy was assumed as a basic cause of the specific shape of these interfaces [5] or a modification of Hunt–Jackson theory was employed [6].

Without repeating the description of the model developed in [1, 2], we list the parameters needed for subsequent consideration: $T(\bar{y}, \bar{z}, \tau)$, $\bar{T}(\bar{y}, \bar{z}, \tau)$, $C(\bar{y}, \bar{z}, \tau)$, and $\bar{C}(\bar{y}, \bar{z}, \tau)$ are the temperatures and component concentrations in the liquid phase, respectively, in curvilinear and laboratory (symbols with bars) coordinate systems; V_s is the steady-state displacement velocity of the interface; K is the wave number; and ω is the frequency of time pulsations.

We now allow for the effect of the surface tension in the model under consideration. In the curvilinear coordinate system proposed in [1, 2], the kinetic overcooling (i.e., the difference between the interface temperature and phase transition temperature) is given by the relation

$$\Delta T_k = 1 + m(C(0, y, \tau) - 1) + \Gamma\kappa(T(0, y, \tau), C(0, y, \tau)) - T(0, y, \tau).$$

Here, κ is the curvature of the phase interface, $\Gamma = \alpha\Gamma_d$, Γ_d is the surface-tension coefficient, $\alpha = 10^2$ m^{-1}, and m is the slope of the liquidus line. In this case, the expansion of the phase-interface displacement velocity $V \approx V_S + V_m$ into the Taylor series up to the terms linear in small perturbations of temperature T_m and concentration C_m, respectively, has the form (see [1, 2])

$$V \approx V_S + \Lambda(-T_m + mC_m + \Gamma\kappa), \quad \Lambda = \frac{\partial V}{\partial \Delta T_k}. \quad (1)$$

We seek V_m as a linear combination of the perturbations:

$$V_m = \theta f_{T0} + \gamma f_{C0},$$

where

$$f_{T0} = T_m(0)\exp(Ky + \omega\tau)$$

and

$$f_{C0} = C_m(0)\exp(Ky + \omega\tau).$$

Here, θ and γ are unknown quantities to be found from kinetic equation (1) and the expression for the curvature of the interface in the linear approximation:

$$\kappa = K^2 f,$$

Institute of Solid State Physics,
Russian Academy of Sciences,
Chernogolovka, Moscow oblast, 142432 Russia

1028-3358/02/4711-0801$22.00

where f denotes the linear term in the expansion [1, 2]

$$F(0, y, t) = \int (V_S + \theta f_{T0} + \gamma f_{C0})dt$$

$$= V_s t + \frac{\theta f_{T0} + \gamma f_{C0}}{\omega} = F_s + f.$$

The solution to these equations is

$$\theta = \Lambda \frac{\omega}{\Lambda \Gamma K^2 - \omega}, \quad \gamma = -m\theta.$$

We now rewrite the expressions for the temperature and concentration in rectangular coordinates in terms of solutions to the linearized problem in curvilinear coordinates:

$$\begin{aligned} \bar{T}(\bar{z}, \bar{y}, \bar{\tau}) &\approx T_s(\bar{z} - \bar{F}(\bar{z}_b, \bar{y}, \bar{\tau})) \\ &+ T_m(\bar{z} - \bar{F}(\bar{z}_b, \bar{y}, \bar{\tau}))\exp(K\bar{y} + \omega\bar{\tau}), \\ \bar{C}(\bar{z}, \bar{y}, \bar{\tau}) &\approx C_s(\bar{z} - \bar{F}(\bar{z}_b, \bar{y}, \bar{\tau})) \\ &+ C_m(\bar{z} - \bar{F}(\bar{z}_b, \bar{y}, \bar{\tau}))\exp(K\bar{y} + \omega\bar{\tau}). \end{aligned} \tag{2}$$

These expressions are inconvenient for analysis, because they include the unknown coordinate $\bar{z}_b$ of the phase interface. However, we can express $\bar{z}_b$ in terms of a small-perturbation amplitude. To do this, we expand the argument of these expressions in a power series for a small perturbation. The summation of the infinite series leads to the relationship

$$\bar{z} - \bar{F}(\bar{z}_b, \bar{y}, \bar{\tau}) = \bar{z} - \bar{F}_S(\bar{\tau}) - f(0, y, \tau)$$

$$= \hat{z} - \frac{1}{1 + \xi}\frac{V_{mb}}{\omega}\exp(K\bar{y} + \omega\bar{\tau}),$$

where

$$\hat{z} = \bar{z} - \bar{F}_S(\bar{\tau}), \quad \xi = \left.\frac{\partial f(\hat{z}, \bar{y}, \bar{\tau})}{\partial \hat{z}}\right|_{\hat{z} = \hat{z}_b},$$

$$V_{mb} = \theta T_m(\hat{z}_b) + \gamma C_m(\hat{z}_b).$$

Substituting these expressions into Eq. (2), we write out the quantities under consideration in the form

$$\begin{aligned} \bar{T}(\hat{z}_b, \bar{y}, \bar{\tau}) &= T_s(\hat{z}_b) + T_m(\hat{z}_b)\exp(K\bar{y} + \omega\bar{\tau}) \\ &- \frac{G_T E_m \exp(K\bar{y} + \omega\bar{\tau})}{\Gamma K^2 - \frac{\omega}{\Lambda} + G_m \exp(K\bar{y} + \omega\bar{\tau})}, \end{aligned} \tag{3}$$

$$\begin{aligned} \bar{C}(\hat{z}_b, \bar{y}, \bar{\tau}) &= C_s(\hat{z}_b) + C_m(\hat{z}_b)\exp(K\bar{y} + \omega\bar{\tau}) \\ &- \frac{G_C E_m \exp(K\bar{y} + \omega\bar{\tau})}{\Gamma K^2 - \frac{\omega}{\Lambda} + G_m \exp(K\bar{y} + \omega\bar{\tau})}. \end{aligned} \tag{4}$$

The displacement velocity and coordinate of the interface are given by the relations

$$\begin{aligned} \bar{V}(\hat{z}_b, \bar{y}, \bar{\tau}) &= \frac{E_m \exp(K\bar{y} + \omega\bar{\tau})\omega}{\Gamma K^2 - \frac{\omega}{\Lambda} + G_m \exp(K\bar{y} + \omega\bar{\tau})}, \\ \hat{z}_b(\bar{y}, \bar{\tau}) &= \frac{E_m \exp(K\bar{y} + \omega\bar{\tau})}{\Gamma K^2 - \frac{\omega}{\Lambda} + G_m \exp(K\bar{y} + \omega\bar{\tau})}. \end{aligned} \tag{5}$$

The latter equation determines the coordinate of the interface, the remaining parameters being known. Here, we introduce the following notation:

$$E_m = T_m(\hat{z}_b) - mC_m(\hat{z}_b), \quad E_S = T_S(\hat{z}_b) - mC_S(\hat{z}_b),$$

$$G_m = \left.\frac{\partial T_m(\hat{z})}{\partial \hat{z}}\right|_{\hat{z} = \hat{z}_b} - m\left.\frac{\partial C_m(\hat{z})}{\partial \hat{z}}\right|_{\hat{z} = \hat{z}_b},$$

$$G_T = \left.\frac{\partial T_S(\hat{z})}{\partial \hat{z}}\right|_{\hat{z} = \hat{z}_b} + \left.\frac{\partial T_m(\hat{z})}{\partial \hat{z}}\right|_{\hat{z} = \hat{z}_b}\exp(K\bar{y} + \omega\bar{\tau}),$$

$$G_C = \left.\frac{\partial C_S(\hat{z})}{\partial \hat{z}}\right|_{\hat{z} = \hat{z}_b} + \left.\frac{\partial C_m(\hat{z})}{\partial \hat{z}}\right|_{\hat{z} = \hat{z}_b}\exp(K\bar{y} + \omega\bar{\tau}).$$

As follows from Eq. (5), the displacement velocity and coordinate of the interface tend to zero as $K \longrightarrow \infty$. The result obtained differs from the classical one, according to which the surface tension suppresses high-frequency perturbations. This turns out to be not true. Even though the surface tension suppresses spatial perturbations of the interface and perturbations of its displacement velocity, the temperature perturbations and concentration perturbations given by Eqs. (3) and (4) survive. This is a fundamental result, because it elucidates the origin of microinhomogeneities under crystallization.

If the surface tension is at a resonance point, i.e., if

$$\Gamma K^2 - \frac{\omega}{\Lambda} = 0,$$

the second harmonics disappear in all of the expressions. In this case, the equations for the coordinate and displacement velocity of the interface take the form

$$\hat{z}_b(\bar{y}, \bar{\tau}) = \frac{E_m}{G_m}, \quad \bar{V}(\hat{z}_b, \bar{y}, \bar{\tau}) = \frac{E_m \omega}{G_m}$$

(i.e., they are independent of $\bar{y}$ and τ), and the interface grows as a single whole preserving its plane shape. In the general case, the displacement velocity of the interface differs from the velocity of its steady motion. The case of the surface-tension resonance under consideration is degenerate. Therefore, in order to analyze it, we must solve the problem in the second approximation.

The case of $E_m = 0$ is of interest. From the physical standpoint, it corresponds to a situation when the point determining a state of the system in the coordinates (T_e, C) moves along the liquidus line. In this case, there

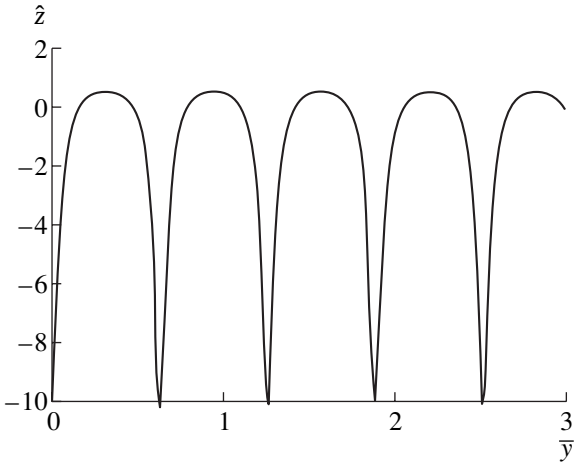

Shape of a phase interface in rectangular coordinates for the case of boundary conditions imposed on the curvilinear interface. Here, $E_m = 1$, $K_2 = 10$, $\Gamma K_2^2 = 1$, and $G_m = 0.9$.

exist perturbations of the temperature and concentration in the system; however, perturbations of both the coordinates and displacement velocity of the interface are absent. With regard to the results of [3, 4], this suggests that eutectic crystallization occurs in this regime.

As is well known from numerous experiments, the cellular crystallization front has a specific shape with a complex spectrum. Therefore, the spectrum of temperature and concentration perturbations is also inferred to be complex. However, the shape of the cellular front of crystallization turns out to be determined only by a single harmonic of temperature and concentration perturbations given in curvilinear coordinates. Its complex shape is determined by the fact that the displacement velocity of the interface depends on the kinetic overcooling. Rewriting expression (5) for the interface coordinate in terms of real-valued functions, we arrive at the relationship

$$\hat{z}_{breal}(\bar{y}, \bar{\tau}) = \frac{E_m \cos(K_2 \bar{y})}{-\Gamma K_2^2 + G_m \cos(K_2 \bar{y})},$$

in which we assume that $\omega = 0$. The shape of the interface for certain values of parameters is shown in the figure. The obtained shape of the interface coincides with the known shape of a cellular crystallization front.

Thus, we have derived analytical expressions for the shape of a phase interface and for the distributions of both temperature and component concentration at the phase interface under oriented crystallization. We have shown the existence of crystallization regimes for which temperature perturbations and concentration perturbations take place on a planar phase interface. The solutions obtained elucidate the origination of inhomogeneities of an arbitrarily small size in the solid phase. We have also shown that the solutions found determine the shape of the interface, which coincides with that observed under cellular crystallization.

REFERENCES

1. A. P. Gus'kov, Dokl. Akad. Nauk **366**, 468 (1999) [Dokl. Phys. **44**, 330 (1999)].
2. A. P. Gus'kov, Izv. Ross. Akad. Nauk, Ser. Fiz. **63**, 1772 (1999).
3. A. Gus'kov, Comput. Mater. Sci. **17**, 555 (2000).
4. A. P. Gus'kov, Pis'ma Zh. Tekh. Fiz. **27** (11), 86 (2001) [Tech. Phys. Lett. **27**, 480 (2001)].
5. S. Akamatsu, G. Faivre, and T. Ihle, Phys. Rev. E **51**, 4751 (1995).
6. M. D. Nave, A. K. Dahle, and D. H. StJohn, Acta Mater. **50**, 2837 (2002).

Translated by V. Chechin

Doklady Physics, Vol. 47, No. 11, 2002, pp. 804–807. Translated from Doklady Akademii Nauk, Vol. 387, No. 2, 2002, pp. 184–187.

PHYSICS

Waveguides with a Complicated Cross-Sectional Shape

V. I. Krivenkov

Presented by Academician E.M. Dianov July 10, 2002

Received July 18, 2002

All presently known methods for calculating the dispersion characteristics of waveguides with a noncircular cross-sectional shape possess a number of noticeable disadvantages. At the same time, special exact calculation methods, e.g., the method of particular domains in the case of elliptic waveguides, have, as a rule, a rather narrow range of application [1, 2]. Universal methods, for example, the finite-difference method, the finite-element method [3], the shear-formula method [4], etc., cannot provide a reasonably high accuracy.

In this paper, a rigorous method for solving the problem on natural waves in a waveguide with an arbitrary cross-sectional shape is presented. For guided modes of this waveguide, exact expressions concerning electromagnetic-field components, dispersion equations, and the equation of critical wavelengths are obtained.

As a generalized model of a waveguide with a complicated cross section, we consider a dielectric structure consisting of both a core that has the form of an infinite cylinder with radius a, which is aligned along a certain axis z, and an infinitely thick shell c with a constant permittivity ε_{00}. The permittivity of the core in a cylindrical coordinate system r, φ, z depends only on the transverse coordinates r and φ.

We write the permittivity $\varepsilon(r, \varphi)$ [and also $\varepsilon^{-1}(r, \varphi)$] of this waveguide in the form

$$\varepsilon^i(r, \varphi) = \begin{cases} \sum_{n=0}^{\infty}\sum_{\nu=0}^{1} \varepsilon^i_{2n-\nu}(r)\cos\left(n\varphi - \nu\frac{\pi}{2}\right), & 0 \le r < a \\ \varepsilon^i_{00}, & a \le r < \infty, \end{cases}$$

$$\varepsilon_{00} < \max\varepsilon(r, \varphi), \quad \varepsilon^i_n(0) = 0,$$
$$n = 1, 2, \ldots, \quad i = \pm 1.$$

Moscow State Academy of Instrumentation and Informatics, ul. Stromynka 20, Moscow, 107846 Russia

Here,

$$\varepsilon^i_{2n-\nu}(r) = \frac{2^{-\delta(2n-\nu)}}{\pi}\int_0^{2\pi} \varepsilon^i(r, \varphi)\cos\left(n\varphi - \nu\frac{\pi}{2}\right)d\varphi,$$

$$\delta(x \ne 0) = 0, \quad \delta(0) = 1,$$
$$i = \pm 1, \quad \nu = 0, 1, \quad n = 0, 1, \ldots$$

are, in the general case, piecewise-continuous functions. After the determination of the discontinuity points $r_1, r_2, \ldots, r_{N-1}$, without loss of generality, we can represent these functions in the form [5]

$$\varepsilon^i_n(r) = \sum_{k=0}^{\infty} \varepsilon^{il}_{nk}\left(\frac{r - r_{l-1}}{r_l - r_{l-1}}\right)^k,$$

$$r_{l-1} \le r < r_l, \quad l = 1, 2, \ldots, N,$$

$$r_0 = 0, \quad r_N = a, \quad \varepsilon^{i1}_{n0} = 0,$$

$$n = 1, 2, \ldots, \quad i = \pm 1.$$

Furthermore, we assume that components of the electric-field-strength vector $\mathbf{E} = (E_r, E_\varphi, E_z)$ and the magnetic-field-strength vector $\mathbf{H} = (H_r, H_\varphi, H_z)$ for the guided mode of the waveguide under consideration depend on time t and the longitudinal coordinate z. The dependence has the form $\exp[j(\omega t - \beta z)]$ (below, this dependence is omitted). Here, ω and β are the circular frequency and the constant for the longitudinal propagation of the mode. Using Maxwell equations for a nonmagnetic dielectric medium, we arrive at the following system of equations:

$$r\frac{\partial \mathbf{e}}{\partial r} = \mathbf{A}(r, \varphi)\mathbf{h},$$

$$r\frac{\partial \mathbf{h}}{\partial r} = \mathbf{B}(r, \varphi)\mathbf{e},$$

where

$$\mathbf{e} = \begin{pmatrix} j\sqrt{\varepsilon_0}E_z \\ k_0 r\sqrt{\mu_0}H_r \end{pmatrix}, \quad \mathbf{h} = \sqrt{\mu_0}\begin{pmatrix} jH_z \\ k_0 r H_\varphi \end{pmatrix},$$

1028-3358/02/4711-0804$22.00

$$\mathbf{A}(r, \varphi) = \begin{pmatrix} -\dfrac{\gamma}{\varepsilon(r, \varphi)}\dfrac{\partial}{\partial\varphi} & \dfrac{\gamma^2 - \varepsilon(r, \varphi)}{\varepsilon(r, \varphi)} \\ k_0^2 r^2 \gamma & -\dfrac{\partial}{\partial\varphi} \end{pmatrix},$$

$$\mathbf{B}(r, \varphi) = \begin{pmatrix} \dfrac{\varepsilon(r, \varphi)}{\gamma}\dfrac{\partial}{\partial\varphi} & \dfrac{\gamma^2 - \varepsilon(r, \varphi)}{\gamma} \\ k_0^2 r^2 \varepsilon(r, \varphi) & \dfrac{\partial}{\partial\varphi} \end{pmatrix},$$

and $\gamma = \dfrac{\beta}{k_0}$, $k_0 = \omega\sqrt{\varepsilon_0\mu_0}$, and ε_0 and μ_0 are electric and magnetic constants.

Using the substitution

$$\mathbf{e}(r, \varphi) = \sum_{m=0}^{\infty}\sum_{\mu=0}^{1} \mathbf{S}_m^{\mu}(\varphi)\mathbf{e}_m^{\mu}(r),$$

$$\mathbf{h}(r, \varphi) = \sum_{m=0}^{\infty}\sum_{\mu=0}^{1} (-1)^{\mu}\mathbf{S}_m^{1-\mu}(\varphi)\mathbf{h}_m^{\mu}(r),$$

where

$$\mathbf{S}_m^{\mu}(\varphi) = \begin{pmatrix} \sin\left(m\varphi + \mu\dfrac{\pi}{2}\right) & 0 \\ 0 & \sin\left[m\varphi + (\mu - 1)\dfrac{\pi}{2}\right] \end{pmatrix},$$

this system of partial differential equations of the first order can be transformed to an infinite system of ordinary differential equations of the first order:

$$r\frac{d\mathbf{e}_m^{\mu}(r)}{dr} = \frac{1}{2}\sum_{\nu=0}^{1}(-1)^{\mu\nu}\left\{\sum_{j=0}^{m}\mathbf{A}_{j, m-j}^{\nu}(r)\mathbf{h}_j^{|\nu-\mu|}(r) + \frac{(-1)^{\nu}}{2^{\delta(m)}}\right.$$

$$\left.\times\sum_{j=0}^{\infty}[\mathbf{A}_{m+j, j}^{\nu}(r)\mathbf{h}_{m+j}^{|\nu-\mu|}(r) - (-1)^{\mu}\mathbf{I}\mathbf{A}_{j, m+j}^{\nu}(r)\mathbf{h}_j^{|\nu-\mu|}(r)]\right\},$$

$$r\frac{d\mathbf{h}_m^{\mu}(r)}{dr} = \frac{1}{2}\sum_{\nu=0}^{1}(-1)^{\mu\nu}\left\{\sum_{j=0}^{m}\mathbf{B}_{j, m-j}^{\nu}(r)\mathbf{e}_j^{|\nu-\mu|}(r) + \frac{(-1)^{\nu}}{2^{\delta(m)}}\right.$$

$$\left.\times\sum_{j=0}^{\infty}[\mathbf{B}_{m+j, j}^{\nu}(r)\mathbf{e}_{m+j}^{|\nu-\mu|}(r) + (-1)^{\mu}\mathbf{I}\mathbf{B}_{j, m+j}^{\nu}(r)\mathbf{e}_j^{|\nu-\mu|}(r)]\right\},$$

$$\mu = 0, 1, \quad m = 0, 1, \ldots.$$

Here,

$$\mathbf{A}_{mn}^{\nu}(r) = \begin{pmatrix} m\gamma\varepsilon_{2n-\nu}^{-1}(r) & \gamma^2\varepsilon_{2n-\nu}^{-1}(r) - \delta(n + \nu) \\ -k_0^2 r^2\gamma\delta(n + \nu) & m\delta(n + \nu) \end{pmatrix},$$

$$\mathbf{B}_{mn}^{\nu}(r) = \begin{pmatrix} m\gamma^{-1}\varepsilon_{2n-\nu}^{+1}(r) & \gamma^{-1}\varepsilon_{2n-\nu}^{+1}(r) - \gamma\delta(n + \nu) \\ k_0^2 r^2\varepsilon_{2n-\nu}^{+1}(r) & m\delta(n + \nu) \end{pmatrix},$$

$$\mathbf{I} = \begin{pmatrix} 1 & 0 \\ 0 & -1 \end{pmatrix}.$$

The continuous solution to the last system of equations decreases more rapidly than r^{-1} as $r \longrightarrow \infty$. This solution can be written in the form

$$\begin{pmatrix} \mathbf{e}_m^{\mu}(r) \\ \ldots\ldots \\ \mathbf{h}_m^{\mu}(r) \end{pmatrix} = \sum_{n,k=0}^{\infty}\sum_{\alpha,\nu=0}^{1} a_n^{\alpha\nu}\begin{pmatrix} {}^{\alpha}\mathbf{e}_{mnk}^{\mu\nu l} \\ \ldots\ldots \\ {}^{\alpha}\mathbf{h}_{mnk}^{\mu\nu l} \end{pmatrix}\left(\frac{r - r_{l-1}}{r_l - r_{l-1}}\right)^{\delta(l-1)m+k},$$

$$r_{l-1} \le r < r_l, \quad l = 1, 2, \ldots, N,$$

$$\begin{pmatrix} \mathbf{e}_m^{\mu}(r) \\ \ldots\ldots \\ \mathbf{h}_m^{\mu}(r) \end{pmatrix} = b_m^{\mu}\begin{pmatrix} 1 \\ \varepsilon_{00}mu^{-2} \\ 0 \\ \varepsilon_{00}F_m(r) \end{pmatrix} + c_m^{\mu}\begin{pmatrix} 0 \\ \gamma F_m(r) \\ -1 \\ \gamma mu^{-2} \end{pmatrix},$$

$$r_N \le r < \infty,$$

$$a_0^{00} = a_0^{11} = b_0^0 = c_0^1 = 0, \quad \mu = 0, 1, \quad m = 0, 1, \ldots,$$

where

$${}^{\alpha}\mathbf{e}_{mn0}^{\mu\nu 1} = \delta(|m - n| + |\mu - \nu|)\begin{pmatrix} (1 - \delta(n + 1 - \alpha))\gamma^{\alpha} \\ (\alpha - 1)m \end{pmatrix},$$

$${}^{\alpha}\mathbf{h}_{mn0}^{\mu\nu 1} = \delta(|m - n| + |\mu - \nu|) \times\begin{pmatrix} (1 - \delta(n + \alpha))\gamma^{1-\alpha}(\varepsilon_{00}^{+1, 1})^{\alpha} \\ (\alpha - 1)m \end{pmatrix},$$

$$\begin{pmatrix} {}^{\alpha}\mathbf{e}^{\mu\nu 1}_{mnk} \\ \cdots\cdots \\ {}^{\alpha}\mathbf{h}^{\mu\nu 1}_{mnk} \end{pmatrix} = \frac{1}{k(2m+k)}$$

$$\times \left(\begin{array}{c:c} (m+k)\mathbf{I}^2 & \mathbf{A}^{01}_{m00} \\ \hdashline \mathbf{B}^{01}_{m00} & (m+k)\mathbf{I}^2 \end{array}\right) \begin{pmatrix} {}^{\alpha}\mathbf{E}^{\mu\nu 1}_{m,n,k-1} \\ \cdots\cdots \\ {}^{\alpha}\mathbf{H}^{\mu\nu 1}_{m,n,k-1} \end{pmatrix},$$

$$k = 1, 2, \ldots,$$

$${}^{\alpha}\mathbf{e}^{\mu\nu l}_{mn0} = \sum_{k=0}^{\infty} {}^{\alpha}\mathbf{e}^{\mu,\nu,l-1}_{mnk}, \quad {}^{\alpha}\mathbf{h}^{\mu\nu l}_{mn0} = \sum_{k=0}^{\infty} {}^{\alpha}\mathbf{h}^{\mu,\nu,l-1}_{mnk},$$

$${}^{\alpha}\mathbf{e}^{\mu\nu l}_{m,n,k+1} = \frac{{}^{\alpha}\mathbf{H}^{\mu\nu l}_{mnk} - k\,{}^{\alpha}\mathbf{e}^{\mu\nu l}_{mnk}}{\rho_l(k+1)},$$

$${}^{\alpha}\mathbf{h}^{\mu\nu l}_{m,n,k+1} = \frac{{}^{\alpha}\mathbf{E}^{\mu\nu l}_{mnk} - k\,{}^{\alpha}\mathbf{h}^{\mu\nu l}_{mnk}}{\rho_l(k+1)},$$

$$k = 0, 1, \ldots, \quad l = 2, 3, \ldots, N,$$

$${}^{\alpha}\mathbf{E}^{\mu\nu l}_{mnk} = \frac{1}{2}\sum_{i=0}^{k}\sum_{p=0}^{1}(-1)^{\mu p}\Bigg[\sum_{j=0}^{m}\mathbf{B}^{pl}_{j,m-j,k-i}\,{}^{\alpha}\mathbf{e}^{|p-\mu|,\nu,l}_{jni}$$

$$+ \frac{(-1)^p}{2^{\delta(m)}}\sum_{j=0}^{\infty}\Big(\mathbf{B}^{pl}_{m+j,j,k-i}\,{}^{\alpha}\mathbf{e}^{|p-\mu|,\nu,l}_{m+j,n,i}$$

$$+ (-1)^{\mu}\mathbf{I}\mathbf{B}^{pl}_{j,m+j,k-i}\,{}^{\alpha}\mathbf{e}^{|p-\mu|,\nu,l}_{jni}\Big)\Bigg],$$

$${}^{\alpha}\mathbf{H}^{\mu\nu l}_{mnk} = \frac{1}{2}\sum_{i=0}^{k}\sum_{p=0}^{1}(-1)^{\mu p}\Bigg[\sum_{j=0}^{m}\mathbf{A}^{pl}_{j,m-j,k-i}\,{}^{\alpha}\mathbf{h}^{|p-\mu|,\nu,l}_{jni}$$

$$+ \frac{(-1)^p}{2^{\delta(m)}}\sum_{j=0}^{\infty}\Big(\mathbf{A}^{pl}_{m+j,j,k-i}\,{}^{\alpha}\mathbf{h}^{|p-\mu|,\nu,l}_{m+j,n,i}$$

$$- (-1)^{\mu}\mathbf{I}\mathbf{A}^{pl}_{j,m+j,k-i}\,{}^{\alpha}\mathbf{h}^{|p-\mu|,\nu,l}_{jni}\Big)\Bigg],$$

$$\mathbf{A}^{\nu l}_{mnk} = \begin{pmatrix} m\gamma\varepsilon^{-1,l}_{2n-\nu,k} & \gamma^2\varepsilon^{-1,l}_{2n-\nu,k} - \delta(k+n+\nu) \\ -\gamma k_0^2(\Delta r_l)^2\sum_{j=0}^{2}2^{\delta(1-j)}\rho_l^{2-j}\delta(|k-j|+n+\nu) & m\delta(k+n+\nu) \end{pmatrix},$$

$$\mathbf{B}^{\nu l}_{mnk} = \begin{pmatrix} m\gamma^{-1}\varepsilon^{+1,l}_{2n-\nu,k} & \gamma^{-1}\varepsilon^{+1,l}_{2n-\nu,k} - \gamma\delta(k+n+\nu) \\ k_0^2(\Delta r_l)^2\sum_{j=0}^{2}2^{\delta(1-j)}\rho_l^{2-j}\varepsilon^{+1,l}_{2n-\nu,k-j} & m\delta(k+n+\nu) \end{pmatrix},$$

$$\rho_l = \frac{r_{l-1}}{\Delta r_l}, \quad \Delta r_l = r_l - r_{l-1}, \quad \varepsilon^{il}_{n,-1} = \varepsilon^{il}_{n,-2} = 0,$$

$$F_m(r) = \frac{r\dfrac{d}{dr}[K_m(k_0 ur)]}{u^2[K_m(k_0 u r_N)]}, \quad u^2 = \gamma^2 - \varepsilon_{00} > 0.$$

The function $K_m(x)$ is the Macdonald function of an integral order m. The set of constants a_0^{01}, a_0^{10}, b_0^1, c_0^0, $a_n^{\alpha\nu}$, b_n^{ν}, c_n^{ν}, $\alpha, \nu = 0, 1$, $n = 1, 2, \ldots$ is the nontrivial solution to the homogeneous system of equations

$$\begin{pmatrix} \mathbf{e}^{\mu}_m(r) \\ \cdots\cdots \\ \mathbf{h}^{\mu}_m(r) \end{pmatrix}_{r=a-0} = \begin{pmatrix} \mathbf{e}^{\mu}_m(r) \\ \cdots\cdots \\ \mathbf{h}^{\mu}_m(r) \end{pmatrix}_{r=a+0},$$

$$\mu = 0, 1, \quad m = 0, 1, \ldots .$$

Equating the determinant of this system of equations to zero, we obtain after simple transformations the equation with respect to an unknown phase constant γ:

$$\det(\mathbf{PQ}) = 0,$$

where

$$\mathbf{Q} = (\mathbf{Q}_{ij}), \quad i, j = 1, 2, \ldots,$$

$$\mathbf{Q}_{2m+\mu,2n+\nu} = \sum_{k=0}^{\infty}\begin{pmatrix} {}^{0}\mathbf{e}^{\mu\nu N}_{mnk} & {}^{1}\mathbf{e}^{|\delta(m)-\mu|,|\delta(n)-\nu|,N}_{mnk} \\ {}^{0}\mathbf{h}^{\mu\nu N}_{mnk} & {}^{1}\mathbf{h}^{|\delta(m)-\mu|,|\delta(n)-\nu|,N}_{mnk} \end{pmatrix},$$

$$\mathbf{P} = (\mathbf{P}_{ij}), \quad i, j = 1, 2, \ldots,$$

$$\mathbf{P}_{2m+\mu,j} = \delta(2m+\mu-j)$$

$$\times\begin{pmatrix} -\varepsilon_{00}F_m(r_N) & 0 & \gamma m u^{-2} & 1 \\ -\varepsilon_{00} m u^{-2} & 1 & \gamma F_m(r_N) & 0 \end{pmatrix},$$

$$\mu, \nu = 0, 1, \quad m, n = 0, 1, \ldots,$$

$$m + \mu > 0, \quad n + \nu > 0.$$

This equation is the dispersion equation for guided modes of the waveguide under consideration.

In this equation, we now pass to the limit $\gamma \longrightarrow \sqrt{\varepsilon_{00}}$. As a result, we arrive at the equation

$$\det[\mathbf{RQ}(\gamma = \sqrt{\varepsilon_{00}})] = 0$$

with respect to an unknown wavelength $\lambda = \frac{2\pi}{k_0}$, which is the equation for critical wavelengths. Here,

$$\mathbf{R} = (\mathbf{R}_{ij}), \quad i, j = 1, 2, \ldots,$$

$$\mathbf{R}_{ij} = \delta(i - j)\begin{pmatrix} 1 & 0 & 0 & 0 \\ 0 & 0 & 1 & 0 \end{pmatrix}, \quad i = 1, 2, 3,$$

$$\mathbf{R}_{2m+\mu, j} = \delta(2m + \mu - j)\begin{pmatrix} \sqrt{\varepsilon_{00}} & 0 & 1 & 0 \\ \dfrac{4\pi^2\varepsilon_{00}r_N^2}{\lambda^2(m-1)} & 1 & 0 & 1 \end{pmatrix},$$

$$\mu = 0, 1, \quad m = 2, 3, \ldots.$$

It is evident that the order of determinants on the left-hand sides of the equations obtained is, in fact, equal to double the number of terms in the expansion into the Fourier series of the field components of the mode. The required number of these terms is determined only by the given accuracy.

REFERENCES

1. S. R. Rengarajan and J. E. Lewis, Radio Sci. **16**, 541 (1981).
2. V. I. Krivenkov, Dokl. Akad. Nauk **382**, 38 (2002) [Dokl. Phys. **47**, 9 (2002)].
3. C. Yeh, K. Ha, S. B. Dong, and W. P. Brown, Appl. Opt. **18**, 1490 (1979).
4. V. V. Shevchenko, Radiotekh. Électron. (Moscow) **31**, 849 (1986).
5. V. I. Krivenkov, Dokl. Akad. Nauk **378**, 751 (2001) [Dokl. Phys. **46**, 407 (2001)].

Translated by G. Merzon

Doklady Physics, Vol. 47, No. 11, 2002, pp. 808–810. Translated from Doklady Akademii Nauk, Vol. 387, No. 2, 2002, pp. 188–190.

PHYSICS

The Role of Mechanical Deformations of Burning Samples in the Relay Combustion of Gasless Systems

V. F. Proskudin

Presented by Academician Yu.A. Trutnev April 27, 2002

Received July 2, 2002

The relay combustion of gasless systems has been comprehensively studied both experimentally [1–3] and theoretically [4–7]. Relay combustion has remarkable properties. In particular, it ensures the conditions for the transformation of a substance via self-propagating high-temperature synthesis at higher (superadiabatic) temperatures [7]. These properties stimulate considerable interest in this combustion regime and its further investigation, including additional information about regularities and features revealed by studying the mechanism of the combustion of condensed systems. In particular, the inclusion of effects associated with the space–time development of mechanical deformations arising within burning samples both in the combustion-wave zone and in its vicinity would likely complement and make more adequate theoretical and experimental consideration of relay combustion.

The processes of arising mechanical deformations in burning gasless systems and their effect on the combustion process were considered by Merzhanov [8] and investigated in more detail in our later studies [9–13]. These studies revealed that the density of a condensed substance of a burning system is continuously redistributed behind (and, in some cases, ahead of) the combustion front. This redistribution can be detected by, e.g., pulsed X-ray radioscopy [9–11] and, when combustion is transferred through a bulkhead, can form a gap that is located near the bulkhead and increases in the process of combustion [10] (Fig. 1). Figure 2 shows the x–τ diagram illustrating the ballistics of the combustion of condensed systems, i.e., the transport dynamics of the particles of burning samples involving two gasless systems separated by an inert bulkhead.

A similar phenomenon accompanied by the appearance of a time-dependent gap in a burning gasless system can occur not only in the presence of an inert bulkhead but also in the presence of the only free interface between individual parts of the burning condensed system. When the combustion front approaches this interface, mechanical deformations in the part of the sample having been burned produce a gap near the interface. This gap serves as a bulkhead with virtually zero heat capacity and ensures delay of the combustion wave, i.e., superadiabatic combustion of the heated layer following the gap. The presence of numerous interfaces spaced by a step close to the width of the layer heated in delay time must give rise to the superadiabatic relay

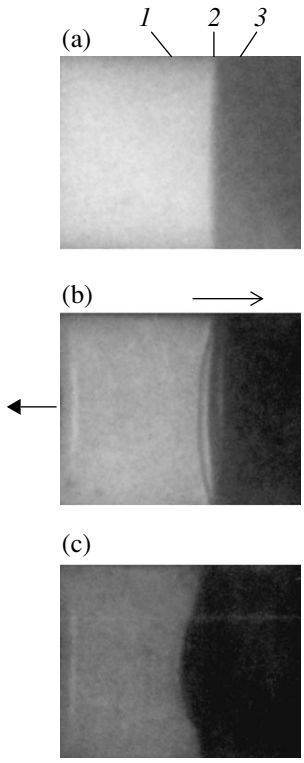

Fig. 1. X-ray images of the samples involving two gasless systems separated by an inert bulkhead [7]: (a) before burning, (b) at the instant of combustion transfer through the bulkhead, (c) after burning; (*1*) the $Cr_2O_3 + 2Al + 4B$ sample (relative pressing density 0.6), (*2*) the 0.4-mm-thick stainless steel bulkhead, (*3*) the Nb + B sample (relative pressing density 0.7), (←) the direction of gas emission from the half-closed hard shell, and (→) the direction of motion of the combustion front.

Russian Federal Nuclear Center All-Russia Research Institute of Experimental Physics, Sarov, Nizhni Novgorod oblast, 607200 Russia

1028-3358/02/4711-0808$22.00

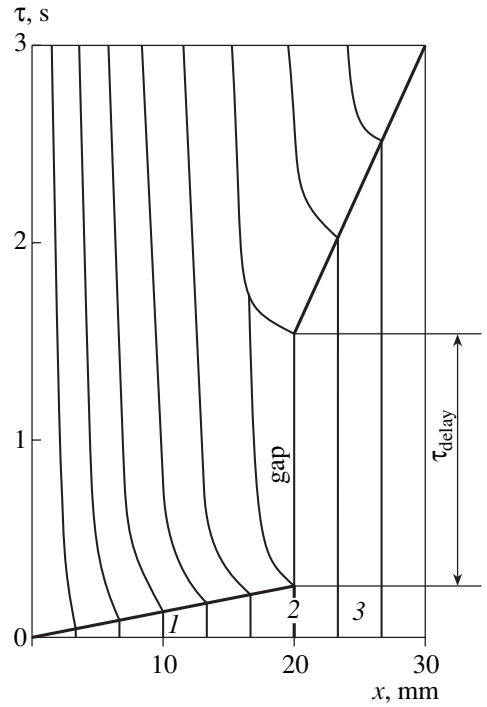

Fig. 2. Ballistic characteristic of mechanical deformations (substance displacement) of two burning gasless systems separated by an inert bulkhead; x is the coordinate of the particles of samples along the direction of motion of the combustion front, τ is time, (*1*) is the $Cr_2O_3 + 2Al + 4B$ system, (*2*) is the inert bulkhead, (*3*) is the Nb + B system, and τ_{delay} is the delay time of motion of the combustion front.

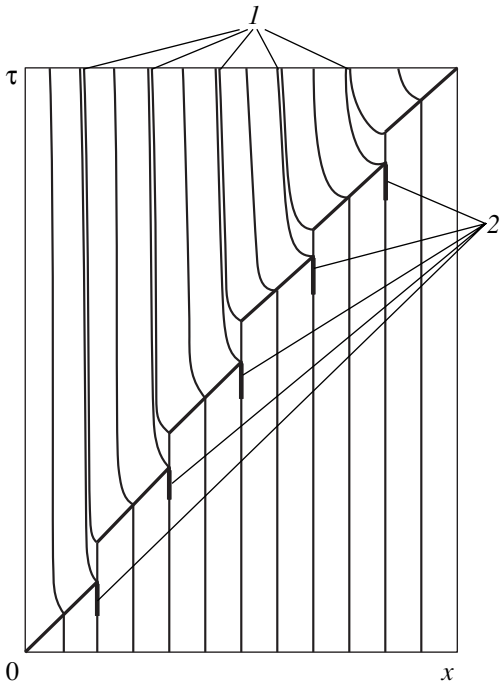

Fig. 3. Ballistic characteristic of mechanical deformations (substance displacement) of a gasless system burning in the relay mode induced by transverse cracks arising ahead of the combustion front: (*1*) interfaces between neighboring slag "clots" and (*2*) the onset of the formation of transverse cracks in the sample.

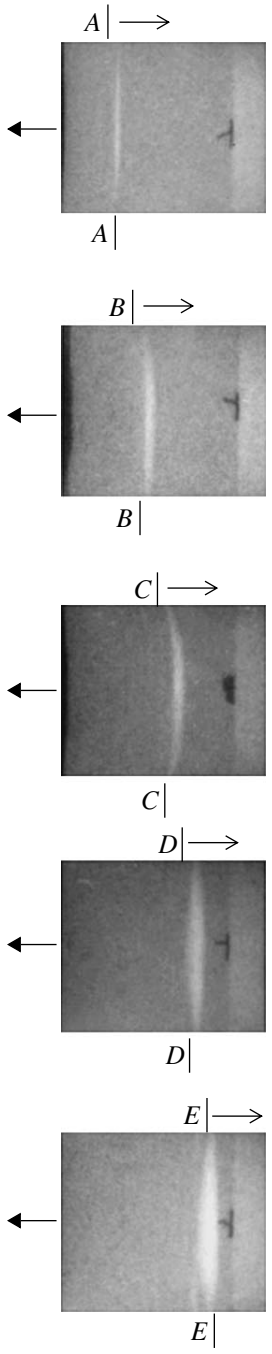

Fig. 4. X-ray images of the burning sample placed within the half-closed hard shell [11] at various times; *AA*, *BB*, *CC*, *DD*, and *EE* are the positions of the combustion front at the X-ray radioscopy time estimated from the relation $l_{front} = l_{sample}\frac{\tau_{X\text{-}ray}}{\tau_{comb}}$, where l_{front} is the path covered by the combustion front to the time of pulse X-ray radioscopy, l_{sample} is the sample length, $\tau_{X\text{-}ray}$ is the time interval from the onset of sample combustion to the instant of pulse X-ray radioscopy, τ_{comb} is the time of sample combustion, (◄–) is the direction of the admixture-gas emission from the half-closed hard shell, and (→) is the direction of motion of the combustion front.

regime of the combustion of the system. These interfaces within the system can be formed intentionally beforehand by, e.g., producing a sample as a set of thin disks [3]. At the same time, these interfaces in certain condensed systems can spontaneously arise as transverse cracks formed ahead of the combustion front in an originally continuous sample [14, 15].

Figure 3 shows the ballistic combustion characteristic for the combustion mode of the gasless system, where transverse cracks are periodically formed ahead of the combustion front and gaps are then developed. The possibility of the appearance of cracks ahead of the combustion front in certain condensed systems was demonstrated in experiments [14, 15]. The possibility of developing gaps in the combustion front zone of the originally continuous gasless system due to mechanical deformations arising in the burning sample was seen in pulse X-ray images that were obtained by me, E.N. Belyaev, L.A. Zhuravleva *et al.*, when we studied a quasi-thermite mixture that is doped with amorphous boron and pressed with a relative density of ~0.7 into a half-closed shell by the method presented in [11] (Fig. 4).

Thus, since the mechanical deformations of a burning sample change permanently in actual condensed systems, one can expect that the gas gap varies substantially both in time and in space (in length and radius of the sample). This variation leads to constant change in the burning-medium heterogeneity scale, which substantially affects the parameters of relay combustion [7]. To analyze this phenomenon and to take it into account in the future description of relay combustion in actual condensed systems, one can use pulsed X-ray radioscopy of burning samples (solid or consisting of thin disks stacked with or without gaps) with further plotting of the x–τ diagram, as was done, e.g., in [11]. This procedure will make it possible to answer the question of whether mechanical deformations in a given specific sample must be taken into account to optimize the conditions of the superadiabatic relay combustion.

ACKNOWLEDGMENTS

I am grateful to A.G. Leshchinskaya for assistance in manuscript preparation and P.G. Berezhko for support.

REFERENCES

1. S. G. Vadchenko and A. G. Merzhanov, Dokl. Akad. Nauk **352** (4), 487 (1997).
2. S. G. Vadchenko, Fiz. Goreniya Vzryva **37** (2), 42 (2001).
3. S. G. Vadchenko, Fiz. Goreniya Vzryva **38** (1), 55 (2002).
4. A. G. Merzhanov, Dokl. Akad. Nauk **353** (4), 504 (1997).
5. A. G. Merzhanov, A. N. Peregudov, and V. T. Gontkovskaya, Dokl. Akad. Nauk **360** (2), 217 (1998).
6. A. S. Rogachev and A. G. Merzhanov, Dokl. Akad. Nauk **365** (6), 788 (1999).
7. A. G. Merzhanov, P. M. Krishenik, and K. G. Shkadinskiĭ, Dokl. Akad. Nauk **380** (3), 323 (2001) [Dokl. Phys. **46**, 619 (2001)].
8. A. G. Merzhanov, Preprint of OIKhF (Department of Inst. Chem. Phys., Chernogolovka, 1978).
9. V. A. Golubev, P. G. Berezhko, V. F. Proskudin, *et al.*, Fiz. Goreniya Vzryva **27** (2), 94 (1991).
10. V. A. Golubev, V. F. Proskudin, P. G. Berezhko, *et al.*, Fiz. Goreniya Vzryva **27** (5), 41 (1991).
11. V. F. Proskudin, V. A. Golubev, and P. G. Berezhko, Fiz. Goreniya Vzryva **33** (4), 78 (1997).
12. V. F. Proskudin, V. A. Golubev, P. G. Berezhko, *et al.*, Fiz. Goreniya Vzryva **34** (6), 43 (1998).
13. V. F. Proskudin, Fiz. Goreniya Vzryva **37** (6), 71 (2001).
14. A. A. Butakov, D. A. Vaganov, and S. N. Leont'ev, Combust. Sci. Technol. **106** (1–3), 137 (1995).
15. B. Sh. Braverman, M. Kh. Ziatdinov, and Yu. M. Maksimov, Fiz. Goreniya Vzryva **38** (1), 43 (2002).

Translated by R. Tyapaev

Doklady Physics, Vol. 47, No. 11, 2002, pp. 811–814. Translated from Doklady Akademii Nauk, Vol. 387, No. 2, 2002, pp. 191–195.

PHYSICS

Computer Simulation of the Properties of MgO–CaO Solid Solutions with Allowance for Short-Range Order

Corresponding Member of the RAS V. S. Urusov, T. G. Petrova, and N. N. Eremin

Received June 7, 2002

For a long time in many investigations, the mixing energies and stability boundaries of solid solutions with varying composition were calculated by using phenomenological theory [1–3]. According to this theory, the mixing enthalpy ΔH_{mix} of solid solutions, in particular, MO–M'O with NaCl-type structure is determined as

$$\Delta H_{mix} = \frac{9}{4}x_1x_2VK\left(\frac{\Delta R}{R}\right)^2 = \frac{1}{4}x_1x_2VK\left(\frac{\Delta V}{V}\right)^2, \quad (1)$$

where x_1 and x_2 are the mole fractions of the components; K is the bulk modulus; $\Delta R = R_2 - R_1$ and $\Delta V = V_2 - V_1$ are the differences between interatomic spacings and molar volumes in crystals of pure components, respectively; and R is the average interatomic spacing, which additively depends on composition according to Vegard's law

$$R = x_1R_1 + x_2R_2, \quad (2)$$

and V is the average molar volume obeying the Retgers law

$$V = x_1V_1 + x_2V_2. \quad (3)$$

The product VK is almost constant and equal to ~2000 kJ/mol for MO-type oxides [2, 3].

In recent years, more precise prediction of the mixing properties for solid solutions has become possible due to computer simulation using semiempirical interatomic potentials. The first such calculations were recently carried out for solid solutions in the MnO–NiO, MgO–MnO, and CaO–MnO [4] and CaO–MgO [5] systems. In addition, the structure and properties of oxide solid solutions were recently calculated for the first time by quantum-mechanical (*ab initio*) methods [4, 6]. As was emphasized by one of us (V.S.U.) [7], the principal disadvantage of such calculations was the choice of too small a cell (supercell) containing from 4 to 16 atoms (32 atoms as a maximum). This choice makes it impossible to adequately reproduce the local structure of a solid solution, because the possibility of describing various atomic configurations of the solid solution by means of such cells is very limited, and only certain ordered structures (in fact, some hypothetical stoichiometric phases) are reproduced in the majority of cases.

Therefore, the principal simulation problems outlined in [7] are, first, to use a larger supercell and, second, to determine the order parameter for each individual atomic configuration, whose energy is minimized in the computer experiment.

To develop such a methodology, we choose the method of semiempirical pair potentials, which allows calculation with reasonably large supercells. As a model system, we take the binary solid solution MgO–CaO, which was often studied by other methods both theoretically and experimentally.

The short-range contributions to the pair potentials of interaction are chosen in the form of the algebraic sum of the Buckingham potential

$$V_{ij}(R_{ij}) = \lambda_{ij}\exp\left(-\frac{R_{ij}}{\rho_{ij}}\right) - \frac{C_{ij}}{R_{ij}^6} \quad (4)$$

and the Morse potential

$$V_M = D_{ij}\{1 - \exp[-\beta_{ij}(R_{ij}^0 - R_{ij})]\}^2 - D_{ij}. \quad (5)$$

Here, λ_{ij} and D_{ij} are the fitting parameters and D_{ij} can be defined as the breaking energy for a single covalent bond. The quantity R_{ij}^0 is usually taken to be equal to the average interatomic spacing (or to the sum of atomic radii) for the corresponding atomic pair. The parameter β_{ij} of the Morse potential and the parameter ρ_{ij} of the Buckingham potential are often known from empirical correlations [8] but can also be refined by fitting. The term $\frac{C_{ij}}{R_{ij}^6}$ in Eq. (4) describes the dispersion interaction. The cohesive energy is expressed as the sum of pair potentials, which also involves the Coulomb interaction between all the ion pairs. Morse potential (5) was introduced with a certain weight

Moscow State University, Vorob'evy gory, Moscow, 119899 Russia

1028-3358/02/4711-0811$22.00

Table 1. Parameters of interatomic-interaction potentials for MgO and CaO

Potential	Ion charge, Å	λ, eV *D*, eV	ρ, Å β, Å^{-1}	*C*, eV Å^6 R_0, Å
V_B(Mg–O)	±2.0	1428.5	0.2945	0.000
V_B(Ca–O)		1090.40	0.3437	0.000
V_B(Mg–O)	±1.7	1044.89	0.2945	0.0
V_M(Mg–O)		0.0007	4.15	2.2
V_B(Ca–O)		714.49	0.3437	0.0
V_M(Ca–O)		0.07	2.27	2.5
V_B(Mg–O)	±1.4	763.36	0.2945	0.000
V_M(Mg–O)		0.264	1.698	2.2
V_B(Ca–O)		602.41	0.3437	0.000
V_M(Ca–O)		0.403	1.455	2.5

Table 2. Unit cell parameters and bulk moduli for pure MgO and CaO

Ion charge, *e*	MgO				CaO			
	a, Å		*K*, GPa		*a*, Å		*K*, GPa	
	exp.	theor.	exp.	theor.	exp.	theor.	exp.	theor.
±2.0	4.204	4.198	165	180	4.810	4.807	116	136
±1.7	–	4.199	–	175	–	4.809	–	120
±1.4	–	4.200	–	163	–	4.791	–	113

depending on a fraction of the bond covalence, which varies from 0 for the pure ionic approximation to 1 for the pure covalent one [8].

The energy minimum was sought by varying atomic coordinates and unit-cell parameters with the GULP software package [9], which makes it possible to calculate both the structure parameters and the optimum values for interatomic potentials. The parameters of the Buckingham (4) and Morse (5) potentials were obtained by fitting the structures and elastic properties of pure CaO and MgO (Tables 1 and 2) for effective charges of cations and anions $zf = \pm 1.4e$, $\pm 1.7e$, and $\pm 2.0e$, which corresponds to a bond ionicity $f = 0.7$, 0.85, and 1.0. In Table 2, it can be seen that the best agreement with experiment is achieved for $zf = \pm 1.7e$, which agrees with the evidence of the high ionicity of the bond in the oxides under study ($f = 0.85$ in this case).

To calculate the structures and energies of solid solutions, we chose the $4 \times 4 \times 4$ supercell with quadruplicate parameters of the NaCl-type structure containing 512 atoms, because smaller cells cannot provide the statistical distribution of mutually substituted atoms characterizing an ideal or regular solid solution. The symmetric restrictions were removed, because atoms are displaced, and therefore cell parameters are distorted during the formation of a solid solution.

The enthalpy of mixing has the form

$$\Delta H_{mix} = U_{s.sol}(x) - xU_1 - (1-x)U_2, \quad (6)$$

where x is the mole fraction of the pure component CaO; and U_1 and U_2 are the structural energies of pure CaO and MgO, respectively. The enthalpy of mixing was obtained for three compositions of $Ca_xMg_{1-x}O$ with $x = 0.25$, 0.50, and 0.75.

In the $A_xB_{1-x}O$ solid solutions with NaCl-type structure, the nearest neighboring atoms A and B; i.e., the atoms located in the second coordination sphere (cubooctahedron, coordination number 12) relative the given one can be arranged in different ways. The composition and symmetry of all the possible configurations, whose number is approximately equal to 2000, were given in [3, 10]. The pattern of the mutual arrangement of atoms within this sphere can be characterized by the Bragg–Williams short-range order parameter σ [11]

$$\sigma = \frac{\bar{q} - q_{min}}{q_{max} - q_{min}}, \quad (7)$$

which is equal to 1 and 0 for completely ordered and disordered states, respectively. Here, the ratio $\bar{q}$ of the number of unlike A–B pairs to the total number of cation pairs in the second coordination sphere is averaged over all the 256 cations of the structure, q_{min} corresponds to a disordered solid solution with a minimum number of unlike pairs and is proportional to $2x(1-x)$, and q_{max} corresponds to the most ordered solid solution forming certain superstructures for the ratio $\frac{x}{1-x}$ = 1.0, 0.25, and 0.75 (1 : 1, 1 : 3, and 3 : 1).

For the composition $A_{0.5}B_{0.5}O$ (1 : 1), ordered structures are formed for the layer-by-layer alternation of A and B atoms (such as …ABAB…) along one of the symmetry axes. When the layers are arranged along the four- or three-fold axes, structures of the CuAu, CuPt, or $LiFeO_2$ type are formed with tetrahedral (CuAu, $LiFeO_2$) or rhombohedral (CuPt, $LiFeO_2$) distortions of the initial structure. In this case, the parameters q_{min} and q_{max} can be determined as $q_{min} = 2 \times 0.5 \times 0.5 = 0.5$ and $q_{max} = \frac{8}{12} = 0.6667$ (among 12 cations surrounding of each cation in the CuAu structure, 8 cations are atoms of another type). For the $A_{0.25}B_{0.75}O$ and $A_{0.75}B_{0.25}O$ compositions, the ordered structure is formed when B atoms are located in the vertices and A atoms, in the centers of cubic-cell faces and *vice versa*. This type of structural ordering is observed in many A_3B alloys. In this case, $q_{min} = 2 \times 0.25 \times 0.75 = 0.375$ and $\bar{q}_{max} = 0.5$ (the latter is an average value, because three quarters and one quarter of cations of the structure have 4 and

12 cations of another type in the surrounding area, respectively).

Now, it is possible to calculate σ for an arbitrary configuration of the composition and to plot the energy of formation of a solid solution as a function of the short-range order parameter. Figure 1 shows these plots for the optimum parameters $f = 0.85$ and $x = 0.25$, 0.50, and 0.75. It is seen that relatively large sizes of the supercell and a great number of atoms are insufficient to generate a completely disordered structure. Therefore, to determine ΔH_{mix} for a disordered solution, we are forced to linearly extrapolate the enthalpy of mixing to $\sigma = 0$ by the least-squares method. Using the resulting $\Delta H_{mix(\sigma = 0)}$ values, we can plot the energy of formation of a disordered solid solution as a function of composition. Figure 2 shows our $\Delta H_{mix(x)}$ values, the results of calculations [4, 6], and the curve ΔH_{mix} calculated by Eq. (1) with $VK_{av} = 1900(20)$ kJ/mol.

In this study, we aim to determine properties of a nonideal solid solution such as deviations of volume from Retgers law (3) and the bulk modulus from additivity by computer simulation. These deviations $\Delta V_{mix}(x)$ and $\Delta K(x)$ are shown in Figs. 3 and 4. It is seen that $\Delta V_{mix}(x)$ and $\Delta K(x)$ are distinctly positive and negative, respectively.

If the cell parameters or interatomic spacings follow Vegard's law (2), $\Delta V_{mix}(x)$ is certainly negative:

$$\Delta V_{mix} = -x_1 x_2 (\Delta a)^2 (a + a_1 + a_2), \quad (8)$$

where the unit-cell parameter $a = x_1 a_1 + x_2 a_2$ and $\Delta a = a_2 - a_1$.

However, NaCl-type solid solutions exhibit a positive deviation of cell parameters from Vegard's law, which can be expressed in the form [2, 3]

$$\Delta a = 3 x_1 x_2 \frac{(\Delta a)^2}{a}. \quad (9)$$

In this case, the calculations show that $\Delta V_{mix}(x)$ corresponds to the total positive deviation from additivity and with a good accuracy is equal to

$$\Delta V_{mix} \simeq 6 x_1 x_2 (\Delta a)^2 (x_1 a_2 + x_2 a_1). \quad (10)$$

Comparing all three models (Fig. 3), we conclude that the model with allowance for a positive deviation of Vegard's law from additivity [Eqs. (9) and (10)] agrees satisfactorily with the results of computer simulation, particularly taking into account the fact that Eq. (10) gives an upper estimate of ΔV_{mix}.

The deviation of the bulk modulus K from additivity can be calculated by the formulas [12]

$$\Delta K_x = \frac{(K_1 - K_2)E}{1 + Ex_1} x_1 (1 - x_1), \qquad \Delta K_x = x_1 x_2 D, \quad (11)$$

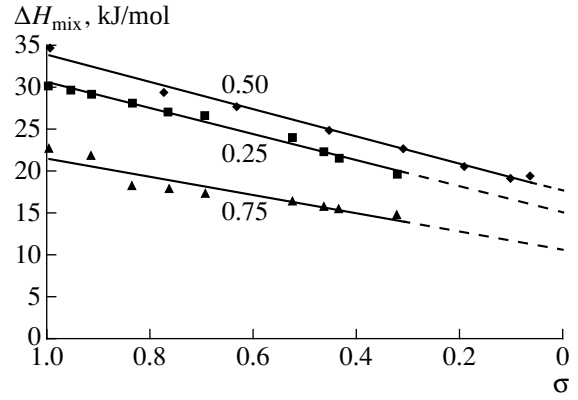

Fig. 1. Enthalpy of formation of solid solutions with 0.25, 0.50, and 0.75 mole fractions of CaO as a function of the short-range order parameter σ.

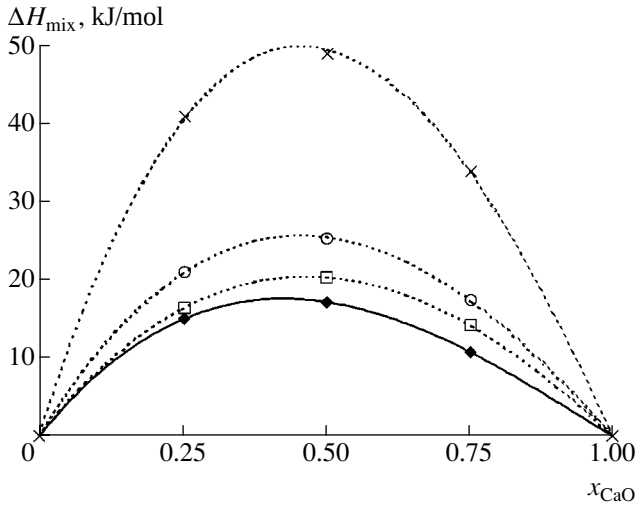

Fig. 2. Enthalpy of mixing for the disordered solid solution MgO–CaO: (◆) our calculation, (□) calculation by phenomenological Eq. (1), and (○) simulation by *ab initio* methods [6] and (×) [5].

where

$$E = \frac{V_1 K_2}{V_2 K_1} - 1, \qquad D = \frac{(K_1 - K_2)[(K_1 V_1)^2 - (K_2 V_2)^2]}{2 K_1 K_2 V_1 V_2}, \quad (12)$$

K_1 and K_2 are the compression moduli of pure components, and V_1 and V_2 are the molar volumes of pure components. The curves calculated by Eqs. (11) and (12) are shown in Fig. 3. It is seen that the negative deviation $\Delta K(x)$ from additivity is predicted by the computer simulation in general agreement with other models.

Experiments and calculations for various structural configurations and solid-solution compositions can

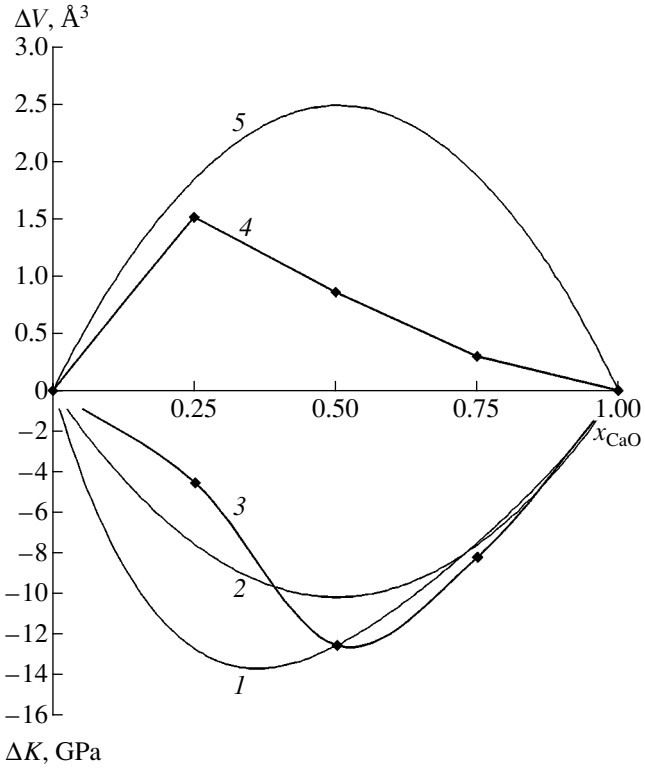

Fig. 3. Deviation of the bulk modulus K from additivity: (*1*) Eq. (11), (*2*) Eq. (12), and (*3*) this study; and the deviation of unit-cell volume V from additivity: (*4*) this study and (*5*) with deviation from Vegard's law (9), (10).

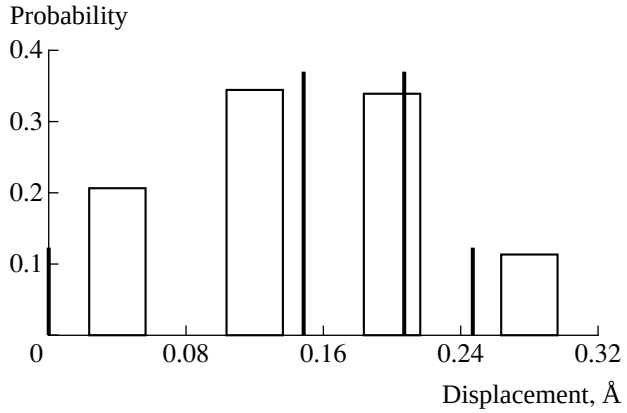

Fig. 4. Histogram of the displacements of oxygen atoms from their regular positions. Vertical lines are predictions of the phenomenological model [2, 3].

provide information about their local structure [13]. Figure 4 shows the calculated histogram of the displacements of oxygen atoms from their regular positions for the composition with $x = 0.5$ and order parameter $\sigma = 0.07$. These results can be compared with the geometrical model of displacements of a common atom from its standard position in NaCl-type solutions [2, 3]. The probabilities of displacements 0, $\frac{\Delta R}{2}$, $\frac{\sqrt{2}\Delta R}{2}$, and $\frac{\sqrt{3}\Delta R}{2}$ are shown in Fig. 4. Reasonably good agreement between the two models is evident, but the computer simulation gives a much more detailed pattern of the distribution of atomic displacements.

REFERENCES

1. V. S. Urusov, *Theory of Isomorphous Mixture* (Nauka, Moscow, 1977).
2. V. S. Urusov, V. L. Tauson, and V. V. Akimov, *Geochemistry of Solids* (GEOS, Moscow, 1997).
3. V. S. Urusov, in *Solid Solution in Oxides and Silicates. EMU Notes* (Eötvös Univ. Press, Budapest, 2001), vol. 3, pp. 121–153.
4. M. Konigstein, F. Kora, and C. R. A. Catlow, J. Solid State Chem. **37**, 261 (1998).
5. P. D. Tepesh, A. F. Kohan, G. D. Garbulsky, *et al.*, J. Am. Ceram. Soc. **79**, 2033 (1996).
6. M. Yu. Lavrentiev, N. L. Allan, G. D. Barrera, and J. A. Purton, J. Phys. Chem. B **105**, 3594 (2001).
7. V. S. Urusov, J. Solid State Chem. **153**, 357 (2001).
8. V. S. Urusov and L. S. Dubrovinskiĭ, *Computer Simulation of the Structure and Properties of Minerals* (Mosk. Gos. Univ., Moscow, 1989).
9. J. D. Gale, *GULP—User's Manual* (London Royal Institution and Imperical College, London, 1997).
10. V. S. Urusov and I. Yu. Kantor, Izv. Akad. Nauk, Ser. Fiz. **66** (6), 876 (2002).
11. W. L. Bragg and R. J. Williams, Proc. R. Soc. London, Ser. A **145**, 699 (1934); **151**, 540 (1935); **152**, 231 (1935).
12. D. L. Fancher and G. R. Barch, J. Phys. Chem. Solids **32**, 1303 (1971).
13. V. S. Urusov, in *Structural Crystallography* (Nauka, Moscow, 1992), pp. 59–80.

Translated by V. Bukhanov

Doklady Physics, Vol. 47, No. 11, 2002, pp. 815–818. Translated from Doklady Akademii Nauk, Vol. 387, No. 3, 2002, pp. 321–325.

PHYSICS

Investigation of the Features of the Fine Structure of Crystals by the Method of Plasma Reflection

A. S. Mal'tsev, V. A. Petrovsky, S. A. Troshev, and A. E. Sukharev

Presented by Academician A.I. Leont'ev February 27, 2002

Received February 27, 2002

Various microdefects are of wide interest for fundamental and applied investigations of both natural and man-made crystals. Therefore, the development of highly informative express methods for studying these defects is a topical problem. The aim of this study is to experimentally and theoretically investigate the features in the behavior of optical functions in the range of plasma resonance, which is observed when IR radiation is reflected from the surface of a crystal containing diverse defects. We investigated anisotropic single crystals of Bi and Bi/Sb solid solutions that were both pure and doped with donor (Te) and acceptor (Sn) and belonged to the class of semimetals and semiconductors with the $R_{\bar{3}m}$ symmetry group, in which the distribution of the impurity atoms along the length of a crystal grown from a melt under actual conditions is complicated.

In general, IR radiation interacts with crystals of this class via many mechanisms that are exhibited in reflection spectra in the form of the following main effects: plasma effects; polarization effects associated with the crystal anisotropy; effects of interband transitions (direct and indirect); and photon–phonon, plasmon–phonon, and electron–plasmon effects [1–7, 13, 14].

Samples for investigation were cut from the central parts of crystals (grown by the floating-zone method) by spark cutting and were then chemically polished. Concentration of composition was checked with a CAMEBAX electron-probe microanalyzer. The reflectance spectra for nonpolarized and polarized radiation beams with the polarization-plane orientation $\mathbf{E} \parallel C_3$ and $\mathbf{E} \perp C_3$ (C_3 is the optical axis of a crystal) were recorded by IFS-113V and LAFS-1000 Fourier spectrometers in the range of 10–1000 cm^{-1} with a resolution of 2 cm^{-1}.

Microprobe investigations with a JSM-6400 scanning electron microscope revealed diverse defects, in particular, in the form of microcracks and microperiodicities. In [8], it was established that heterostructures rather than substitutional solid solutions were formed in bismuth doped with elements of groups IV and VI of the periodic table. These heterostructures consists of semimetal matrices with inclusions (clusters) involving atoms of introduced impurities, atoms of matrix components, and compounds of impurity atoms with bismuth.

Figure 1 shows the IR reflectance spectra for the samples at T = 80 K. These spectra have a form typical of plasma reflection and have additional peaks in the region of the plasma minimum, which cannot be explained in the framework of the classical Drude model, by polarization effects, effects of interband transitions, or photon–phonon and plasmon–phonon interactions.

To explain the observed effects, we use the theory of elementary excitations in a solid [7], as well as studies [9–12], where the effect of different scattering centers on the dynamic resistivity $\rho(\omega)$ of semiconductor crystals was shown.

In order to consider IR radiation from crystal surfaces in different parts of the spectrum, it is necessary to determine the frequency dependence of the complex permittivity of a crystal, because this dependence is

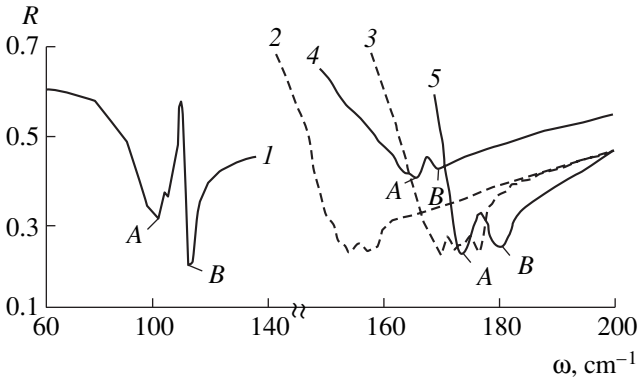

Fig. 1. Reflectance spectra of polarized radiation for BiSn alloys at T = 80 K: (*1*) $BiSn_{0.03}$ ($\mathbf{E} \parallel C_3$), (*2*) $BiSn_{0.01}$ ($\mathbf{E} \parallel C_3$), (*3*) $BiSn_{0.01}$ ($\mathbf{E} \perp C_3$), (*4*) $BiSn_{0.02}$ ($\mathbf{E} \perp C_3$), and (*5*) $BiSn_{0.02}$ ($\mathbf{E} \parallel C_3$).

Institute of Geology, Komi Scientific Center, Ural Division, Russian Academy of Sciences, ul. Pervomaĭskaya 54, Syktyvkar, 167982 Russia

1028-3358/02/4711-0815$22.00

responsible for the dependence of the reflectivity $R(\omega)$ on the frequency of the incident electromagnetic wave.

In general, the dielectric function ε and dynamic resistivity $\rho(\omega, \gamma)$ are related as

$$\varepsilon(k = 0, \omega, \gamma) = \varepsilon_L + \frac{i}{\varepsilon_0 \omega}\rho(\omega, \gamma)^{-1}, \quad (1)$$

where ε_L is the permittivity determined by virtual transitions at frequencies far from the plasma resonance; γ is the inverse relaxation time of the basic charge carriers [electrons and (or) holes]; and k is the momentum transferred by a charge carrier.

For normal incidence of a beam on the sample surface, the reflection coefficient $R(\omega)$ and the dielectric-function $Z(\omega)$ are calculated by the well-known formulas

$$R(\omega) = \frac{\sqrt{\varepsilon_1^2 + \varepsilon_2^2} - \sqrt{2(\varepsilon_1 + \sqrt{\varepsilon_1^2 + \varepsilon_2^2})} + 1}{\sqrt{\varepsilon_1^2 + \varepsilon_2^2} + \sqrt{2(\varepsilon_1 + \sqrt{\varepsilon_1^2 + \varepsilon_2^2})} + 1}, \quad (2)$$

$$Z(\omega) = \frac{\varepsilon_2}{\varepsilon_1^2 + \varepsilon_2^2},$$

where ε_1 and ε_2 are the real and imaginary parts of the complex permittivity $\varepsilon = \varepsilon_1 + i\varepsilon_2$, respectively.

In general, $\rho(\omega, \gamma)$ is determined by the expression [12]

$$\rho(\omega, \gamma) = -\frac{im}{ne^2}(\omega + i\gamma) + \frac{iN}{(2\pi)^3 \varepsilon_0 n^2 e^2 \omega}\int d^3k \frac{k_x^2}{k^2}|q_f(k)|^2\left(\frac{1}{\varepsilon(k, \omega, \gamma)} - \frac{1}{\varepsilon(k, 0, \gamma)}\right), \quad (3)$$

where m and n are the effective mass and concentration of charge carriers, respectively; N is the concentration of defects; e is the electron (hole) charge; $q_f(k)$ is the Fourier transform of the spatial distribution of change defects; and $\varepsilon(k, \omega, \gamma)$ is the permittivity of charge carriers in the Linchard approximation.

Now, we introduce the auxiliary function $F(k)$:

$$ne^2 F(k) = N|q_f(k)|^2. \quad (4)$$

Then, substituting Eq. (3) into Eq. (1) and taking Eq. (4) into account, we arrive at the expression

$$\varepsilon(\omega, \gamma) = \varepsilon_L\left(1 - \frac{\omega_p^2}{\omega(\omega + i\gamma)}\frac{1}{1 - \frac{\omega_p^2 \varepsilon_L}{(2\pi)^3 n\omega(\omega + i\gamma)}\int d^3k \frac{k_x^2}{k^2}F(k)\left(\frac{1}{\varepsilon(k, \omega, \gamma)} - \frac{1}{\varepsilon(k, 0, \gamma)}\right)}\right), \quad (5)$$

where $\omega_p^2 = \frac{ne^2}{\varepsilon_L \varepsilon_0 m}$ is the plasma frequency of the charge carriers.

Representing the integral entering in Eq. (5) in the form of the real and imaginary parts

$$F(\omega, \gamma) = F_1(\omega, \gamma) + iF_2(\omega, \gamma) = \frac{\omega_p^2 \varepsilon_L}{(2\pi)^3 n}\int d^3k \frac{k_x^2}{k^2}F(k)\left(\frac{1}{\varepsilon(k, \omega, \gamma)} - \frac{1}{\varepsilon(k, 0, \gamma)}\right), \quad (6)$$

we obtain the expressions [15]

$$\varepsilon(\omega, \gamma) = \varepsilon_L\left[1 - \frac{\omega_p^2}{\omega\left[\omega + i\left(\gamma + \frac{iF_1(\omega, \gamma) - F_2(\omega, \gamma)}{\omega}\right)\right]}\right] \quad (7)$$

$$= \varepsilon_L\left[1 - \frac{\omega_p^2}{\omega[\omega + \mathrm{Re}\,Y(\omega) + i \cdot \mathrm{Im}\,Y(\omega)]}\right],$$

where

$$\mathrm{Re}\,Y(\omega, \gamma) = \gamma - \frac{F_2(\omega, \gamma)}{\omega}, \quad \mathrm{Im}\,Y(\omega, \gamma) = \frac{F_1(\omega, \gamma)}{\omega}; \quad (8)$$

and $Y(\omega)$ is the frequency-dependent attenuation coefficient inverse to the relaxation time of the system.

In what follows, we investigate the behavior of $R(\omega)$, $Z(\omega)$, $\mathrm{Re}\,Y(\omega)$, and $\mathrm{Im}\,Y(\omega)$ with permittivity (7) for the following types of defects: clusters, layers, and ion pairs.

CLUSTER MODEL

We consider a crystal uniformly doped with an impurity with the atom concentration of the background N_b. In addition, impurity atoms are surrounded by ions of spherically symmetric concentration N_c with the Gaussian distribution density

$$P(r) = \Delta N \exp\left(-\frac{r^2}{s^2}\right), \quad (9)$$

where ΔN is the density of ion concentration at the cluster center, s is the mean cluster radius, and r is the distance from the cluster center.

Finding the Fourier transform of the distribution of the cluster charge with ion concentration density (9) and integrating with respect to the angles in Eq. (3), we reduce Eq. (6) to the form

$$F(\omega, \gamma) = \frac{\varepsilon_L \omega_p^2}{6\pi^2 n}\int dk k^2 \left(1 + \frac{N_c e^2 \Delta N^2 s^6 \pi^3}{n} \exp\left(-\frac{k^2 s^2}{2}\right)\right)\left(\frac{1}{\varepsilon(k, \omega, \gamma)} - \frac{1}{\varepsilon(k, 0, \gamma)}\right), \quad (10)$$

where $N_b + N_c \Delta N s^3 \pi^{3/2} = n$.

Figure 2 shows the optical functions obtained by Eqs. (2), (7), (8), and (10) with the parameters ε_L, γ, m, n, and N, which are typical for Bi crystals, in comparison with optical functions corresponding to the classical (purely plasma) dielectric Drude function

$$\varepsilon_{\text{Drude}}(\omega, \gamma) = \varepsilon_L\left(1 - \frac{\omega_p^2}{\omega(\omega + i\gamma)}\right). \quad (11)$$

Expression (11) follows immediately from Eqs. (1) and (3) at $N = 0$.

LAYER MODEL

We consider a crystal containing layer microdefects (zone crystal) with concentration N_w. The distribution in each layer has the form

$$P(x) = \Delta N \exp\left(-\frac{x^2}{s^2}\right), \quad (12)$$

where ΔN is the impurity density at the layer center, s is the mean layer thickness, and x is the distance from the layer center.

Calculating the Fourier transform of the charge distribution in a layer in accordance with Eq. (12) and integrating with respect to the angles in Eq. (3), we obtain

$$F(\omega, \gamma) = \frac{\varepsilon_L \omega_p^2}{6\pi^2 n}\int dk \left(k^2 + 6\pi^2 n N_w \left(\frac{\Delta N}{n}\right)^2 s^2 \exp\left(-\frac{k^2 s^2}{2}\right)\right)\left(\frac{1}{\varepsilon(k, \omega, \gamma)} - \frac{1}{\varepsilon(k, 0, \gamma)}\right). \quad (13)$$

The optical functions calculated for the zone crystal are presented in Fig. 3.

MODEL OF ION PAIRS

For a crystal containing defects in the form of a pair of ions spaced by the distance R, the Fourier transform of the charge distribution has the form

$$|q_f(k)|^2 = 2e^2\left(1 + \frac{\sin kR}{kR}\right). \quad (14)$$

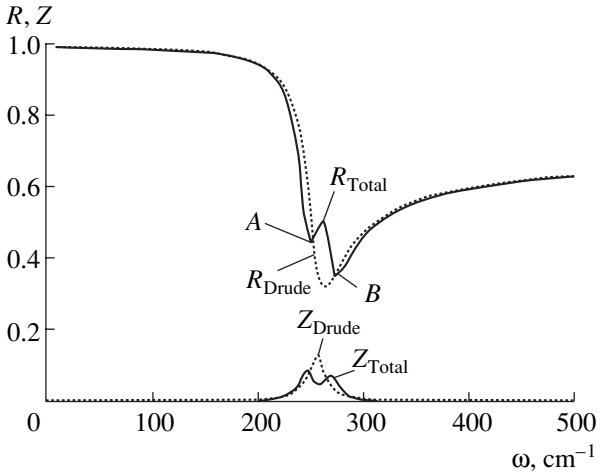

Fig. 2. Reflectivity R and dielectric-loss function Z that take into account the interaction of IR radiation in the range of plasma effects with cluster defects. The parameters are $n = 10^{24}$ m^3, $m^* = 0.031$, $\varepsilon_L = 100$, $S = 4 \times 10^{-7}$ m, $N_c = 10^{18}$ m^{-3}, and $\Delta N = 10^{24}$ m^{-3}.

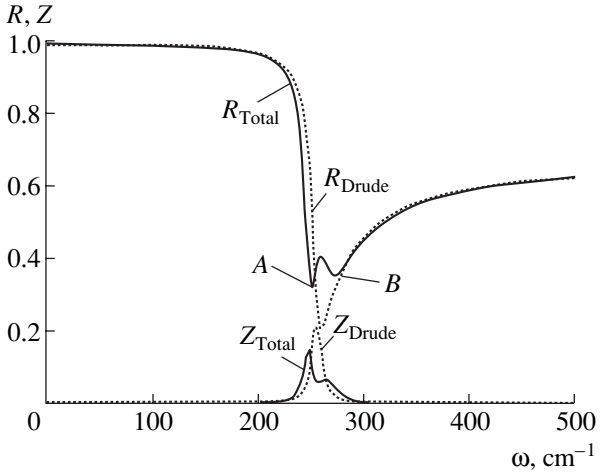

Fig. 3. The same as in Fig. 2, but for layer defects. The parameters differing from Fig. 2 are, $S = 10^{-7}$ m and $N_w = 10^6$ m^{-1} (instead of N_c).

After integration with respect to the angles in Eq. (3), we find

$$F(\omega, \gamma) = \frac{\varepsilon_L \omega_p^2}{6\pi^2 n}\int dk k^2 \left(1 + \frac{\sin(kR)}{kR}\right)\left(\frac{1}{\varepsilon(k, \omega, \gamma)} - \frac{1}{\varepsilon(k, 0, \gamma)}\right). \quad (15)$$

Note that the frequency dependences of the reflectivity $R(\omega)$ and dielectric loss function $Z(\omega)$ for defects in the form of a pair of ions are close to the respective dependences in the Drude model. However, the dependence $Y(\omega)$ also makes it possible to identify defects of this type.

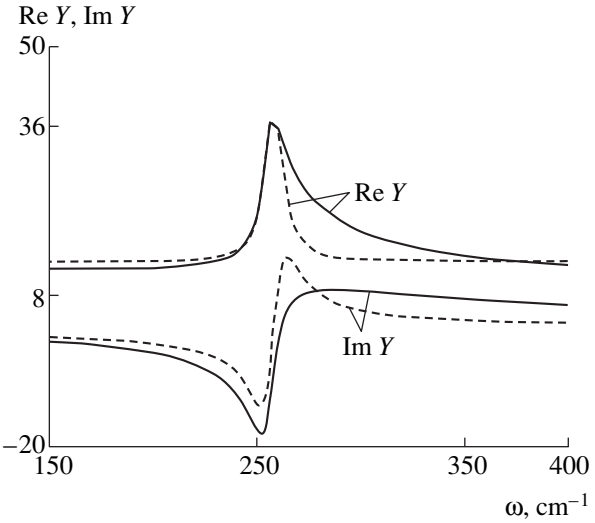

Fig. 4. Real and imaginary parts of the attenuation coefficient in the range of plasma effects for (solid line) layer defects and (dashed line) cluster defects.

As is seen in Figs. 2 and 3, the positions and shapes of the additional peaks are determined by the type, concentration, and linear sizes of defects. As is seen in Fig. 2 (3), the left boundary *A* of the additional peak is higher (lower) than the right boundary *B* for ion cluster defects (for ion layer defects, as well as for Bi crystals). However, their relative position depends generally on ε_L. Similarly, the plots of the attenuation coefficients $Y(\omega)$ and dielectric-loss functions $Z(\omega)$ are different for the above-described defects.

Comparing the spectra calculated for the reflectivity (Figs. 2 and 3) with experimental data (Fig. 1), we conclude that the features observed are not accidental. For example, the additional peak at the plasma frequency in the spectrum shown by curve *1* in Fig. 1 is associated with cluster defects (Fig. 2), while the features in the spectra shown by curves *4* and *5* in Fig. 1 testify to the presence of layer defects in the crystal (Fig. 3). The complex structure of the plasma minimum for the sample (Fig. 1, curves *2* and *3*) is determined by a combination of several types of defects.

The appearance of the additional peak near the plasma frequency is explained by the excitation of longitudinal plasmons of charge inhomogeneity, which shield the defects under the action of the electric field of the incident transverse electromagnetic wave [13]. These plasmons are characterized by a proper relaxation time whose frequency dependence [15] is resonant (Fig. 4).

Longitudinal plasmons can exist only in a narrow frequency range [7] and decay to single-particle excitations at higher frequencies. With increasing temperature, the additional plasma peak decreases due to the extension of the single-particle region and becomes invisible at room temperature (300 K). In this case, the reflectance spectra of crystals can be described by the Drude model for transverse plasmons. This temperature dependence is not typical of interband transitions.

Thus, the optical functions $R(\omega)$, $Z(\omega)$, and $Y(\omega)$ are explained by a dynamic model of $\varepsilon(\omega)$, which takes into account the effects of defect shielding. Therefore, by studying the behavior of the reflectance spectrum of a crystal, it is possible to investigate the fine-structure features of the crystal, for example, to determine the type, concentration, sizes, and volume distribution of defects, as well as the quality of doping.

ACKNOWLEDGMENTS

This work was supported by the Russian Foundation for Basic Research, project no. 00-15-98485.

REFERENCES

1. M. I. Belovolov, V. S. Vavilov, V. D. Egorov, and V. D. Kulakovskiĭ, Izv. Vyssh. Uchebn. Zaved. Fiz. **2**, 5 (1976).
2. V. M. Grabov, N. P. Stepanov, B. E. Wolf, and A. S. Mal'tsev, Opt. Spektrosk. **69** (1), 134 (1990) [Opt. Spectrosc. **69**, 82 (1990)].
3. T. M. Lifshits, A. B. Ormont, E. G. Chirkova, and A. Ya. Shul'man, Zh. Éksp. Teor. Fiz. **72** (3), 1130 (1977) [Sov. Phys. JETP **45**, 591 (1977)].
4. A. S. Mal'tsev, V. M. Grabov, and A. A. Kukharskiĭ, Opt. Spektrosk. **58**, 927 (1985) [Opt. Spectrosc. **58**, 567 (1985)].
5. A. S. Mal'tsev, S. A. Troshev, and V. A. Petrovsky, Syktyvkarskiĭ Mineralogicheskiĭ Sbornik, No. 28, 106 (1999).
6. A. S. Mal'tsev, V. A. Petrovsky, and S. A. Troshev, Syktyvkarskiĭ Mineralogicheskiĭ Sbornik, No. 26, 93 (1997).
7. D. Pines, *Elementary Excitations in Solids* (Benjamin, New York, 1963; Mir, Moscow, 1965).
8. Yu. T. Levitskiĭ and V. I. Palazhchenko, Neorg. Mater. **36** (7), 802 (2000).
9. E. Gerlach and M. Rautenberg, Phys. Status Solidi B **65**, 13 (1974).
10. E. Gerlach and M. Rautenberg, Phys. Status Solidi B **67**, 519 (1975).
11. E. Gerlach, P. Grosse, M. Rautenberg, and W. Senske, Phys. Status Solidi B **75**, 553 (1976).
12. E. Gerlach and S. Kistinger, Phys. Status Solidi B **151**, 241 (1989).
13. A. S. Mal'tsev and V. M. Grabov, *Physics of Solids* (Altaĭskiĭ Gosudarstvennyĭ Pedagogicheskiĭ Inst., Barnaul, 1990).
14. A. S. Mal'tsev, V. M. Grabov, and V. A. Petrovsky, *Mineralogical Crystallography and Crystallogeneses* (Inst. of Geology Akad. Nauk SSSR, Syktyvkar, 1990), pp. 59–60.
15. A. S. Mal'tsev, S. A. Troshev, V. A. Petrovsky, and A. E. Sukharev, Syktyvkarskiĭ Mineralogicheskiĭ Sbornik, No. 31, 155 (2001).

Translated by Yu. Vishnyakov

Doklady Physics, Vol. 47, No. 11, 2002, pp. 819–821. Translated from Doklady Akademii Nauk, Vol. 387, No. 3, 2002, pp. 326–328.

PHYSICS

The Effect of Temperature Gradient on Kinetics of the Surface-Oxidation Process

Corresponding Member of the RAS P. K. Khabibullaev, D. T. Alimov, and S. A. Ubaĭdullaev

Received February 27, 2002

In this paper, the results of investigations in the kinetics of the metal-surface oxidation process when heating by laser radiation are presented. It is found that a decrease in the copper oxidation rate occurs at temperatures $T < 250$–300°C on the surface facing the laser radiation as compared to the non-illuminated opposite side. At temperatures $T > 300$°C, the decrease in the oxidation rate on the overheated surface is not observed. As was previously predicted, these features of the oxidation kinetics are governed by the thermoelectromotive-force mechanism of diffusive mass transfer, which is explained by the existence of a high temperature gradient in the surface-oxide layer.

In the case of a solid subjected to laser heating, the observed physical pattern of the oxidation process has a number of specific features that are caused by an inhomogeneous temperature-field distribution over both the target surface and thickness [1–3].

As was previously shown by us in [4–6] for the case of laser heating, high temperature gradients arise in the oxide film, an effect which leads to the appearance of the internal thermoelectromotive force. It is also well known (see [7–9]) that high-temperature oxidation of various metals is accompanied by the movement of charged defects through the oxide layer. Therefore, the appearance of the electric field caused by the thermoelectromotive-force in the oxide layer results in the directed electric diffusion of reaction atomic components. In this case, either acceleration or retardation of the oxidation process takes place depending on the sign of the thermoelectromotive force [4].

In the present paper, we describe further investigations of the thermoelectromotive-force mechanism of copper-target oxidation in ambient air under different temperature conditions in which differences in the stoichiometric composition of oxides being formed arise. At relatively moderate temperatures $T < 250$–300°C in the course of the reaction of copper oxidation, the CuO oxide dominates in the phase composition of the oxides formed. At the same time, in the case of high-temperature oxidation, preferential growth of the Cu_2O oxide occurs [10]. In accordance with [11], these oxides must possess opposite signs of the thermoelectromotive-force coefficient. It is evident that for different temperature ranges, we should expect a different contribution of the thermoelectromotive-force mechanism into the process of heterogeneous oxidation of copper.

DESCRIPTION OF THE EXPERIMENT

Copper samples 16 mm in diameter and 0.5 mm thick were used as targets. Heating was accomplished by the beam of a continuous-radiation CO_2 laser with a power of about 100 W. Two thermocouples were fixed to the back side of each target. One of them was located directly under the target frontal surface and measured the temperature of the surface being heated by the laser radiation. The other thermocouple determined the temperature of the rear surface.

The oxidation process was monitored according to the thickness of the oxide layer formed as a result of heating the surfaces of the copper targets. The oxide thickness was measured by an optical method using the interference maxima of the reflection of monochromatic light from the oxide-layer structure. Synchronous measurements of the oxide-layer thickness were performed on the frontal and rear target surfaces. Radiation from a pulse-periodic CO_2 laser with integral and peak powers of 0.1 W and up to 2–3 W was used as probing radiation. The diameter of the region illuminated by the probing radiation did not exceed 2–3 mm and was much smaller than the target diameter. This allowed local-thickness measurements at arbitrary target points to be performed.

EXPERIMENTAL RESULTS

The values of the light-reflection coefficient $R(t)$, which were determined as a function of time in the course of our experiments, are presented in Fig. 1. The oxide thickness could be unambiguously determined by virtue of the fact that positions of the interference absorption maxima were associated with the optical

Department of Thermal Physics,
Academy of Sciences of Uzbekistan,
Katartal 28, kvartal Ts, Chilanzar, Tashkent,
700135 Uzbekistan

1028-3358/02/4711-0819$22.00

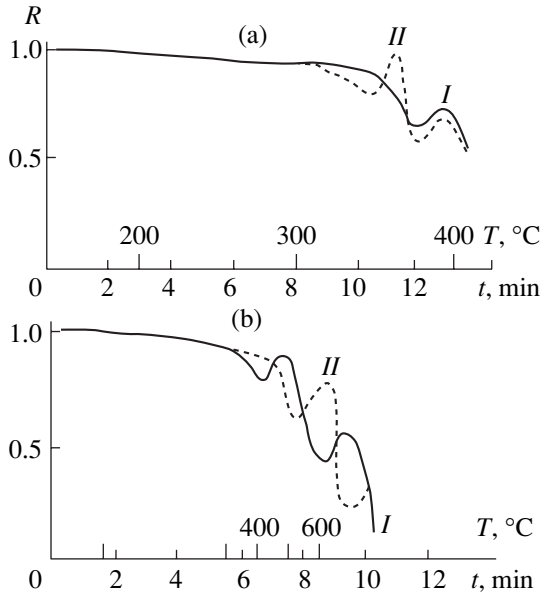

Fig. 1. The effect of the complicated copper oxide structure on the time dependence of the reflection coefficient for monochromatic light with the wavelength $\lambda = 10.6$ μm: (*I*) target frontal surface and (*II*) target rear surface. (a) $m_1 = 3.3$ g; $P = 100$ W; beam diameter $D \sim 15$ mm; target thickness $h_1 = 1.5$ mm and (b) $m_2 = 2.5$ g; $P = 100$ W; beam diameter $D \sim 15$ mm; target thickness $h_2 = 0.7$ mm.

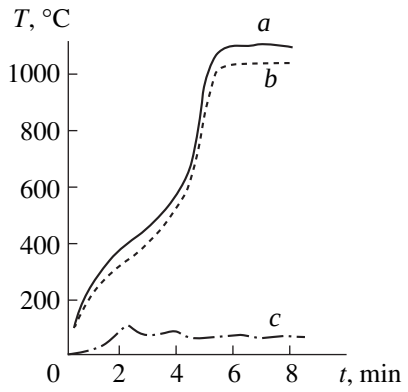

Fig. 2. Heat dynamics in heating copper targets: (*a*) frontal surface, (*b*) rear surface; and (*c*) absolute temperature difference between the frontal and rear surfaces.

thickness I by the relation $I = k_i \frac{\lambda}{2n}$, where λ is the radiation wavelength, n is the refractivity index, and k_i is the interference order. Inasmuch as we were interested, in the present experiment, only in relative measurements of the thickness, the temperature dependence $n(T)$ was ignored in our calculations.

The experiments were performed with targets of various masses. This made it possible to observe the oxidation process under conditions of different thermal dynamics of heating without a variation of heating-radiation parameters. Thereby, we managed to carry out experiments with oxides having a given stoichiometric composition. For each oxide type, the absolute value and the sign of the thermoelectromotive force were determined. In order to do this, CuO and Cu_2O oxides were separated by etching with selective chemical etching reagents [8]. Polycrystal fractions of CuO and Cu_2O oxides obtained as a result of this separation were used in preparing samples for thermoelectromotive-force measurements. It is worth mentioning that, in the case of a massive target ($m_1 = 3.3$ g), the heating rate was low. Therefore, the oxide formation preferentially occurred at relatively moderate temperatures $T < 300$°C. For a light target ($m_2 = 2.6$ g), a higher heating rate was observed, and target oxidation preferentially proceeded at higher temperatures $T > 300$°C. In all cases, the temperature of the frontal surface exceeded that of the rear one (Fig. 2). Curve *b* in Fig. 2 shows the absolute difference of temperatures on the frontal and rear target surfaces. The experimental data concerning the values and sign of the thermoelectromotive force for CuO and Cu_2O oxides exhibit complete consistency with the results of [8]. For example, in the case of CuO, $\varepsilon \sim -500$ μV/°C at $T \sim 200$°C, whereas for Cu_2O, $\varepsilon \sim -450$ μV/°C at $T \sim 600$°C.

In order to estimate the contribution of thermoelectromotive-force waves into the diffusion process, we consider the expression for the total diffusion flux [3]:

$$j_D = -DN\left[\nabla C + \delta C\left(\frac{\nabla T}{T}\right)\right]. \quad (1)$$

Here, $\delta = \alpha + \gamma$ (α is the thermodiffusion constant and $\gamma = \frac{|q|\varepsilon}{k_D}$ is the electrodiffusion constant).

In solving the diffusion problem, we use conditions of the quasi-steadiness for both the mass-transfer and heat-transfer processes, namely, $\nabla j_D = 0$ and $\nabla j_T = 0$, respectively. Thus, we arrive at the expression describing the kinetic law adequate to the given conditions:

$$\frac{dx}{dt} = \frac{D(T)}{xf(\alpha, \gamma, I)}. \quad (2)$$

Here, $f(\alpha, \gamma, I) = \left\{1 - \frac{\alpha - \gamma}{1 + \alpha - \gamma}\frac{x}{kT}\right\}$, I is the radiation intensity; k is the oxide heat-conduction coefficient; T is the temperature of the target; and x is the oxide thickness.

The function $f(\alpha, \gamma, I)$ can be written in the form

$$f(\alpha, \gamma, I) = \left\{1 - \frac{x}{kT}I + \frac{1}{1 + \alpha - \gamma}\frac{x}{kT}I\right\}. \quad (3)$$

If, in expression (3), the quantity $(1 + \alpha - \gamma) < 1$, then in the case of $x \ll x_0 = \frac{k_0 T}{I}$, $k \sim 0.01$ W/(cm^2 °C), $T = 10^3$,

$I = 10^2$, we may ignore the second term. In this case,

$$f(\alpha, \gamma, I) = 1 \pm \Delta I. \quad (4)$$

Here, the plus and minus signs correspond to positive and negative values of the thermoelectromotive-force coefficient.

As expressions (2) and (4) show, regimes of an increase or a decrease in the oxidation rate as compared to the isothermal oxidation rate (proportional to $\sim\frac{D}{x}$) are realized in the following cases. (a) If $(1 + \alpha - \gamma) < 1$, both an increase and a decrease are possible; and (b) if $(1 + \alpha - \gamma) > 1$, only a decrease is possible.

Thus, the results of this work demonstrate intrinsic features of the kinetics of the heterogeneous oxidation reaction, which are associated with a variation in the stoichiometric composition of an oxide being formed when the diffusion mass transfer is governed by the thermoelectromotive-force mechanism.

REFERENCES

1. N. V. Karlov, N. A. Kirichenko, and B. S. Luk'yanchuk, *Laser Thermochemistry* (CISP, 1999).
2. V. A. Bobyrev, F. V. Bunkin, B. S. Luk'yanchuk, *et al.*, Poverkhnost **4**, 134 (1984).
3. O. G. Buzykin and A. V. Burmistrov, Poverkhnost **10**, 91 (1983).
4. D. T. Alimov, V. A. Bobyrev, F. V. Bunkin, *et al.*, Dokl. Akad. Nauk SSSR **268**, 850 (1983) [Sov. Phys. Dokl. **28**, 150 (1983)].
5. D. T. Alimov, B. S. Luk'yanchuk, A. I. Omel'chenko, and P. K. Khabibullaev, Fiz. Khim. Obrab. Mater. **1**, 50 (1988).
6. D. T. Alimov, Yu. N. Mitin, V. K. Tyugaĭ, and P. K. Khabibullaev, Poverkhnost **4**, 126 (1985).
7. A. A. Vedenov and G. G. Gladush, *Physical Processes in Laser Treatment of Materials* (Énergoatomizdat, Moscow, 1985).
8. P. Kofstad, *High-Temperature Oxidation of Metals* (Wiley, New York, 1966; Mir, Moscow, 1969).
9. A. P. Menushenkov and V. N. Nevolin, *Lazer Technology* (Mosk. Inzh.-Fiz. Inst., Moscow, 1992), Part 1.
10. O. Kubaschewski and B. E. Hopkins, *Oxidation of Metals and Alloys* (Butterworths, London, 1962; Metallurgiya, Moscow, 1965).
11. M. Skuratov, V. P. Kolesov, and V. A. Vorob'eva, *Thermochemistry* (Moscow, 1964), Part 1.

Translated by G. Merzon

Doklady Physics, Vol. 47, No. 11, 2002, pp. 822–824. Translated from Doklady Akademii Nauk, Vol. 387, No. 3, 2002, pp. 329–332.

TECHNICAL PHYSICS

Deformability of Particle-Filled Composites at Brittle Fracture

O. A. Serenko, G. P. Goncharuk, and S. L. Bazhenov

Presented by Academician N.F. Bakeev April 8, 2002

Received April 19, 2002

Strain at the brittle rupture of rubber-particle-filled composites based on polymeric matrices deformed via the neck propagation was found to be equal to the value for the onset of the neck propagation in the initial matrix polymer. This characteristic is important for particle-filled composites, because it determines their ultimate elongation at brittle fracture.

Conventionally, caoutchouc particles are introduced into brittle polymers, for example, polystyrene, to increase their shock viscosity and deformability [1]. However, the introduction of caoutchouc or rubber particles into a plastic polymer reduces its ultimate strain [2, 3]. For a certain critical filler content, the composite becomes brittle, more precisely, quasibrittle, which is accompanied by a sharp decrease in the rupture strain by a factor of about 100 [3]. The translation from plastic to brittle fracture of the composite occurs because the formed neck loses its capability to propagate along the sample with a certain content of particles, and it ruptures during the neck formation [4, 5].

Translation to brittle fracture occurs when the initial matrix is deformed via the neck propagation [4, 5]. Otherwise, the introduction of a filler into the polymer only monotonically reduces rupture strain in a wide interval of compositions [6]. Brittle fracture is observed in a narrow range of filling degree that is determined by the type of the matrix and by the capability of the matrix for strain hardening [3]. The typical interval of the brittle behavior of a composite containing a hard mineral or elastic particles lies from 10 to 40 vol % of filler. For higher contents of rubber particles, the next translation occurs from the brittle fracture to the homogeneous plastic deformation and is accompanied by an increase in the rupture strain of the filled polymer [7]. The purpose of this study is to investigate the deformability of composites consisting of polyethylene matrices and rubber particles in the region of quasibrittle behavior.

Institute of Synthetic Polymeric Materials, Russian Academy of Sciences, ul. Profsoyuznaya 70, Moscow, 117393 Russia

To prepare composite materials, we used low-density polyethylene (LDPE), medium-density polyethylene (MDPE), their mixtures, and mixtures of LDPE and high-density polyethylene (HDPE). The brands and properties of the polymers, as well as the properties of polyethylene mixtures, are presented in the table. We used a polydisperse rubber crumb with a particle size ranging from 0.05 to 0.6 mm as a filler and varied the filling degree from 0 to 36 vol %.

The composites were prepared by mixing in a single-screw laboratory extruder. Then, 2-mm plates were formed by pressing the mixtures at a temperature of 160°C and a pressure of 10 MPa and were cooled to 20°C under pressure. From the plates, we cut samples in the form of a two-sided paddle with a 5×35-mm working area.

The mechanical tests of the composites were carried out on a Shimadzu Autograph AGS-10 kNG universal testing machine and on a 2038R-005 dynamometer at room temperature and a tension rate of 20 mm/min. The sample surface was studied by a computerized optical microscope $Q \times 3$.

All the polymeric matrices being investigated were deformed with the formation of a neck. Figure 1 shows typical stress–strain curves for filled polymers with various contents of rubber particles. For a low filler content, the composite ruptures as the neck propagates across the working area of the sample (curve *2*). As the filling degree increases, the plastic deformation of the composite changes to brittle, more precisely to quasibrittle, fracture (curve *3*). The material ruptures when the neck is formed. Further filling leads to the disappearance of the sharp yield point in the stress–strain diagram of the composite (curve *4*).

Figure 2 shows the typical appearance of the ruptured material containing 36 vol % of rubber particles. In the rupture plane of the sample, we observe a contraction associated with neck formation.

Figure 3 shows the most characteristic dependences of rupture strain ε_c for the composites being investigated on rubber-particle content V_f. The introduction of a small amount of rubber particles (1.6 vol %) substantially reduces material deformability due to the large

1028-3358/02/4711-0822$22.00

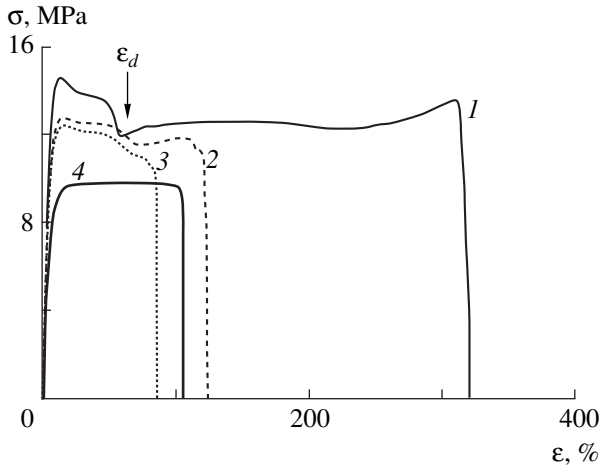

Fig. 1. Stress–strain curves of the composites based on matrix no. 9 from the table. The content of an elastic filler is (*1*) 0, (*2*) 6, (*3*) 9, and (*4*) 26 vol %. The arrow indicates the neck-formation strain ε_d in the matrix polymer.

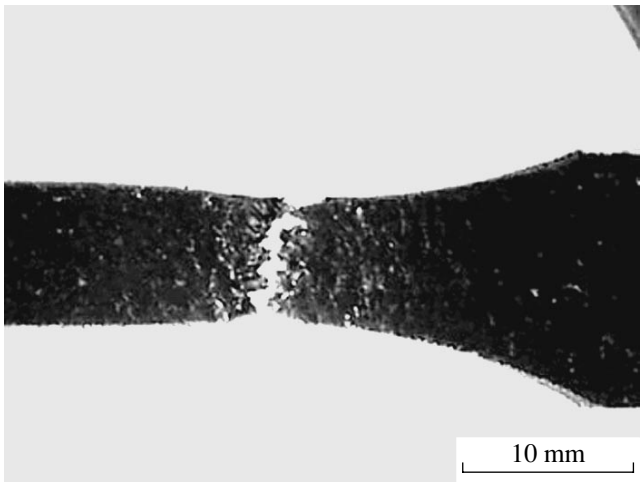

Fig. 2. Appearance of the fractured sample of the composite based on matrix no. 9 from the table and containing 36 vol % of an elastic filler.

size (up to 0.6 mm) of particles of the polydisperse elastic filler. The filling of the polymers under investigation with a monodisperse elastic filler of smaller particles increases rupture strains in the composites for low degrees of filling but does not affect the deformation mechanism and the general form of ε_c as a function of V_f. The filled polymer is deformed via the formation and propagation of a neck. For a certain filler content, the material loses deformability and ruptures as the neck is formed. With the further increase in V_f, the ultimate elongation of the composite remains almost constant for the amounts of filling being investigated.

Deformability decreases sharply for a certain critical filler content, because the plastic behavior of the

Composition and properties of polymeric matrices (engineering magnitudes of stresses are given)

No.	Composition	Polymer brand	Upper yield point σ_y, MPa	Neck-propagation stress σ_d, MPa	Neck-formation strain ε_d, %	Strength σ_c, MPa	Ultimate strain ε_c, %
1	LDPE	16803-070	8.0	7.8	70	12.7	550
2	LDPE	15803-020	10.2	10.0	86	16.7	600
3	95 wt % LDPE + 5 wt % HDPE	15803-020 + 277-73	8.9	8.7	90	11.8	380
4	90 wt % LDPE + 10 wt % HDPE	″	9.3	9.0	77	11.5	360
5	85 wt % LDPE + 15 wt % HDPE	″	9.3	8.8	76	10.2	340
6	75 wt % LDPE + 25 wt % HDPE	″	10.1	9.5	60	10.9	320
7	70 wt % LDPE + 30 wt % HDPE	″	11.4	9.8	53	11.8	340
8	HDPE	F 3802 B	21.3	15.5	27	26.5	720
9	70 wt % LDPE + 30 wt % HDPE	15803-020 + F 3802B	14.7	12.1	60	14.3	450
10	LDPE	16204-020	11.0	10.6	100	16.8	600
11	80 wt % LDPE + 20 wt % HDPE	16204-020 + 277-73	13.7	11.6	70	15.6	520
12	70 wt % LDPE + 30 wt % HDPE	″	16.4	12.5	35	15.8	510

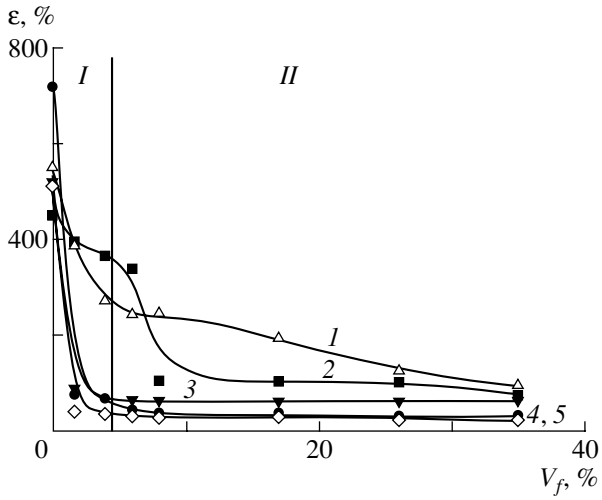

Fig. 3. Ultimate strain in composites based on matrices (*1*) no. 1, (*2*) no. 9, (*3*) no. 11, (*4*) no. 12, and (*5*) no. 8 (numbers according to table). Intervals *I* and *II* correspond to the plastic deformation and brittle rupture of the materials, respectively.

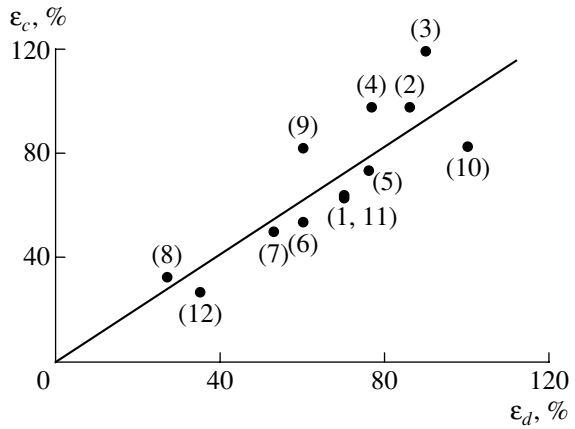

Fig. 4. Ultimate strain in composites at brittle fracture vs. the neck-formation strain in the matrix polymers, whose numbers according to the table are given in the parentheses.

composite (interval *I*, Fig. 3) changes to brittle fracture (interval *II*, Fig. 3) [3]. The critical filling for this change in the deformation mechanism depends on both the reinforcement degree [3, 4] and the elongation degree of the matrix-polymer neck.

The ultimate elongation at brittle rupture (interval *II*, Fig. 3) is virtually independent of the filler content but varies for various matrix polymers. All the composites in this region of compositions rupture in the process of neck formation before its propagation along the sample. Figure 4 shows the correlation between the rupture strain ε_c of the composite at brittle fracture and the strain ε_d at the onset of neck propagation in the initial matrix polymer. The latter value is denoted by the arrow in Fig. 1. The dependence shown in Fig. 4 is linear and has a slope close to 45°. Consequently, the rupture strain ε_c of the composite is equal to the strain ε_d at the onset of neck propagation in the initial matrix polymer:

$$\varepsilon_c = \varepsilon_d.$$

This correlation explains why the brittle rupture of various composites occurs at different ultimate elongations. The brittle rupture of a composite based on a matrix polymer where the neck is formed for low (high) strains as, for example, in MDPE (LDPE) occurs at low (high) ultimate elongation.

Thus, the strain at the onset of neck propagation is an important characteristic of the material and determines the deformability of filled composite systems at brittle fracture.

REFERENCES

1. C. B. Bucknall, *Toughened Plastics* (Applied Science Publishers Ltd., London, 1977; Khimiya, Leningrad, 1981).
2. N. A. Erina, S. G. Karpova, O. A. Ledneva, *et al.*, Vysokomol. Soedin., Ser. B **37** (8), 1392 (1995).
3. O. A. Serenko, V. S. Avinkin, and S. L. Bazhenov, Vysokomol. Soedin., Ser. A **44** (8), 457 (2002).
4. S. Bazhenov, Polym. Eng. Sci. **35** (10), 813 (1995).
5. Al. Al. Berlin, V. A. Topolkaraev, and S. L. Bazhenov, *Physical Aspects of Production of Failure and Deformation, Collection of Scientific Works* (Fiziko-Tekhnicheskiĭ Inst., Leningrad, 1987).
6. S. L. Bazhenov, V. S. Avinkin, and O. A. Serenko, Dokl. Akad. Nauk **382** (3), 341 (2002) [Dokl. Phys. **47**, 72 (2002)].
7. S. L. Bazhenov, G. P. Goncharuk, and O. A. Serenko, Dokl. Akad. Nauk **379** (5), 620 (2001) [Dokl. Phys. **46**, 562 (2001)].

Translated by V. Bukhanov

Doklady Physics, Vol. 47, No. 11, 2002, pp. 825–827. Translated from Doklady Akademii Nauk, Vol. 387, No. 2, 2002, pp. 196–199.

MECHANICS

On Trajectories of Earth–Moon Flight of a Particle with Its Temporary Capture by the Moon

V. V. Ivashkin

Presented by Academician T.M. Éneev April 10, 2002

Received April 15, 2002

Studies of the characteristics of a space flight from the Earth to the Moon are of importance for both astronautics and celestial mechanics. A valuable contribution to analysis of this problem was made by Egorov (see [1] and references therein). In his papers, a fundamental investigation of the Earth–Moon–particle system was performed for trajectories of a direct flight to the Moon within the Earth's sphere of influence with respect to the Sun. Trajectories of this class were used in virtually all flights of space vehicles to the Moon. These trajectories are distinguished by a short (several days) flight time and by the fact that the approach to the Moon occurs along a hyperbola. Recently (see, e.g., [2–6]), a new class of trajectories appropriate for a flight to the Moon was revealed in the Earth–Sun–Moon–particle system. These trajectories initially correspond to flight in the direction of the Sun (or from the Sun) beyond the boundary of the Earth's sphere of influence and, only afterwards, to flight to the Moon (Fig. 1). We below call these flights and trajectories "bypass" ones. The bypass flights are somewhat similar to the three-impulse bielliptic flights proposed by Sternfeld in [7, 8]. However, from the dynamic standpoint, the former trajectories differ from the latter ones. In contrast to bielliptic flights, the perigee rise now is realized, not due to the expense of the velocity increase in a remote apogee, but owing to solar gravitation. In addition, a particle now approaches the Moon along an ellipse, i.e., is captured by the Moon. Therefore, for the transition of a space vehicle into a Moon-satellite orbit or for landing, such bypass flights are more efficient than direct and bielliptic ones. It is also important to reveal the conditions of the formation and realization of these trajectories, in particular, the particle capture mechanism. In this paper, we present the results of analysis of effects produced by solar and terrestrial disturbances on the motion of a particle in the Earth–Sun–Moon system, which can promote the discovery the mechanism of the particle capture by the Moon. The results of investigating characteristics of the new trajectories for flights from the Earth to the Moon are also presented.

First, we estimate the effect of the Sun on the change in the perigee distance r_π of the particle orbit. We apply the method developed by Lidov [9] of analysis of planet-satellite orbit evolution under the action of an external body. For an immobile Sun, the major semiaxis of a space vehicle is constant. Assuming the orbit eccentricity $e \approx 1$ (initial distance in the perigee is small, $\Delta r_\pi \gg r_{\pi 0}$) and taking for r_π its average value $r_\pi =$

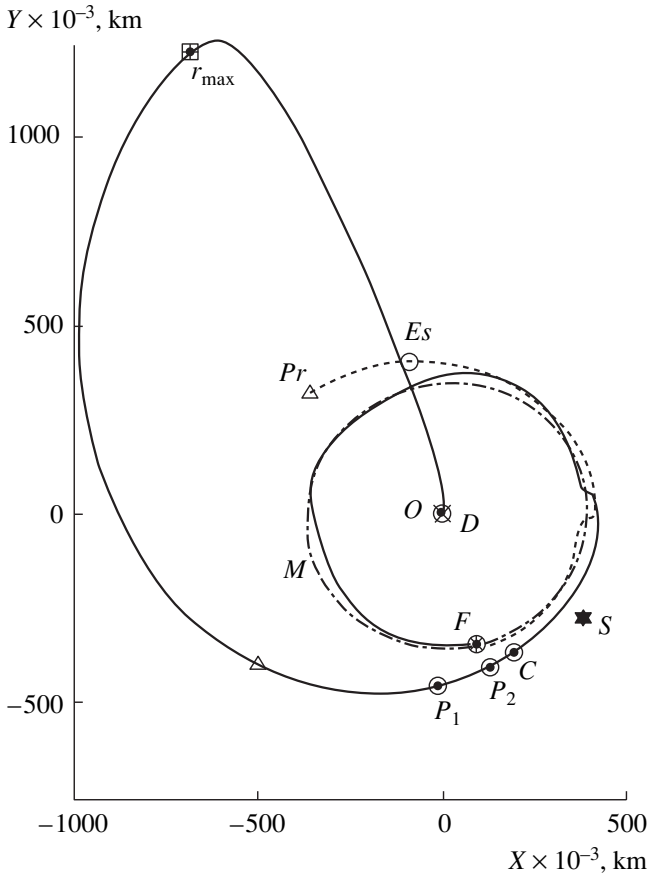

Fig. 1. Geocentric trajectory of a flight from the Earth to the Moon and the passive continuation of the trajectory beyond the final point.

Keldysh Institute of Applied Mechanics, Russian Academy of Sciences, Miusskaya pl. 4, Moscow, 125047 Russia

1028-3358/02/4711-0825$22.00

$\frac{2r_{\pi 0} + \Delta r_\pi}{2} \approx \frac{\Delta r_\pi}{2}$, we obtain the variation of the perigee distance

$$\Delta r_\pi \approx \operatorname{sgn}\beta\left(\frac{15}{2}\pi\frac{\mu_S}{\mu_E}\beta\right)^2\frac{a^7}{r_B^6} > 0. \quad (1)$$

Here, μ_E and μ_S are the gravitational parameters of the Earth and Sun; $\beta = \cos^2\gamma \sin 2\alpha$, γ is the inclination angle for the radius vector $\mathbf{r}_B$ of an external body (in this case, the Sun) to the plane of the mass-point orbit; α is the angle between the projection onto this plane of the radius vector and the direction to the perigee; and $r_B = |\mathbf{r}_B|$. For $\Delta r_\pi > 0$, we must have $\sin 2\alpha > 0$, $0 < \alpha < \frac{\pi}{2}$ or $\pi < \alpha < \frac{3\pi}{2}$.

We now estimate the necessary value of the major semiaxis of the space-vehicle orbit:

$$a \approx \left[\frac{\Delta r_\pi r_B^6}{\left(\frac{15}{2}\pi\frac{\mu_S}{\mu_E}\beta\right)^2}\right]^{1/7}. \quad (2)$$

We assume that $\Delta r_\pi = 500000$ km and $\beta = 0.5$. In this case, $a \approx 0.87 \times 10^6$ km and $r_\alpha \approx 1.5 \times 10^6$ km. Allowance for the variation of the direction to the Sun slightly changes the results obtained. Thus, flying away for a distance of $\sim 1.5 \times 10^6$ km and for the suitable orientation of the Sun direction results in the rise of the particle orbit perigee outside of the lunar orbit.

Now, suppose the mass point in its flight to the lunar orbit approaches the Moon and has with respect to it the radius vector $\boldsymbol{\rho}$, the velocity vector $\mathbf{V}$, and the mechanical energy $E = \frac{\mathbf{V}^2}{2} - \frac{\mu_M}{\rho} > 0$, where $\rho = |\boldsymbol{\rho}|$ and μ_M is the gravitational parameter of the Moon. In order to analyze the possibility of reducing this energy by the Earth, we consider a model of the particle motion to the Moon along a straight line, $\frac{d\rho}{dt} < 0$, the Earth being located beyond the Moon in the same straight line. In this case, the Earth's perturbation damps the particle motion. Assuming the distance between the Earth and the Moon to be invariable, $r_M = \text{const}$, we find for the perturbed particle motion the dependence of its energy on the distance and the distance ρ_C corresponding to the capture:

$$E = \frac{\mu_E}{r_M^2}(\rho - \rho_C) + \frac{\mu_E}{r_M + \rho} - \frac{\mu_E}{r_M + \rho_C}, \quad E(\rho_C) = 0,$$

$$\rho_C = \frac{B}{2} + \left(\frac{B^2}{4} + r_M B\right)^{1/2}, \quad (3)$$

$$B = \rho - r_M\left(1 + E\frac{r_M}{\mu_E} - \frac{r_M}{r_M + \rho}\right).$$

Example. In the onset of the approach, let the energy of the particle be $E = 0.08$ km^2 s^{-2}; the velocity at infinity is $V_\infty = 0.4$ km s^{-1}, $\rho = 160000$ km, and $r_M = 390000$ km. In this case, relationship (3) yields $\rho_C \sim 90000$ km. Thus, for these flights, the gravitation of the Earth allows the damping of the particle hyperbolic velocity with respect to the Moon and realization of the particle capture by the Moon near the translunar libration point l_2.

We now estimate the effect of the Earth's gravitation on a decrease in the selenocentric energy ΔE of the particle motion from zero to a negative value for a finite elliptic orbit. To this aim, we use the evolution theory [9]. Assuming $e \sim 1$, the average energy $E \sim \Delta E/2$, and taking into account a change in the Moon–Earth direction, we arrive at

$$\Delta E \approx \operatorname{sgn}\beta\left(\frac{15}{2}\pi\mu_E\left(\frac{\mu_M}{r_M}\right)^3 n_M|\beta|\right)^{2/9} < 0. \quad (4)$$

Here, n_M is the angular velocity of the orbital lunar motion and β is determined by the Earth as an external body. Evaluating by formula (4) yields $\Delta E \sim -0.09$ km^2 s^{-2} for $\beta = 0.5$. Thus, the gravitation of the Earth (in the case of its appropriate orientation) noticeably decreases the particle energy and leads to the strongly elongated elliptic orbit of the lunar satellite. It is worth noting (similarly to [3]) that, as distinct to estimate (1), where the perigee rose, now in expression (4), $\sin 2\alpha < 0$.

Reviewing the results of the given analysis, we can see that there exists a fundamental possibility for the realization of a bypass flight from the Earth to the Moon, which is accompanied by the capture of a particle by the Moon into an elongated elliptic orbit. The results of numerical calculations presented in [2–6] of such trajectories confirm this conclusion and the estimates obtained.

In the numerical analysis, we determine space-vehicle trajectories by integrating (using the method of [10]) equations of motion of a particle in an nonrotating geoequatorial geocentric rectilinear *OXYZ* coordinate system. The integration was performed with allowance for the attraction field of the Earth (with the principal harmonic c_{20} taken into account), Moon, and Sun and with the determination of the coordinates of the Sun and of the Moon according to the DE403 JPL ephemerises. The motion of the particle was also determined in the selenocentric *MXYZ* coordinate system. As an example, we present characteristics for one of the bypass trajectories obtained by us. In Figs. 1–3, solid curves show the geocentric and selenocentric motions of a space vehicle from the Earth to the Moon, as well as the variation of the energy constant for the motion with respect to the Moon. The dashed–dotted line *M* in Fig. 1 shows the lunar orbit. A space vehicle flies away from the Earth ($r_{\pi 0} = 6578$ km, the point *D*) on December 20, 2000, covering in the time $\Delta t \sim 51$ days the distance $r_{\max} \approx 1.51 \times 10^6$ km. At this time, the direction to the Sun is determined by the point *S*. Here, the space vehicle receives a small velocity increment (~12 m s^{-1})

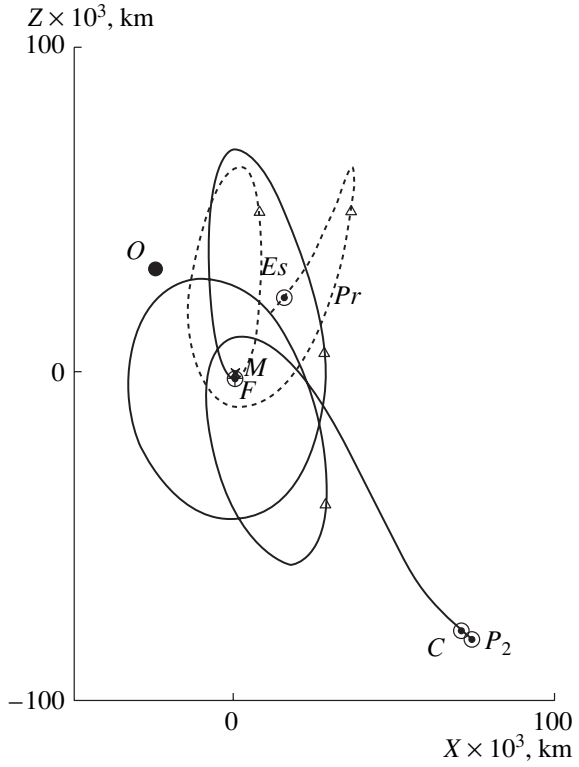

Fig. 2. Selenocentric trajectory of a flight from the Earth to the Moon at the final stage of motion, and the passive continuation of the trajectory beyond the final point.

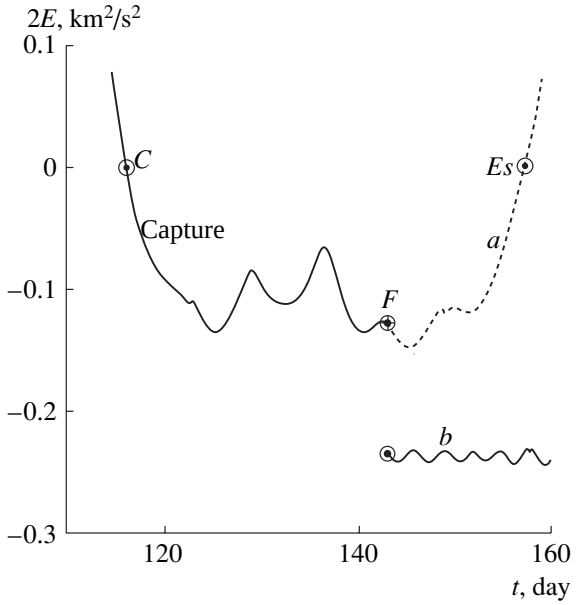

Fig. 3. Selenocentric energy constant as a function of time for capture of a particle by the Moon and for the continuation of motion beyond the final point: (*a*) passive flight through the final point and (*b*) application of an impulse for the velocity decrease.

to match positions of the space vehicle and the Moon before capture. Under the effect of the Sun, the perigee gradually rises up to ~514000 km, and the space vehicle approaches the Moon. For $\Delta t \sim 112.9$ days, the energy is $E \sim 0.08$ km^2 s^{-2}; the velocity is $V_\infty \sim 0.4$ km s^{-1}; and the distance to the Moon is $\rho \sim 160000$ km (P_1 point). For $\Delta t \sim 114.6$ days, $V_\infty \sim 0.2$ km s^{-1}; $\rho \sim 122000$ km (P_2 point). For $\Delta t \sim 115.4$ days, $E = 0$, $V_\infty = 0$, $\rho \sim 110000$ km; i.e., the capture occurs (*C* point). We can see a good qualitative correspondence between the actual motion and capture-model predictions according to formula (3). In Fig. 2, the point *O* indicates the direction to the Earth at the capture moment. Furthermore, the evolution of the circumlunar orbit occurs 142.4 days after the start, and ~27 days after capture, the final perilune *F* is attained. Here, for the osculating orbit, $E \sim -0.064$ km^2 s^{-2}, and distances in the pericenter and in the apocenter are, respectively, $r_{\pi f} = 1838$ km and $r_{\alpha f} = 75072$ km. Curve *b* in Fig. 3 corresponds to the continued motion of a space vehicle after a small retarding impulse (~23.54 m s^{-1}) has been applied at the final point *F* and after the corresponding lowering the apolune to 40000 km. In this case, the orbit remains elliptic. Dashed prolongation curves *Pr* in Figs. 1–3 correspond to the passive continuation of the motion beyond the final point *F* with no impulse applied. In 14.2 days, the space vehicle gets free of the lunar attraction (at the escape point *Es*). Here, $E = 0$, and we have a temporary capture of the particle.

ACKNOWLEDGMENTS

The author is grateful to Professor J.J. Martinez Garcia and Dr. Belló Mora for help in the study of this problem. They were the first to bring it to the author's attention. The author is also grateful to V.A. Stepan'yants and A.V. Chernov for their help in the development of the numerical algorithm.

This work was supported by the Russian Foundation for Basic Research, project no. 01-01-00133.

REFERENCES

1. V. A. Egorov, Usp. Fiz. Nauk **63**, 73 (1957).
2. J. K. Miller and E. A. Belbruno, in *Proceedings of the AAS/AIAA Spaceflight Mechanics Meeting, Houston*, AIAA Pap. **91**–**100**, 97 (1991). AAS Paper 91–100, pp. 97–109.
3. E. A. Belbruno and J. K. Miller, J. Guid. Cont. Dyn. **16**, 770 (1993).
4. R. Biesbroek and G. Janin, ESA Bull., No. 103, 92 (2000).
5. W. S. Koon, M. W. Lo, J. E. Marsden, and S. D. Ross, Celest. Mech. Dyn. Astron. **81**, 63 (2001).
6. V. V. Ivashkin, Preprint No. 85, IAM RAS (Inst. Prikl. Mat. Ross. Acad. Nauk, Moscow, 2001).
7. A. Sternfeld, C. R. Hebd, Comptes rendus de l'Academie des Sciences (Paris) **198**, 711 (1934).
8. A. Sternfeld, *Artificial Earth's Satellite* (Gos. Izd. Tekh. Teor. Lit., Moscow, 1956).
9. M. L. Lidov, Iskusstv. Sputniki Zemli, No. 8, 5 (1961).
10. V. A. Stepan'yants and D. V. L'vov, Mat. Model. **12** (6), 9 (2000).

Translated by G. Merzon

Doklady Physics, Vol. 47, No. 11, 2002, pp. 828–832. Translated from Doklady Akademii Nauk, Vol. 387, No. 3, 2002, pp. 333–337.

MECHANICS

Relation of Wave and Vibration Processes in the Strings of Pizzicato Musical Instruments with the Playing Style of a Performer

Yu. A. Dem'yanov* and A. A. Malashin

Presented by Academician E.I. Shemyakin June 17, 2002

Received June 20, 2002

The propagation of waves and the vibrations induced by them in a string of a pizzicato musical instrument were previously studied [1, 2] by solving the problem with the initial conditions for the equations of transverse vibrations. The initial string shape is represented as two sides of a triangle with vertices at the bracings $x = 0$ and L, where, as a rule, $y = 0$ (rigid bracing) or, at the point $x = c$, where a performer acts on the string, $y = h$ (h corresponds to the maximum deflection of the string). It was also considered that particles in the string are initially at rest.

This formulation of the problem means that the action of the performer terminates instantaneously, which is not the case.

This problem was formulated more rigorously in [3], where the action of an exciter of vibrations (plectrum, finger nail, or finger of the performer) was considered as the interaction between a body moving with velocity $V_0(t)$ and the string during time $t = t_0$.[1] The body shape corresponds to the shape of the exciter of vibrations.

In this paper, we consider that the exciter of vibrations can move in the performer's hand according to the following laws.

(i) For a high exciter velocity and short contact time with the string (e.g., the "slap" manner), the exciter holds its orientation until the time $t = t_0$, and wave and vibration processes occur in one plane.

(ii) For a low exciter velocity and long contact time with the string, the moment $M(t)$ of the force produced by the string at the time $t = \tau_0$, when one of the transverse waves is reflected from the point $x = c$, exceeds the limiting value $M_{\lim}$, at which the exciter holds without turn, and the exciter begins to rotate. In this case, wave and vibration processes occur both for $t_0 > t \geq \tau_0$ and after the completion of the performer's action.

First, we analyze the case when the exciter of vibrations is schematically presented as an infinite thin rectangular stick acting with a constant velocity at the point $x = c$ and the stick can slip. The parameters of transverse and longitudinal waves can also be determined in the nonlinear formulation, when arising disturbances are not small. In this case, the additional spectrum of transverse–longitudinal vibrations has features including the longitudinal vibrations at the frequencies of transverse vibrations. A mathematical model of propagating transverse and longitudinal (according to [4]) waves is formulated for stick rotation, when

$$t_0 > t \geq \tau_0, \quad M(t) > M_{\lim}.$$

Possible ways of simplifying the problem are analyzed. It is reasonable to apply the method of perturbations to take into account fluctuations in the vibration process, which are associated with the plectrum shape, variation in the velocity vector at the point where the exciter of vibrations is applied, plectrum elasticity, and slackness of the bracings.

1. Let a string rigidly fixed at the points $x = 0$ and L be exposed at the point $x = c$ to the action of an infinite thin stick having the velocity components V_0 and V_τ normal and longitudinal to the stick length, respectively; i.e., V_τ is the velocity of the slip of the stick along the string.

For simplicity, we assume that $V_0 = \text{const}$ and $V_\tau = \text{const}$. The Ox and Oy axes are taken along the stick and along the velocity component V_0. In this case, the motion of the particles of the string occurs in the $z = 0$ plane and is described by the following equation of transverse vibrations:

$$\frac{\partial^2 y}{\partial t^2} = b_0^2 \frac{\partial^2 y}{\partial x^2}, \tag{1.1}$$

[1] Measuring the time of the closure of the electric circuit between the string and metallic plectrum, both under a voltage, A.V. Bryukvin and A.A. Malashin determined that t_0 was equal to 0.01–0.05 s.

Moscow State Forest University, Mytishchi, Moscow oblast, Russia
** E-mail: demyanov@mgul.ac.ru*

1028-3358/02/4711-0828$22.00

with the initial and boundary conditions

$$y(x, 0) = \frac{\partial y}{\partial x}(x, 0) = 0,$$
$$y(0, t) = y(L, t) = 0, \quad \frac{\partial y}{\partial t}(x = c, t) = V_0, \tag{1.2}$$

where b_0 is the velocity of propagation of transverse waves.

This problem can be solved by both the method of propagating waves [2] and the method of characteristics [5]. The solution is the wave process shown in Fig. 1. The initial angle α_0 of the string slope to the X axis is determined from the condition

$$\tan\alpha_0 = \bar{V}_0 \text{ or } \alpha_0 \approx \bar{V}_0, \text{ where } \bar{V}_0 = \frac{V_0}{b_0} \ll 1.$$

After the reflections of transverse waves from the bracings $x = 0$ and L, the slope angles at these points are equal to $2\alpha_0$. Once the wave reflected from the bracing arrives at the point $x = c$ and is reflected from it, the slope angles of the string at these points are equal to $3\alpha_0$, etc. Therefore, for times

$$2k\frac{c}{b_0} < t < (2k+1)\frac{c}{b_0}$$

and

$$(2k-1)\frac{c}{b_0} < t < 2k\frac{c}{b_0},$$

the slope angles of the left part of the string are $\theta_0 = 2k\alpha_0$ at the point $x = 0$ and $\theta_1 = (2k + 1)\alpha_0$ and $(2k - 1)\alpha_0$, respectively, at the point $x = c$.

According to [4], transverse displacements $U(s, t)$ of the string particles in the first approximation satisfy the equation

$$\frac{\partial^2 U}{\partial t^2} = \bar{a}_0^2\left[\frac{\partial^2 U}{\partial s^2} + \frac{1}{2(1+e_0)}\frac{\partial}{\partial s}\left(\frac{\partial y}{\partial s}\right)^2\right]. \tag{1.3}$$

Here, s is the Lagrange coordinate coinciding with the Cartesian coordinate x of the loose string, e_0 is the initial strain of the string, and $\bar{a}_0 = a_0(1 + e_0)^{-1}$, where a_0 is the velocity of transverse waves. Although longitudinal displacements are smaller than transverse displacements by an order of magnitude, their contributions to strain and dynamic stress are of the same order of magnitude as the contributions from transverse displacements. In the case under consideration, $\frac{\partial y}{\partial s}$ = const in each region shown in Fig. 1. For this region, Eq. (1.3) becomes homogeneous and, after changing to the Cartesian coordinate $x = s(1 + e_0)$, takes the following conventional form of the equation of longitudinal vibrations:

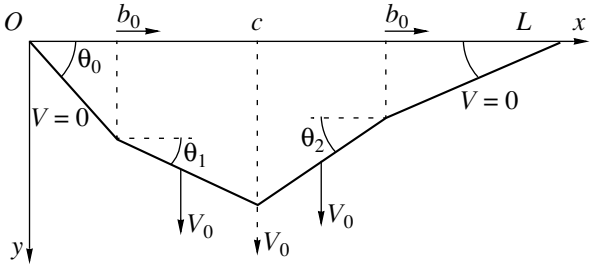

Fig. 1.

$$\frac{\partial^2 U}{\partial t^2} = a_0^2\frac{\partial^2 U}{\partial x^2}. \tag{1.4}$$

As was shown in [4], in order to formulate the problem for Eq. (1.4), it is necessary to set additional conditions at transverse waves and at the point of stick action in addition to the initial conditions $U = \frac{\partial U}{\partial t} = 0$ and boundary Cs at the points $x = 0$ and L. These additional conditions have the form

$$\left[\frac{\partial U}{\partial s} + \frac{1}{2(1+e_0)}\left(\frac{\partial y}{\partial s}\right)^2\right] = 0,$$
$$\left[\frac{\partial U}{\partial t}\right] = \frac{b_0}{2(1+e_0)}\left(\frac{\partial y}{\partial s}\right)^2, \tag{1.5}$$

where the square brackets are the discontinuity of the corresponding parameters at the right and left from transverse waves and from the point $x = c$ and present the continuity of total strain $\frac{\partial U}{\partial s} + \frac{1}{2(1+e_0)}\left(\frac{\partial y}{\partial s}\right)^2$ and the law of momentum conservation in the Ox direction, respectively.

For the problem under study, these discontinuities are independent of time. For this reason, the solutions of Eq. (1.4) consist of regions where the components of velocities $\frac{\partial U}{\partial t}$ and strains $\frac{\partial U}{\partial s}$ are constant and have discontinuities at transverse waves and at the point $x = c$ according to Eqs. (1.5). Therefore, these solutions are expanded into Fourier series involving, along with frequencies depending on $\frac{a_0}{c}$ and $\frac{a_0}{L-c}$, frequencies depending on $\frac{b_0}{c}$ and $\frac{b_0}{L-c}$, i.e., on the frequencies of transverse vibrations.

The shape of the string at $t = t_0$ differs from triangular, and its parts adjoining the point $x = c$ have transverse velocity components. Therefore, the amplitude–

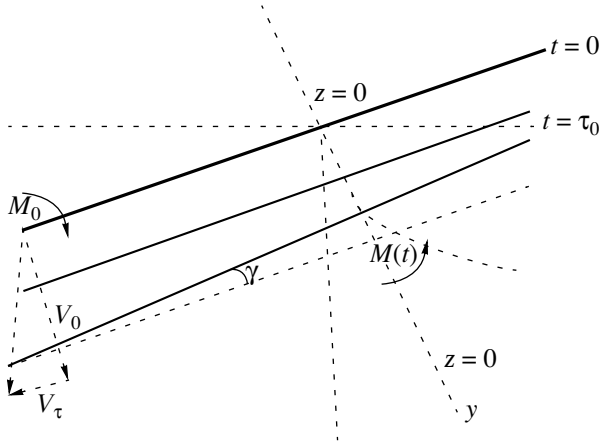

Fig. 2.

frequency spectrum of transverse vibrations for $t > t_0$ differs from that determined from the traditional formulation [1, 2] in both amplitude and phase shift, and the corresponding spectrum of transverse vibrations consists of both natural and forced vibrations (at the frequencies of transverse vibrations). The problem formulated above can also be solved in the nonlinear formulation, because the methods of dimensionalities and similarity for constant V_0 and initial parameters provide self-similar solutions in each of the arising regions bounded by the points $x = 0$, c, and L and the fronts of transverse and longitudinal waves. Moreover, in the nonlinear formulation, this problem can be solved for the action of a triangular plectrum.

Let us determine the condition under which the pattern shown in Fig. 1 remains until the time $t = t_0$.

Since tension forces in the string are directed along it and their magnitudes differ only slightly from the initial force F_0, the component F_n of these forces, which is perpendicular to the stick axis, is

$$F_n = F_0(\sin\theta_1 + \sin\theta_2) \approx F_0(\theta_1 + \theta_2) = F_0\frac{V_0}{b_0}(2k_1 + 2k_2 + 2), \quad (1.6)$$

where θ_1 and θ_2 are the deviation angles of the string at the point $x = c$ to the right and to the left of the stick and k_1 and k_2 are the number of arrivals of transverse waves from the point $x = c$ to the points $x = 0$ and L, respectively. According to this formula, F_n changes discretely. The moment of the force is $M_n = F_n(t)l(t)$, where $l(t)$ is the corresponding arm of the force. If $M_n(t_0) < M_{\lim}$, where $M_{\lim}$ is the limiting moment at which the plectrum or finger of the performer is in a constant position, the wave pattern shown in Fig. 1 and corresponding transverse vibrations hold over the entire time of the performer's action. Therefore, further propagation of waves and transverse vibrations occurs in the same plane.

2. Let us determine the time $t = \tau_0 < t_0$ at which $M(t)$ can exceed the value $M_{\lim}$. This is obviously the time at which one of the transverse waves moving from the bracings is reflected from the point $x = c$. For definiteness, we take this to be the wave moving from the point $x = 0$. For simplicity, we assume that, as this wave moves to the point $x = 0$ and the wave reflected from this point returns to the point $x = c$, no transverse wave reflected from the point $x = L$ arrives at the point $x = c$. From this time, the exciter of vibrations begins to rotate. When it is a plectrum, this rotation occurs both for the unchanged position of fingers and due to their turn together with the plectrum.

In terms of the stick slope angle $\gamma(t)$ in the ZOY plane (Fig. 2), the stick motion is described by the equation

$$J\frac{d^2\gamma}{dt^2} = M(t) - M_{\lim}, \quad (2.1)$$

where J is the moment of inertia of the stick, with the condition $\gamma = \dfrac{d\gamma}{dt} = 0$ at $t = \tau_0$.

Let $z_s(t)$ and $y_s(t)$ be the string coordinates in the stick, $y_0(t) = V_0 t$ and $z_0(t) = -l_{00} - V_\tau t$, where l_{00} is the distance from the point of contact between the string and stick to the axis of plectrum rotation at $t = \tau_0$.

In the time interval until the next arrival of the transverse wave reflected from the bracing $x = 0$ to the point $x = c$, the relation on the characteristic provides the expressions

$$\frac{\partial y}{\partial x} = \pm\frac{1}{b_0}\frac{dy_s}{dt}, \quad \frac{\partial z}{\partial x} = \pm\frac{1}{b_0}\frac{dz_s}{dt} \text{ for } x = c, \quad (2.2)$$

where signs $\pm$ correspond to the values for $x = c \pm 0$.

Since angles α and β are small, the string deviations at this point in the planes $y = 0$ and $z = 0$ are

$$\theta = \pm\frac{1}{b_0}\left(k_1 V_0 + \frac{d\bar{y}_s}{dt}\right), \quad \beta = \pm\frac{1}{b_0}\frac{dz_s}{dt}, \quad (2.3)$$

respectively, where $\bar{y}_s(t) = y_s(t) - V_0 t$. The quantities $z_s(t)$ and $y_s(t)$ are obviously related by the conditions that they are always in the stick,

$$\bar{y}_s(t) = -\tan\gamma(z_0 + l_{00} + V_\tau t), \quad (2.4)$$

and that the instantaneous velocity of the string in the stick is directed along the stick,

$$\dot{y}_0 + \tan(\gamma)\dot{z}_0 = 0. \quad (2.5)$$

Taking into account the fact that angles θ and β completely determine the direction of string tension, we find the corresponding angles and calculate the force components:

$$F_y = F_0(\theta_1 + \theta_2), \quad F_z = F_0(\beta_1 + \beta_2).$$

The string acts on the stick with the moment

$$M = F_0(\theta_1 + \theta_2)(z_s(t) - z_0(t)) + F_0(\beta_1 + \beta_2)(y_s(t) - y_0(t)). \quad (2.6)$$

3. It is reasonable to analyze these equations in terms of the dimensionless variable $\bar{t} = \frac{t}{\tau_0}$ and functions $\bar{y} = \frac{y}{V_0\tau_0}$ and $\bar{z} = \frac{z}{V_0\tau_0}$. In this case, Eq. (2.6) takes the form

$$M = F_0\frac{V_0^2\tau_0}{b_0} \times [(2n + 1 + 2\bar{y}_s + 2k)(\bar{l}_{00} + \bar{V}_\tau\bar{t} + \bar{z}_s) + 2\bar{z}_s(\bar{t} - \bar{y}_0)], \quad (3.1)$$

where $\bar{l}_{00} = \frac{l_{00}}{V_0\tau_0}$ and $\bar{V}_\tau = \frac{V_\tau}{V_0}$, and Eq. (2.1) takes the form

$$J\frac{d\gamma^2}{dt^2} = F_0\frac{V_0^2\tau_0}{b_0}[(2n + 1 + 2\bar{y}_s + 2k) \times (\bar{l}_{00} + \bar{V}_\tau\bar{t} + \bar{z}_s) + 2\bar{z}_s(\bar{t} - \bar{y}_0)] - M_{\lim}. \quad (3.2)$$

The problem is considerably simplified when the plectrum mass and, therefore, the moment of inertia are negligible. Since quantity $M(\tau_0 + 0) - M_{\lim}$ is finite at $t = \tau_0 + 0$, the angular acceleration $\frac{d^2\gamma}{dt^2}$ is infinite, and therefore the plectrum moves rapidly to the state characterized by a certain angle $\gamma = \gamma_0$ at which $M(\gamma_0) - M_{\lim} = 0$. Thus, we can consider the limiting case, where the stick instantaneously moves from the position $\gamma = 0$ to the position $\gamma = \gamma_0$. Since the components of the velocities and strains at $t = \tau_0 - 0$ are constant, this problem is self-similar and provides the wave pattern shown in Fig. 3. Using the relations [5, 6]

$$\rho_0(b_0 + u)(u - V_y) = T(1 + e_0)(1 - \cos\gamma_0),$$
$$\rho_0(b_0 + u)V_z = T(1 + e_0)\sin\gamma_0,$$

in a transverse wave moving along the string from the bend, kinematic condition $b_0\sin\gamma_0 = V\cos\theta$, relation $u = a_0(e - e_0)$ in a longitudinal wave, and the condition that the angle between the velocity of the string point and z axis is equal to γ_0, we determine all the parameters of the problem. In particular, the string moves in the stick with the velocity $V_1 = b_0\gamma_0$. Here, ρ_0 is the string density and

$$\gamma_0 = \left(\frac{\rho_0 a_0 b_0^2 - Ta_0(1 + e_0)}{\frac{3}{2}Tb_0 - \rho_0 a_0 b_0^2}\right)^{\frac{1}{2}},$$

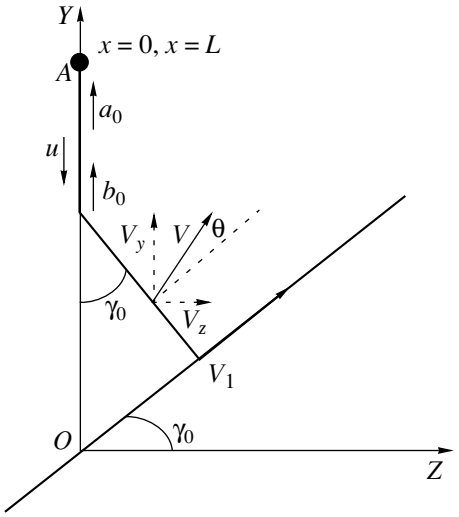

Fig. 3.

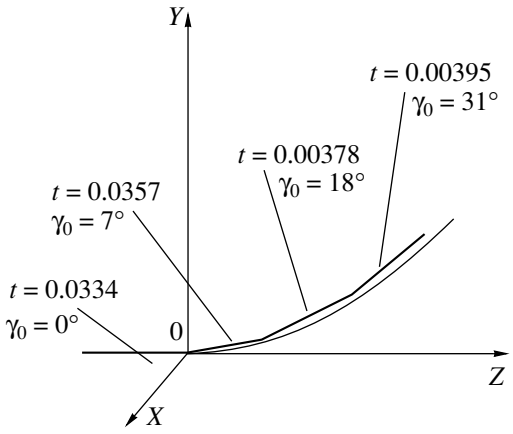

Fig. 4.

where u is the particle velocities behind the transverse wave and T is the stress.

The problem can be solved both in the linear and nonlinear formulations. When transverse waves propagating to the bracings are reflected and one of the waves arrives at the stick at time $t = \tau_0$, a case similar to the one discussed above arises. As a result, the limiting trajectory $\gamma = \gamma(t)$ is determined (Fig. 4).

4. In the framework of the linear equations of the propagation of transverse and longitudinal waves, the results can be generalized as follows.

(i) The above solutions can be corrected by the perturbation method for the actual shape of the exciter of vibrations for both $t < \tau_0$ and $\tau_0 \le t \le t_0$. In this case, $\frac{l}{L}$, where l is the characteristic width of the plectrum, is a small parameter, and corrections to the variation in the

vibration frequencies for $t < t_0$ are determined in particular.

(ii) One can take into account the fact that the velocity $V(t)$ is variable both in magnitude and direction due to rotations in the elbow, hand, and phalanxes of the finger.

(iii) The elasticity of the plectrum treated as a beam can be taken into account.

(iv) The elasticity of the bracing of the string can be taken into account, which is most simple for the case when the strain of the bracings is small, and for elastic attachment, when $\mathbf{l} = k\frac{\partial \mathbf{l}}{\partial s}$, where $\mathbf{l}$ is the displacement vector, for $s = 0$ and L. The parameter k can be considered small. In this case, the change in the vibration spectrum due to the elasticity of attachment can be determined for both $t < t_0$ and $t > t_0$.

REFERENCES

1. J. W. S. Rayleigh, *The Theory of Sound* (Macmillan, London, 1896; Gostekhteorizdat, Moscow, 1940), Vol. 1, pp. 187–257.
2. A. N. Tikhonov and A. A. Samarskiĭ, *Equations of Mathematical Physics* (Nauka, Moscow, 1977; Pergamon, Oxford, 1964).
3. Yu. A. Dem'yanov, Dokl. Akad. Nauk **372** (6), 743 (2000).
4. Yu. A. Dem'yanov, Dokl. Akad. Nauk **369** (4), 461 (1999).
5. Kh. A. Rakhmatulin and Yu. A. Dem'yanov, *Strength under Strong Short-Term Loads* (Fizmatgiz, Moscow, 1961), pp. 119–120; 129–140; 174–184.
6. Kh. A. Rakhmatulin, Prikl. Mat. Mekh. **16** (1), 23 (1952).

Translated by R. Tyapaev

Doklady Physics, Vol. 47, No. 11, 2002, pp. 833–837. Translated from Doklady Akademii Nauk, Vol. 387, No. 3, 2002, pp. 338–342.

MECHANICS

On the Stability of the Regular Precession of an Asymmetric Gyroscope

A. P. Markeev

Presented by Academician D.M. Klimov June 14, 2002

Received June 21, 2002

FORMULATION OF THE PROBLEM

We consider the motion of a rigid body with a fixed point O in a uniform gravity field. The body's weight, the distance from the center of gravity to the fixed point, and the principal moments of inertia with respect to the point O are denoted by mg, l, and A, B, and C, respectively. Let the body have no dynamical symmetry ($A > B > C$ for definiteness) and its center of gravity lie in the straight line that passes through the fixed point and is perpendicular to a circular cross section of the ellipsoid of inertia.

As was revealed by Grioli [1], under these conditions, the body can regularly precess around a nonvertical axis.

Grioli precession is the last dynamically allowed regular precession. Indeed, as was shown in [2], there are no regular precessions of a rigid body with a fixed point other than the Grioli precession and well-known Euler and Lagrange precessions of a dynamically symmetric rigid body.

In this paper, we present our results concerning the orbital stability of Grioli precession. Some aspects of the stability of Grioli precession were considered in [3–5].

MOTION OF A BODY IN THE GRIOLI CASE

We take a fixed coordinate system $OXYZ$ with the upward-directed vertical OZ axis and a coordinate system $Oxyz$ rigidly fixed to the body under study. Let the Oy axis coincide with the principal axis of inertia that corresponds to the moment of inertia B and the Oz axis pass through the center of gravity. Eulerian angles φ, θ, and ψ are used as generalized coordinates q_1, q_2, and q_3, respectively, and the corresponding momenta reduced to a dimensionless form by means of the factor $(An)^{-1}$, as generalized momenta. As an independent variable, we take the quantity $\tau = n(t + t_0)$, where t_0 is an arbitrary constant and n is determined from the relations

$$n^2 = \frac{mgl}{(A - B + C)\sqrt{b^2 + 1}}, \quad b = \frac{\sqrt{(1 - \theta_b)(\theta_b - \theta_c)}}{1 - \theta_b + \theta_c}.$$

Here, $\theta_b = \dfrac{B}{A}$ and $\theta_c = \dfrac{C}{A}$ are the dimensionless parameters of the problem. Their allowable domain on the (θ_b, θ_c) plane ($0 < \theta_c < \theta_b < 1$, $\theta_b + \theta_c > 1$) is the right triangle with vertices at the points $P_1\left(\frac{1}{2}, \frac{1}{2}\right)$, $P_2(1, 1)$, and $P_3(1, 0)$.

Grioli precession is described by the following solution of the equations of motion:

$$q_1 = f_1(\tau) = -\frac{\pi}{2} + \tau - \arctan(b\sin\tau), \qquad p_1 = g_1(\tau) = (1 - \theta_b + \theta_c)(1 - b\cos\tau); \tag{1}$$

$$q_2 = f_2(\tau) = \arccos\left(\frac{b\cos\tau}{\sqrt{b^2 + 1}}\right), \qquad p_2 = g_2(\tau) = \frac{b\sin\tau}{\sqrt{1 + b^2\sin^2\tau}}[1 + \theta_c - (1 - \theta_b + \theta_c)b\cos\tau]; \tag{2}$$

$$q_3 = f_3(\tau), \quad p_3 = \frac{\theta_c}{(1 - \theta_b + \theta_c)\sqrt{b^2 + 1}} = \text{const}. \tag{3}$$

Here,

$$f_3(\tau) = q_3(0) + (2k + 1)\frac{\pi}{2} - \arctan\left(\frac{\cot\tau}{\sqrt{b^2 + 1}}\right),$$

if

$$k\pi < \tau < (k + 1)\tau$$

and

$$f_3(k\pi) = q_3(0) + k\pi$$

Institute of Problems in Mechanics,
Russian Academy of Sciences,
pr. Vernadskogo 101, Moscow, 117526 Russia

1028-3358/02/4711-0833$22.00

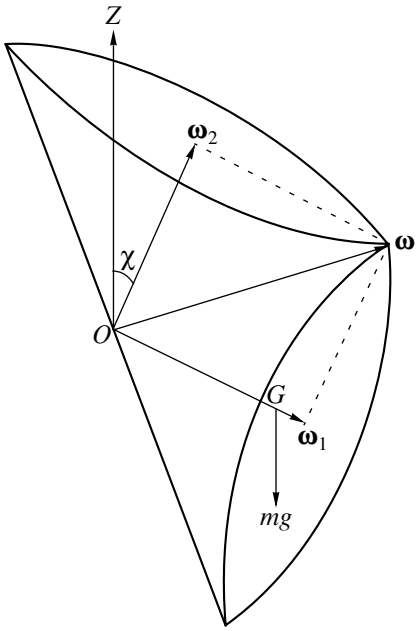

Fig. 1. Loose and fixed axoids for Grioli motion; G is the center of gravity, and $\boldsymbol{\omega}_1$ and $\boldsymbol{\omega}_2$ are the angular velocities of proper rotation and precession, respectively.

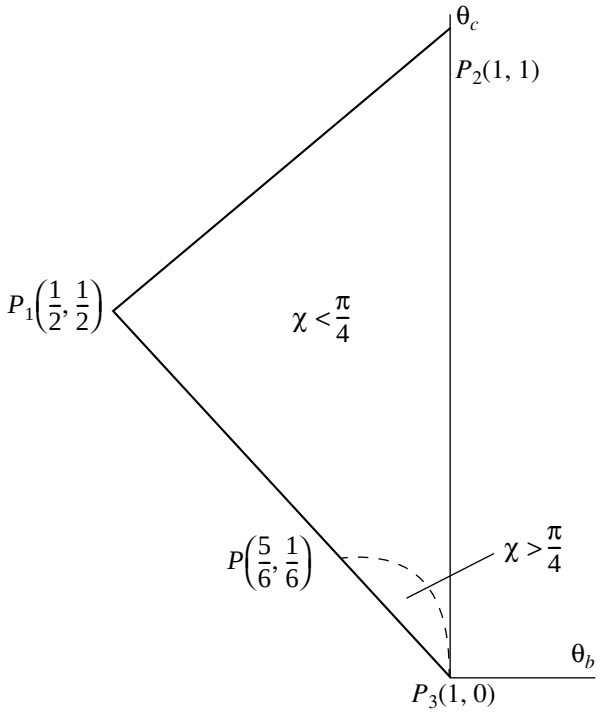

Fig. 2. Angle χ between the precession axis and vertical in various domains of the inertia parameters of a body.

for

$$k = 0, 1, \ldots .$$

For Grioli precession, the axis passing through the center of gravity of the body is the axis of its proper rotation, whereas the precession axis is inclined at the angle $\chi = \arctan b$ to the vertical (see Fig. 1). The axes of the loose and fixed axoids are perpendicular to each other. The precession velocity coincides with the angular velocity of proper rotation and is equal to n. The body's center of gravity moves around a circle on a plane perpendicular to the precession axis, where the center of the circle lies. The motion of the body is periodic: it returns to its initial orientation in absolute space with the period $\frac{2\pi}{n}$, and the angular velocity takes its initial value.

The dependence of the angle χ on the moments of inertia of the body is illustrated in Fig. 2. The dashed curve, a section of a hyperbola, corresponds to $\chi = \frac{\pi}{4}$ and intersects the boundary P_1P_3 at the point $P\left(\frac{5}{6}, \frac{1}{6}\right)$. The vertical straight line $\theta_b = 1$ is tangent to this curve at the point P_3. The angle of proper rotation φ increases monotonically in the range $\chi < \frac{\pi}{4}$ ($\dot{f}_1 > 0$). In the range $\chi > \frac{\pi}{4}$, the quantity $\dot{f}_1 > 0$ vanishes; hence, the angle φ varies nonmonotonically.

ON THE STABILITY IN A FIRST APPROXIMATION

The coordinate q_3 is cyclic. Replacing the momentum p_3 in the Hamiltonian function by its constant value given by Eq. (3), we obtain the Hamiltonian $H(q_1, q_2, p_1, p_2; \theta_b, \theta_c)$ for the reduced system with two degrees of freedom. This system admits a solution that is 2π-periodic in τ and is defined by Eqs. (1) and (2).

We set $q_i = f_i(\tau) + Q_i$ and $p_i = g_i(\tau) + P_i$, $i = 1, 2$. Let $\mathbf{Y}(\tau)$ be the matrix of fundamental solutions to the equations for perturbed motion that are linearized with respect to Q_i and P_i. We found this matrix by numerical integration [with $\mathbf{Y}(0) = \mathbf{E}$, where $\mathbf{E}$ is the 4×4 identity matrix]. The characteristic equation for the matrix $\mathbf{Y}(2\pi)$ can be written in the form

$$(\rho - 1)^2(\rho^2 - 2a\rho + 1) = 0; \quad a = \frac{1}{2}\mathrm{Sp}\,\mathbf{Y}(2\pi) - 1. \quad (4)$$

For $|a| > 1$, a parametric resonance takes place and Grioli precession is unstable by virtue of the Lyapunov theorem on the stability in a first approximation. The boundaries of the parametric-resonance domain are determined by the condition $|a| = 1$. For $|a| < 1$, the pre-

cession is orbitally stable in a first approximation. In this case, the roots of Eq. (4) are

$$\rho_1 = \exp(i2\pi\lambda), \quad \rho_2 = \exp(-i2\pi\lambda),$$

$$\text{and } \rho_3 = \rho_4 = 1,$$

where λ is a real quantity determined from the equation

$$\cos 2\pi\lambda = a. \tag{5}$$

Our analytical and numerical treatments showed that there are only two parametric-resonance domains. These domains are shaded in Fig. 3 and begin with the points $P_4\left(\frac{\sqrt{3}}{3}, \frac{\sqrt{3}}{3}\right)$ and $P_7\left(\frac{2\sqrt{5}}{5}, \frac{2\sqrt{5}}{5}\right)$ on the segment P_1P_2. We found analytical expressions for the boundaries of the parametric-resonance domains in small neighborhoods of these points (when $\theta_b = \theta_c + \varepsilon^2$).

The left and right boundaries of the domain starting from the point P_4 terminate at the points $P_5(0.74957, 0.25043)$ and $P_6(0.75652, 0.24348)$, respectively. For small ε, the curves P_4P_5 and P_4P_6 are specified by the respective equations

$$\theta_b = \frac{\sqrt{3}}{3} + \frac{1}{540}(267 - 73\sqrt{3})\varepsilon^2$$

$$+ \frac{1}{1944000}(278042\sqrt{3} - 141267)\varepsilon^4 + O(\varepsilon^6)$$

$$= 0.5773502693 + 0.2602968351\varepsilon^2$$

$$+ 0.1750596043\varepsilon^4 + O(\varepsilon^6)$$

and

$$\theta_b = \frac{\sqrt{3}}{3} + \frac{1}{540}(267 - 73\sqrt{3})\varepsilon^2$$

$$+ \frac{1}{1944000}(453542\sqrt{3} - 1147983)\varepsilon^4 + O(\varepsilon^6)$$

$$= 0.5773502693 + 0.2602968351\varepsilon^2$$

$$+ 0.9946197466\varepsilon^4 + O(\varepsilon^6).$$

When $\theta_c \longrightarrow 0$, both the boundaries of the parametric-resonance domain starting from the point P_7 tend to the corner point P_3 of the allowable domain. In the vicinity of the point P_7, the boundary curves are specified by the equations

$$\theta_b = \frac{2\sqrt{5}}{5} + \frac{1}{1000}(405 - 373\sqrt{5})\varepsilon^2$$

$$\mp \frac{1}{80}\sqrt{3050 - 1310\sqrt{5}}\varepsilon^3 + O(\varepsilon^4)$$

$$= 0.8944271912 - 0.4290533558\varepsilon^2$$

$$\mp 0.1373584209\varepsilon^3 + O(\varepsilon^4),$$

where the upper and lower signs refer to the left and right boundaries, respectively.

NONLINEAR ANALYSIS OF ORBITAL STABILITY

When the parameters θ_b and θ_c are outside the parametric-resonance domain, the first approximation is insufficient to solve the problem of the orbital stability of Grioli precession exactly. In this case, it is necessary to analyze nonlinear equations for perturbed motion.

Method of solving the problem. In order to solve the problem, we reduced the Hamiltonian of perturbed motion to the normal form and used the Arnold–Moser theorem [6] and stability conditions for a Hamiltonian system with resonance [7, 8]. The Hamiltonian was normalized by the Deprit–Hori method [7].

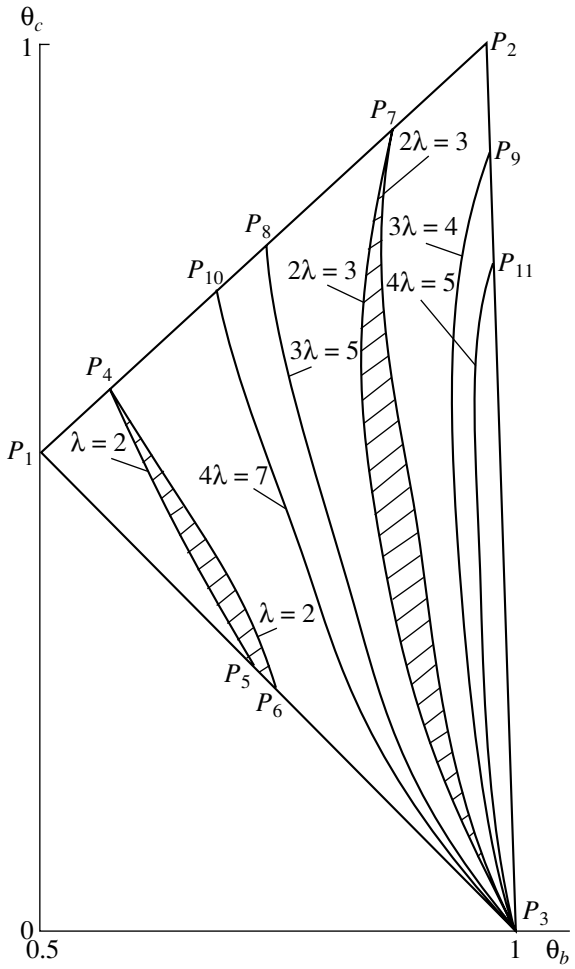

Fig. 3. Parametric-resonance domains (shaded) and resonance curves up to the fourth order. In a first approximation, Grioli precession is orbitally stable outside the shaded domains.

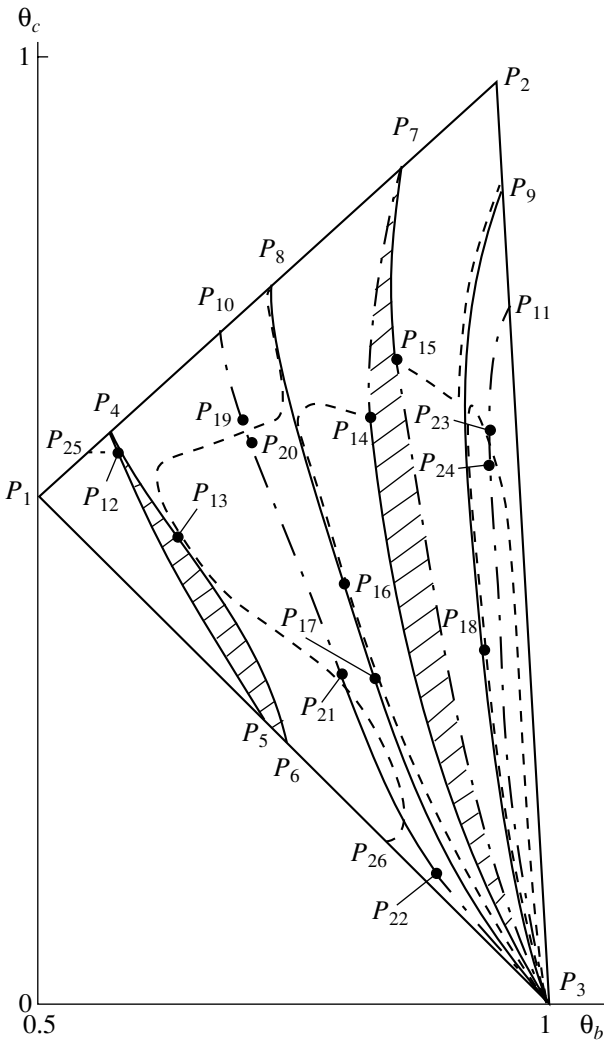

Fig. 4. Domains of orbital stability and instability.

First, we made the canonical change of variables $(q_i, p_i) \longrightarrow (\xi_i, \eta_i, i = 1, 2)$ such that the following solution in the new variables

$$\xi_1(\tau) = \tau + \xi_1(0), \quad \eta_1 = \xi_2 = \eta_2 = 0 \qquad (6)$$

corresponded to Grioli precession and the Hamiltonian function was 2π-periodic in ξ_1. The problem of the orbital stability of Grioli precession is equivalent to that of the stability of solution (6) with respect to perturbations of the quantities η_1, ξ_2, and η_2 determining the deviation of perturbed trajectories from the unperturbed trajectory.

For θ_b and θ_c belonging to the domains $\chi < \frac{\pi}{4}$ and $\chi \geq \frac{\pi}{4}$ (see Fig. 2), the variables ξ_i and η_i were introduced by the respective canonical transformations

$$q_1 = f_1(\xi_1), \quad q_2 = f_2(\xi_1) + \xi_2,$$
$$p_1 = g_1(\xi_1) + (f_1')^{-1}[g_2'\xi_2 + \eta_1 - f_2'\eta_2],$$
$$p_2 = g_2(\xi_1) + \eta_2$$

and

$$q_1 = f_1(\xi_1) - \eta_2,$$
$$q_2 = f_2(\xi_1) + (f_1' + g_2')^{-1}[f_1'\xi_2 - \eta_1 + (f_2' + g_1')\eta_2],$$
$$p_1 = g_1(\xi_1) + (f_1' + g_2')^{-1}[g_2'\xi_2 + \eta_1 - (f_2' + g_1')\eta_2],$$
$$p_2 = g_2(\xi_1) + \eta_2.$$

Here, f_i and g_i are the functions given by Eqs. (1) and (2) and the primes stand for the differentiation with respect to ξ_1.

Resonances. When solving the problem of stability, it is important to know whether the system under consideration has resonances, particularly, resonances of up to the fourth order (in these cases, the quantity $k\lambda$ is an integer for $k = 1, 2, 3, 4$).

Equation (5) ambiguously determines the quantity λ. Taking the continuity of characteristic indices into account, we removed this ambiguity by considering the limiting case $\theta_b = \theta_c$, where the coefficients of the linearized equations for perturbed motion are constants and $\lambda = \sqrt{1 + \theta_b^{-2}}$ is the frequency of small oscillations in the vicinity of the unperturbed trajectory.

In the domains $P_1P_4P_5$, $P_7P_2P_3$, and $P_4P_7P_3P_6$ in Fig. 3, $\lambda = 2 + (2\pi)^{-1}\arccos a$, $1 + (2\pi)^{-1}\arccos a$, and $2 - (2\pi)^{-1}\arccos a$, respectively.

The first-order resonance condition ($\lambda = 2$) is satisfied on the curves P_4P_5 and P_4P_6, and the second-order resonance condition ($2\lambda = 3$), on the boundaries of the parametric-resonance domain starting from the point P_7. In the first approximation, two third-order resonance curves $3\lambda = 5$ and $3\lambda = 4$ starting from the points $P_8\left(\frac{3}{4}, \frac{3}{4}\right)$ and $P_9\left(1, \frac{\sqrt{7}}{3}\right)$, respectively, as well as two fourth-order resonance curves $4\lambda = 7$ and $4\lambda = 5$ starting from the points $P_{10}\left(\frac{4\sqrt{33}}{33}, \frac{4\sqrt{33}}{33}\right)$ and $P_{11}\left(1, \frac{3}{4}\right)$, respectively, exist in the stability domains (see Fig. 3). As θ_c tends to zero, these curves tend to the point P_3.

Results. The results of the numerical and analytical investigation of the orbital stability of Grioli precession for parameters θ_b and θ_c lying outside the parametric-resonance domain are presented below (see also Fig. 4). The calculations were carried out for $\theta_c \geq 0.01$.

Grioli precession is orbitally unstable on the boundaries P_4P_5 and P_4P_6 of the parametric-resonance domain starting from the point P_4, except the point $P_{12}(0.578, 0.57175)$, at which the question of stability

remains open, and the point P_{13}(0.65635, 0.444957), at which the precession is orbitally stable.

The left and right boundaries of the parametric-resonance domain starting from the point P_7 are divided by the points P_{14}(0.853, 0.604) and P_{15}(0.87876, 0.678), respectively, into two pairs of intervals (see Fig. 4). There is orbital stability (instability) in the half-open intervals P_7P_{14} and P_3P_{15} (P_7P_{15} and P_3P_{14}). The question of stability at the points P_{14} and P_{15} remains open.

The intervals on which the Grioli precession is orbitally unstable (stable) are shown in Fig. 4 by solid (dash–dotted) lines.

There is orbital instability on the third-order resonance curves, except the three orbital-stability points P_{16}(0.809339, 0.449) and P_{17}(0.831305, 0.336) on the curve $3\lambda = 5$ and P_{18}(0.954319, 0.389) on the curve $3\lambda = 4$.

We found three instability intervals on the fourth-order resonance curves ($P_{19}P_{20}$, $P_{21}P_{22}$) $4\lambda = 7$ and ($P_{23}P_{24}$) $4\lambda = 5$. The question of stability at the boundary points P_{19}(0.7221, 0.5905), P_{20}(0.7224, 0.5895), P_{21}(0.809, 0.332), P_{22}(0.892, 0.138), P_{23}(0.97688, 0.5746), and P_{24}(0.9767, 0.5717) remains open. The precession is orbitally stable at the other points on these curves.

For parameters θ_b and θ_c lying outside the parametric-resonance domains and resonance curves considered above, Grioli precession is stable everywhere, except perhaps for the set of points at which the Arnold–Moser condition for the isoenergetic nondegeneracy of the Hamiltonian for perturbed motion is violated. This set consists of five sections shown in Fig. 4 by the dashed lines between points P_{25}(0.56776, 0.56776) and P_{12}; P_8 and P_{26}(0.83902, 0.16098); P_{14} and P_3; P_{15} and P_9; and the loop between the curve $3\lambda = 4$ and the vertical line $\theta_b = 1$.

Thus, we solved the problem of the orbital stability of Grioli precession over almost the entire allowable domain of the parameters for $\theta_c \geq 0.01$. The analysis of the stability at the remaining six points P_{k+18} ($k = 1, 2, \ldots, 6$) on the fourth-order resonance curves and at points on the isoenergetic-nondegeneracy curve must take into account terms higher than the fourth order in the expansion of the Hamiltonian for perturbed motion.

ACKNOWLEDGMENTS

This work was supported in part by the Russian Foundation for Basic Research, project no. 02-01-00831.

REFERENCES

1. G. Grioli, Ann. Mat. Pura Appl. **26** (4), 271 (1947).
2. M. P. Gulyaev, Tr. Sekt. Mat. Mekh. AN Kaz. SSR **1**, 202 (1958).
3. G. Grioli, Ann. Scuola Norm. Sup. Pisa (3) **1**, 43 (1949).
4. A. Z. Bryum, Mekh. Tverd. Tela (Kiev) **19**, 68 (1987).
5. V. N. Thai, Prikl. Mat. Mekh. **64** (5), 848 (2000).
6. V. I. Arnol'd, V. V. Kozlov, and A. I. Neishtadt, *Mathematical Aspects of Classical and Celestial Mechanics* (Editorial URSS, Moscow, 2002; Springer-Verlag, New York, 1997).
7. A. P. Markeev, *Libration Points in Celestial Mechanics and Cosmodynamics* (Nauka, Moscow, 1978).
8. A. P. Markeev, Prikl. Mat. Mekh. **64** (5), 833 (2000).

Translated by V. Chechin